

Condition Monitoring of Induction Motors in the Nuclear Power Station Environment



Prepared by:

Naasef Rylands

RYLNAA001

Department of Electrical Engineering
University of Cape Town

Prepared for:

Professor Paul Barendse

Department of Electrical Engineering
University of Cape Town

October 2018

Submitted to the Department of Electrical Engineering at the University of Cape Town in partial fulfilment of the academic requirements for a *Master of Engineering specialising in Nuclear Power*.

Key Words: Induction Motor; Condition Monitoring; Spectral Analysis; Nuclear Power

The copyright of this thesis vests in the author. No quotation from it or information derived from it is to be published without full acknowledgement of the source. The thesis is to be used for private study or non-commercial research purposes only.

Published by the University of Cape Town (UCT) in terms of the non-exclusive license granted to UCT by the author.

Declaration

- 1. I know that plagiarism is wrong. Plagiarism is to use another's work and pretend that it is one's own.**
- 2. I have used the IEEE convention for citation and referencing. Each contribution to, and quotation in, this final year project report from the work(s) of other people, has been attributed and has been cited and referenced.**
- 3. This final year project report is my own work.**
- 4. I have not allowed, and will not allow, anyone to copy my work with the intention of passing it off as their own work or part thereof**

Name: Naasef Rylands

Signature: Signed by candidate

Date: 18 October 2018

Terms of Reference

To fulfil the requirements towards the degree of Master of Engineering in Nuclear Power, students are required to write a 60 credit dissertation after completing all the necessary coursework. To this end, the author approached Professor Paul Barendse for assistance with finding a suitable research topic.

After consultation with Professor Barendse, it was agreed that the author would conduct research in the area of condition monitoring as applied to electrical machines. The brief was to use the condition monitoring test rig developed by previous students to conduct research into acceptable methods of detecting incipient faults in induction machines, with a view of applying these methods in a Nuclear Power Station environment.

It was agreed that existing techniques will be validated for both grid connected as well as inverter-fed induction machines. Additionally, specific faults should be investigated to ascertain if fault detection could be improved. Finally, the feasibility of applying the researched techniques to a nuclear power station environment should be investigated.

Acknowledgements

I would like to acknowledge and thank Professor Barendse for his guidance and patience in this endeavour, without which I would have struggled.

To Mr. Chris Wozniak, thank you for your assistance in the lab and with the test rig. To the lab assistants, Riyaad and Masi, thank you for your assistance with changing motors and alignment.

To my family, thank you for your patience during this endeavour.

And to the Lord belongs all thanks.

Abstract

The induction motor is a highly utilised electrical machine in industry, with the nuclear industry being no exception. A typical nuclear power station usually contains more than 1000 motors, where they are used in safety and non-safety applications. The efficient and fault-free operation of this machine is critical to the safe and economical operation of any plant, including nuclear power stations.

A comprehensive literature review was conducted that covered the functioning of the induction machine, its common faults and methods of detecting these faults. The Condition Based Maintenance framework was introduced in which condition monitoring of induction machines is an essential component. The main condition monitoring methods were explained with the main focus being on Motor Current Signature Analysis (MCSA) and the various methods associated with it. Three analysis methods were selected for further study, namely, Current Signature Analysis, Instantaneous Power Signature Analysis (IPSA) and Motor Square Current Signature Analysis (MSCSA). Essentially, the methodology used in this dissertation was to study the three common motor faults (bearings, stator and rotor cage) in isolation and compare the results to that of the healthy motor of the same type. The test loads as well as fault severity were varied where possible to investigate its effect on the fault detection scheme. The data was processed using an FFT based algorithm programmed in MATLAB.

The results of the study of the three spectral analysis techniques showed that no single technique is able to detect motor faults under all tested circumstances. The MCSA technique proved the most capable of the three techniques as it was able to detect faults under most conditions, but generally suffered poor results in inverter driven motor applications. The IPSA and MSCSA techniques performed selectively when compared to MCSA and were relatively successful when detecting the mechanical faults. The fact that the former techniques produce results at unique points in the spectrum would suggest that they are more suitable for verifying results. As part of a comprehensive condition monitoring scheme, as required by a large population of the motors on a nuclear power station, the three techniques presented in this study could readily be incorporated into the Condition Based Maintenance framework where the strengths of each could be exploited.

Table of Contents

Terms of Reference	3
Acknowledgements	4
Abstract	5
Table of Contents	6
List of Figures	11
List of Tables	14
1 Introduction	19
1.1 Background to the study	19
1.2 Problem Statement	19
1.3 Research Questions	20
1.4 Objectives of this study	21
1.5 Scope and Limitations	21
1.6 Plan of development	21
2 Literature Review	23
2.1 Introduction	23
2.2 Induction Machines	23
2.2.1 Constructional Features	23
2.2.2 Principle of operation	24
2.2.3 Performance characteristics	25
2.2.4 Methods of control	26
2.3 Induction Motor Faults	28
2.3.1 Bearing Faults	29
2.3.2 Stator Faults	30
2.3.3 Rotor faults	32
2.3.4 Eccentricity related faults	33
2.4 Maintenance in the Nuclear Power Station Environment	34
2.4.1 Background	34
2.4.2 Approach to Maintenance	34
2.4.3 Condition Based Maintenance of Induction Motors	36
2.5 Induction Motor Condition Monitoring Methods	37
2.5.1 Vibration Monitoring	37
2.5.2 Temperature Measurements	38

2.5.3	Axial Flux Related Methods.....	39
2.5.4	Acoustic Methods.....	40
2.5.5	Motor Current Signature Analysis.....	41
2.6	Concluding Remarks.....	46
3	Theory Development – Fault Signatures and Signal Processing Techniques	47
3.1	Introduction.....	47
3.2	Analysis Techniques.....	47
3.2.1	Motor Current Signature Analysis.....	47
3.2.2	Instantaneous Power Signature Analysis	47
3.2.3	Motor Square Current Signature Analysis	48
3.3	Fault signatures.....	48
3.3.1	Stator faults	49
3.3.2	Broken Rotor Bar Faults.....	51
3.3.3	Bearing faults.....	52
3.4	Signal Processing Techniques.....	56
3.4.1	The Fourier Transform and FFT algorithm	56
3.4.2	Windowing and Zero Padding	57
3.5	Concluding Remarks.....	58
4	Experimental Setup and Testing Methodology	59
4.1	Introduction.....	59
4.2	The Induction Motor Test Rig.....	59
4.2.1	Instrumentation and Data Acquisition	61
4.2.2	Data Processing	62
4.2.3	Test Motors	63
4.2.4	Motor Supplies and Loads	65
4.3	Experimental Methodology	66
4.3.1	Baseline Conditions.....	66
4.3.2	Experimental Procedure	67
4.4	Concluding Remarks.....	68
5	Results and Discussion.....	69
5.1	Introduction.....	69
5.2	Stator fault tests using Motor Current Signature Analysis	69
5.2.1	MCSA: Inter-turn fault – 4 shorted turns.....	69
5.2.2	MCSA: Inter-turn fault with load variation – 4 shorted turns	72

5.2.3	MCSA: Reduction in fault severity – 2 shorted turns	74
5.2.4	MCSA: Inter-turn fault with load variation – 2 shorted turns	75
5.2.5	MCSA: Inverter connected motor with inter-turn fault	76
5.3	Stator fault detection using Motor Square Current Signature Analysis	77
5.3.1	MSCSA: Inter-turn fault – 4 shorted turns.....	77
5.3.2	MSCSA: Inter-turn fault with load variation – 4 shorted turns.....	78
5.3.3	MSCSA: Reduction in fault severity – 2 shorted turns.....	79
5.3.4	MSCSA - Inverter connected motor with inter-turn fault	80
5.4	Stator fault detection using Instantaneous Power Signature Analysis.....	81
5.4.1	IPSA: Inter-turn fault – 4 shorted turns	81
5.4.2	IPSA: Reduction in fault severity – 2 shorted turns	82
5.4.3	IPSA: Inverter connected motor with inter-turn fault.....	83
5.4.4	Summary of stator inter-turn fault detection	83
5.5	Broken Rotor Bar Fault Detection using Motor Current Signature Analysis	85
5.5.1	MCSA: Broken Rotor Bars at 100% load.....	85
5.5.2	MCSA: Broken rotor bar fault with load variation	86
5.5.3	MCSA - Inverter driven motor with broken rotor bars.....	88
5.6	Broken Rotor Bar Fault Detection using Instantaneous Power Signature Analysis.....	89
5.6.1	IPSA: Broken Rotor Bars at 100% load	89
5.6.2	IPSA: Broken rotor bar fault with load variation	90
5.6.3	IPSA - Inverter driven motor with broken rotor bars	92
5.7	Broken Rotor Bar Fault Detection using Motor Square Current Signature Analysis ...	94
5.7.1	MSCSA: Grid connected broken rotor bar motor.....	94
5.7.2	MSCSA - Inverter driven motor with broken rotor bars.....	96
5.7.3	Similarities between IPSA and MSCSA.....	97
5.8	The Effect of Reduced Voltage on Broken Rotor Bar Fault Detection.....	99
5.8.1	Motor at no-load with 10% supply voltage reduction	99
5.8.2	Motor at no-load with 20% supply voltage reduction	102
5.8.3	Concluding remarks.....	102
5.9	Bearing Fault Detection using Motor Current Signature Analysis	103
5.9.1	MCSA: Bearing outer race fault.....	103
5.9.2	MCSA: Bearing inner race fault.....	105
5.9.3	Effects of the inverter on bearing fault detection using MCSA.....	107
5.10	Bearing Fault Detection using Instantaneous Power Signature Analysis	108

5.10.1	IPSA: Bearing outer race fault.....	108
5.10.2	IPSA: Bearing inner race fault.....	110
5.10.3	Effects of the inverter on bearing fault detection using IPSA.....	112
5.11	Bearing Fault Detection using Motor Square Current Signature Analysis.....	113
5.11.1	MSCSA: Bearing outer race fault.....	113
5.11.2	MSCSA: Bearing inner race fault.....	114
5.11.3	Effects of the inverter on bearing fault detection using MSCSA.....	115
5.11.4	Bearing Fault Detection Summary.....	116
5.12	Summary of Results.....	117
6	Conclusions and Recommendations.....	118
6.1	Conclusions.....	118
6.2	Recommendation.....	120
7	List of References.....	121
8	Appendices.....	130
	Hardware.....	130
	<i>Inverter Drive Parameters</i>	130
	<i>Servo Drive Parameters</i>	130
	<i>Control Panel Schematics</i>	131
	Software.....	133
	LabView Block Diagram.....	133
	<i>MATLAB Code</i>	133
	Appendix B - Results.....	138
	MCSA: Inter-turn fault – 4 shorted turns.....	138
	MCSA: Inverter connected motor with inter-turn fault (4 turns).....	138
	MCSA: Inverter connected motor with inter-turn fault (2 turns).....	139
	IPSA: Inter-turn fault – 4 shorted turns.....	139
	IPSA: Inter-turn fault – 2 shorted turns.....	141
	IPSA: Inter-turn fault – 4 shorted turns (inverter).....	142
	IPSA: Inter-turn fault – 2 shorted turns (inverter).....	143
	MSCSA: Inter-turn fault – 4 shorted turns.....	144
	MSCSA: Inter-turn fault – 2 shorted turns.....	145
	MSCSA: Inter-turn fault – 4 shorted turns (inverter).....	147
	MSCSA: Inter-turn fault – 2 shorted turns (inverter).....	148
	MCSA: Broken Rotor Bar Fault, Grid supplied.....	149

MCSA: Broken Rotor Bar Fault, Inverter supplied	150
IPSA: Broken Rotor Bar Fault, Grid supplied.....	151
IPSA: Broken Rotor Bar Fault, Inverter supplied.....	153
MSCSA: Broken Rotor Bar Fault, Grid supplied	154
MSCSA: Broken Rotor Bar Fault, Inverter supplied	156
MSCSA: The Effect of Field Weakening on Broken Rotor Bar Fault Detection	158
MCSA: Bearing faults.....	159
Appendix C – Derivations	161
9 EBE Faculty: Assessment of Ethics in Research Projects.....	163

List of Figures

Figure 2-1: Overview of an induction motor with cut-away showing the motor internals. [4]	24
Figure 2-2: Torque versus Speed characteristic for an induction machine at various supply voltages [9].	26
Figure 2-3: Graph of Torque versus Speed demonstrating the effect of changing rotor resistance [9].	26
Figure 2-4: Basic concept of supplying variable frequency to an induction motor using power electronics [13].	27
Figure 2-5: Torque versus speed graph showing constant volts per hertz control scheme [13].	28
Figure 2-6: Dissection of a typical ball bearing showing its major parts [6].	29
Figure 2-7: Three phase AC motor winding showing different types of stator faults [12].	31
Figure 2-8: Cast rotor showing broken rotor bars [18].	32
Figure 2-9: Maintenance strategy of a nuclear power station as per IAEA guidelines [5].	35
Figure 3-1: Frequency spectrum of stator current showing inter-turn fault components [18]	49
Figure 3-2: Typical frequency spectrum of a broken rotor bar fault in an induction motor [71].	51
Figure 3-3: Bearing dimensions used for characteristic frequency calculations [77].	54
Figure 3-4: Typical outer race bearing defect frequency and its translation into the current spectrum [77].	54
Figure 4-1: The SpectraQuest Machine Fault Simulator used for testing [94].	59
Figure 4-2: Drive Control and Fault Simulation interface panel.	60
Figure 4-3: A conceptual overview of the test rig used for testing [94].	60
Figure 4-4: NI9215 Analog input module concept [95].	61
Figure 4-5: Diagram depicting terminal arrangement for simulating a stator fault [94].	64
Figure 5-1: PSD of the motor current at full load for selected n and k values (a) n=1, k=1; (b) n=1, k=3; (c) n=1, k=5;	70
Figure 5-2: Current Spectra of a motor with 4 shorted turns at (a) 0% and (b) 50% load showing fault components.	72
Figure 5-3: Current spectrum of motor with an inter-turn fault at various loads.	73
Figure 5-4: Current spectrum of motor with 2 shorted turn at 100% load.	74
Figure 5-5: Current spectrum of faulty motor with 2 shorted turns at various loads.	75

Figure 5-6: Current spectrum of an inverter driven motor with 4 shorted turns versus a healthy motor at full load.....	76
Figure 5-7: Spectrum of the squared current for the first fault component at full load.....	78
Figure 5-8: Spectrum of the squared current for the second fault component at full load.....	80
Figure 5-9: Comparison of instantaneous power and squared current spectra showing fault component <i>fst2</i> at full load.....	82
Figure 5-10: PSD of motor current showing broken rotor bar upper and lower sideband components.....	85
Figure 5-11: Current spectrum of motor with broken rotor bars at various loads.....	87
Figure 5-12: Current spectrum of inverter driven motor with broken rotor bars at no-load..	88
Figure 5-13: PSD's of motor instantaneous power showing broken rotor bar components (a) <i>fbr1</i> and (b) <i>fbr2</i>	89
Figure 5-14: Instantaneous power spectrum of motor with broken rotor bars at various loads showing <i>fbr1</i> frequencies.....	91
Figure 5-15: Instantaneous power spectrum of motor with broken rotor bars at various loads showing <i>fbr2</i> upper and lower sideband frequencies.....	92
Figure 5-16: Instantaneous power spectrum of inverter driven motor with broken rotor bars at no-load showing <i>fbr1</i> frequencies for $k = 1$ and 2	93
Figure 5-17: Instantaneous power spectrum of inverter driven motor with broken rotor bars at no-load showing <i>fbr2</i> upper and lower sideband frequencies for $k = 1$	93
Figure 5-18: PSD's of motor squared current showing broken rotor bar components (a) <i>fbr1</i> and (b) <i>fbr2</i> for $k = 1, 2, 3$	95
Figure 5-19: Squared Current spectrum of the inverter driven motor with broken rotor bars at no-load showing <i>fbr2</i> upper and lower sideband frequencies for $k = 1, 2, 3$	96
Figure 5-20: Comparative spectrum of the squared current and instantaneous power for $k = 1, 2, 3$	97
Figure 5-21: PSD of motor current for a 10% voltage reduction compared to a broken rotor bar fault at rated voltage.....	100
Figure 5-22: PSD of motor instantaneous power showing a shift in frequency between fault components <i>fbr1</i> due to field weakening.....	101
Figure 5-23: PSD of motor current showing bearing outer race fault components at 0%, 50% and 100% load respectively.....	104
Figure 5-24: PSD's of motor current showing bearing inner race fault components at 0%, 50% and 100% load respectively.....	106

Figure 5-25: Current spectra of inverter driven motor showing (a) outer race and (b) inner race fault components..... 107

Figure 5-26: Instantaneous power spectra of motor with bearing outer race fault operating at various loads..... 109

Figure 5-27: PSD of motor instantaneous power showing bearing inner race fault components at 0%, 50% and 100% load respectively..... 111

Figure 5-28: PSD of motor instantaneous power showing expected location of the outer race fault for the inverter driven motor at full load..... 112

Figure 5-29: PSD of the square of the motor current highlighting the anticipated position of the outer race fault component..... 114

Figure 5-30: PSD of the motor current squared showing the anticipated position of the inner race fault component..... 115

Figure 5-31: PSD of motor square current showing expected location of the outer race fault for the inverter driven motor at full load..... 115

List of Tables

Table 2-1: Failure statistics of motors by major component according to EPRI [15].	28
Table 4-1: Specifications of the Induction motor used for testing [96].	63
Table 4-2: Table of fault voltage and current versus fault severity.	64
Table 4-3: Percentage loading and the corresponding shaft torque versus current dissipated.	65
Table 5-1: Table of results for the motor at full load with 4 shorted turns using MCSA.	71
Table 5-2: Table of fault components (n=1; k=3) and amplitudes for a motor with 4 shorted turns at various load levels using MCSA.	72
Table 5-3: Table of fault components (n=1; k=3) and amplitudes for motor with 2 shorted turns at various loads.	75
Table 5-4: Squared Current PSD results for motor with 4 shorted turns at full load.	77
Table 5-5: Table of fault component frequencies (n=1; k=5) and amplitudes from the squared current spectra for a motor with 4 shorted turns at various loads.	78
Table 5-6: Table of fault component frequencies (n=1; k=5) and amplitudes from the squared current spectra for a motor with 2 shorted turns at various loads.	79
Table 5-7: Table of fault component frequencies (n=1; k=5) and amplitudes from the instantaneous power PSD's for a motor with 4 shorted turns at various loads.	81
Table 5-8: Table of fault components frequencies (n=1; k=5) and amplitudes from the instantaneous power PSD's for a motor with 2 shorted turns at various loads.	83
Table 5-9: Fault component frequencies and amplitudes associated with broken rotor bars with motor at full load.	86
Table 5-10: Fault component frequencies and amplitudes associated with the broken rotor bar motor at various loads.	86
Table 5-11: Fault component frequencies and amplitudes associated with the inverter driven, broken rotor bar motor at no-load and full load.	88
Table 5-12: Fault component frequencies and amplitudes associated with broken rotor bars with motor at full load using IPSA.	90
Table 5-13: Fault component frequencies and amplitudes associated with the broken rotor bar motor at various loads using IPSA.	91
Table 5-14: Fault component frequencies and amplitudes associated with the inverter driven, broken rotor bar motor at no-load and full load processed using IPSA.	92

Table 5-15: Fault component frequencies and amplitudes associated with the broken rotor bar motor at various loads using MSCSA.....	94
Table 5-16: Fault component frequencies and amplitudes associated with the inverter driven broken rotor bar motor at various loads using MSCSA.....	96
Table 5-17: Results comparison between IPSA and MSCSA for broken rotor bar case.....	98
Table 5-18: Results comparison between IPSA and MSCSA for broken rotor bar case using the inverter drive.....	98
Table 5-19: Summary of sideband distance from the fundamental frequency using MCSA....	100
Table 5-20: Summary of sideband distance from the fundamental frequency using IPSA.....	101
Table 5-21: Summary of sideband distance from the fundamental frequency using MCSA at 80% rated voltage.....	102
Table 5-22: Summary of sideband distance from the fundamental frequency using IPSA at 80% rated voltage.....	102
Table 5-23: Calculated frequencies of outer raceway fault components for healthy and faulty motors at various loads.	103
Table 5-24: Actual outer race fault frequencies and amplitudes at various motor loads.....	103
Table 5-25: Calculated frequencies of inner raceway fault components for healthy and faulty motors at various loads.	105
Table 5-26: Actual inner race fault frequencies and amplitudes at various motor loads.....	105
Table 5-27: Results for inverter driven motor with bearing fault at full load.....	107
Table 5-28: Calculated mechanical frequencies of outer raceway fault components for healthy and faulty motors at various loads.....	108
Table 5-29: Actual outer race fault frequencies and amplitudes at various motor loads.....	108
Table 5-30: Calculated mechanical frequencies of inner raceway fault components for healthy and faulty motors at various loads for use with the instantaneous power spectrum.....	110
Table 5-31: Actual inner race fault frequencies and amplitudes at various motor loads obtained from the instantaneous power spectrum.	110
Table 5-32: Results of outer race fault component frequencies and amplitudes at various motor loads based on the squared current spectrum.....	113
Table 5-33: Results of inner race fault component frequencies and amplitudes at various motor loads based on the square current spectrum.	114
Table 5-34: Summary of results for the three fault detection techniques as applied to stator, rotor bar and bearing faults.....	117
Table 8-1: Critical Parameters for the Lenze SMVector Inverter Drive [94].	130

Table 8-2: Critical parameters configured for the Delta ASDA-A2 Servo drive [94].	130
Table 8-3: Inter-turn fault components for various combinations of n and k.	138
Table 8-4: Inter-turn fault components for combinations of n and k for the inverter driven case.	138
Table 8-5: Inter-turn fault components for combinations of n and k for the inverter driven case at reduced fault severity and full load.	139
Table 8-6: Inter-turn fault components for combinations of n and k at no-load using IPSA.	139
Table 8-7: Inter-turn fault components for combinations of n and k at 50% load using IPSA.	140
Table 8-8: Inter-turn fault components for combinations of n and k at 100% load using IPSA.	140
Table 8-9: Inter-turn fault components for combinations of n and k at no-load and reduced fault severity using IPSA.	141
Table 8-10: Inter-turn fault components for combinations of n and k at 50% load and reduced fault severity using IPSA.	141
Table 8-11: Inter-turn fault components for combinations of n and k at 100% load and reduced fault severity using IPSA.	142
Table 8-12: Inter-turn fault components for combinations of n and k for the inverter driven motor at no-load using IPSA.	142
Table 8-13: Inter-turn fault components for combinations of n and k for the inverter driven motor at full load using IPSA.	143
Table 8-14: Inter-turn fault components for combinations of n and k for the inverter driven motor at full load and reduced severity using IPSA.	143
Table 8-15: Inter-turn fault components for combinations of n and k at no-load using MSCSA.	144
Table 8-16: Inter-turn fault components for combinations of n and k at 50% load using MSCSA.	144
Table 8-17: Inter-turn fault components for combinations of n and k at 100% load using MSCSA.	145
Table 8-18: Inter-turn fault components for combinations of n and k at no-load and reduced severity using MSCSA.	145
Table 8-19: Inter-turn fault components for combinations of n and k at 50% load and reduced severity using MSCSA.	146

Table 8-20: Inter-turn fault components for combinations of n and k at 100% load and reduced severity using MSCSA.....	146
Table 8-21: Inter-turn fault components for combinations of n and k at 0% load for an inverter driven motor using MSCSA.....	147
Table 8-22: Inter-turn fault components for combinations of n and k at 100% load for an inverter driven motor using MSCSA.....	147
Table 8-23: Inter-turn fault components for combinations of n and k at 100% load and reduced severity for an inverter driven motor using MSCSA.....	148
Table 8-24: Broken rotor bar fault components and its multiples for a motor at no-load.	149
Table 8-25: Broken rotor bar fault components and its multiples for a motor at 50% load..	149
Table 8-26: Broken rotor bar fault components and its multiples for a motor at 100% load.	150
Table 8-27: Broken rotor bar fault components and its multiples for an inverter driven motor at no-load.....	150
Table 8-28: Broken rotor bar fault components and its multiples for an inverter driven motor at full load.....	151
Table 8-29: Broken rotor bar fault components and its multiples for a motor at 0% load using IPSA.	151
Table 8-30: Broken rotor bar fault components and its multiples for a motor at 50% load using IPSA.	152
Table 8-31: Broken rotor bar fault components and its multiples for a motor at 100% load using IPSA.	152
Table 8-32: Broken rotor bar fault components and its multiples for an inverter driven motor at 0% load using IPSA.....	153
Table 8-33: Broken rotor bar fault components and its multiples for an inverter driven motor at 0% load using IPSA.....	154
Table 8-34: Broken rotor bar fault components and its multiples for a motor at 0% load using MSCSA.....	154
Table 8-35: Broken rotor bar fault components and its multiples for a motor at 50% load using MSCSA.....	155
Table 8-36: Broken rotor bar fault components and its multiples for a motor at 100% load using MSCSA.....	156
Table 8-37: Broken rotor bar fault components and its multiples for an inverter driven motor at 0% load using MSCSA.....	156

Table 8-38: Broken rotor bar fault components and its multiples for an inverter driven motor at 100% load using MSCSA.....	157
Table 8-39: Summary of sideband distance from the fundamental frequency at 90% rated voltage using MSCSA.....	158
Table 8-40: Summary of sideband distance from the fundamental frequency at 80% rated voltage using MSCSA.....	158
Table 8-41: Bearing fault components for inner and outer race faults at various motor loads.	159
Table 8-42: Bearing fault components for inner and outer race faults at various motor loads (inverter driven).	160

1 Introduction

1.1 Background to the study

The induction machine is the most commonly utilised electrical machine in industry and is often referred to as the workhorse of industry. Many processes in the industrial environment depend on the efficient and reliable operation of this machine. Failure during operation usually results in production stoppages with its obvious impact on revenue [1].

Various methods have been employed in industry to mitigate against this risk to production, from implementing periodic maintenance regimes to designing systems with redundancy. Both the aforementioned methods lead to a significant increase in cost, both operational and capital. Hence most large industrial installations including nuclear power stations are moving towards a Predictive Maintenance focus [2]. Under this maintenance regime the condition of the induction machines are monitored during operation, so that this type of uncontrolled scenario is prevented.

In the context of a nuclear power station, this scenario is even more critical, an example being the reactor coolant pump, which is typically driven by a large induction motor and flywheel [3]. This large motor coupled to a pump removes the heat produced by the nuclear fission process and failure of the motor could lead to reactor core damage. Several other safety as well as secondary systems utilise induction machines as part of the power generation process [4]. It is with this in mind that this study will be conducted in the field of condition monitoring of induction machines.

1.2 Problem Statement

Predictive maintenance has many benefits but usually requires special techniques to ascertain the condition of plant equipment. In the field of induction machine condition monitoring there are several techniques that can be utilised to gain insight into the state of health of the machine, namely, Temperature Monitoring, Motor Current Signature Analysis (MCSA), Vibration Monitoring, Acoustic Emission Levels and Axial Flux Monitoring [1]. Vibration Monitoring techniques are the most widely used in the industrial and nuclear environments [4].

Vibration monitoring requires access to the equipment to be monitored. In the context of a Nuclear Power Station, accessibility is highly dependent on the radiological zone the equipment falls into [4]. As such, there is a great need for condition monitoring techniques that can be implemented remotely from the equipment in question. A typical example would be access to a safety critical motor inside the containment area while the nuclear reactor is in operation. This would require that the reactor be operated at reduced output at the very least to avoid radiation overdosing of maintenance personnel. This also has a natural impact on revenue and employee dose levels and limits.

There is thus a need to develop and apply robust techniques to remotely monitor the condition of induction machines in the nuclear environment, where vibration monitoring typically dominates. To this end Motor Current Signature Analysis can be used to achieve this objective, since motor currents can typically be accessed in safe radiological zones [5], [6].

1.3 Research Questions

The advantages of vibration monitoring for the detection of incipient faults in induction machines is well documented in the subject literature, as well as its comparison to Motor Current Signature Analysis [7], [8]. With a view of the operational environment of a nuclear power station, and the need to reduce the radiation dose of workers, the following research questions will be addressed:

1. Is the technique of Motor Current Signature Analysis (MCSA) able to remotely detect the most common faults or incipient faults that occur in induction motors in a nuclear environment?
2. Is the technique robust enough to detect the presence of faults in grid connected and inverter driven induction motors?
3. Does the technique prove reliable with load variation and reduced fault severity?
4. Are there other related techniques that can be applied to the collected data that can verify or enhance the results of the Current Analysis method?
5. What are the merits of these techniques in comparison to one another?
6. Can a combined fault detection scheme be recommended for a particular fault type?

1.4 Objectives of this study

Through investigating the aforementioned questions, this study aims to provide a comprehensive recommendation as to the performance of MCSA in detecting common faults in induction machines, and to recommend additional post processing techniques that mitigate the shortcomings of the MCSA technique so as to make it more reliable in a nuclear environment. Increased use of Current Analysis in the nuclear environment could potentially make a positive contribution towards dose reduction in workers.

1.5 Scope and Limitations

The study presented in this dissertation deals with the squirrel cage induction machine in motor mode only. The study focuses on three of the more common faults in these machines, namely, bearing faults, winding faults and broken rotor bar faults. The motors were grid connected and inverter-fed for the various tests and connected to resistive or servo motor loads depending on the test requirements. The quality of the laboratory supply was checked for balance and total harmonic distortion and was deemed acceptable. To achieve the objectives of the study, current, voltage, shaft speed and torque were the primary measurands.

1.6 Plan of development

Henceforth, the thesis is presented as follows:

Chapter 2 provides a comprehensive literature review of the induction machine, its typical faults and the need for condition monitoring. It then proceeds into reviewing the condition monitoring techniques as they apply to induction motors.

Chapter 3 presents the theory for understanding and applying spectral analysis, which is the preferred signal processing tool utilised in the most common condition monitoring techniques. It then proceeds to describe the theory associated with the Motor Current Signature Analysis and the spectral signatures associated with the different motor faults. Additional post-processing techniques such as Instantaneous Power Signature Analysis and Motor Square Current Signature Analysis are then presented.

Chapter 4 presents an overview of the experimental setup and testing methodology used for data collection and analysis.

Chapter 5 provides a detailed account of the results obtained from the experimentation.

Chapter 6 summarizes the findings from the results in chapter 5 and provides conclusive insight into outcomes of the experimentation and research questions. Recommendations for the application of the results will be provided, together with suggested avenues to be investigated for future research in the area.

2 Literature Review

2.1 Introduction

The induction motor is the most commonly used electrical machine in industry, largely due to its simple design and robust construction that effectively results in a highly reliable and efficient piece of equipment [6], [9].

2.2 Induction Machines

2.2.1 Constructional Features

The induction machine can essentially be viewed as a transformer with moving parts separated by an airgap that effectively converts electrical energy to mechanical energy. This similarity is evident in the equivalent circuits of the two devices. With this in mind, the primary circuit or stator typically consists of a three phase winding embedded in a laminated sheet steel core and mounted in a solid frame. The windings which can be single or double layered are distributed across the core per phase in a full or short pitched configuration [9], [10].

The rotor of the induction machine is normally of two types, namely, Wound Rotor or Squirrel Cage type. The Squirrel Cage design is the most common in industry, including Nuclear Power Stations [6]. The Wound Rotor design is effectively a three phase winding similar to the stator, with lead ends brought out onto slip rings via carbon brushes for the purposes of controlling the motor torque via an external resistance [9]. The Squirrel Cage rotor design consists of die-cast aluminium bars shorted by end-rings housed in a laminated steel core. The parallel bars typically run at an angle relative to the end-rings to reduce magnetic hum and the tendency of the rotor to lock up [11].

A fan is typically mounted on the non-drive end of the motor to provide forced cooling of the stator and rotor. The rotor is mounted on bearings housed in the end flanges [12]. Smaller motors with lower horsepower up to 200hp typically use ball bearings and/or roller bearings on the non-drive and drive ends respectively. Motors above 200hp are more likely to use ring lubricated sleeve bearings or oil lubricated bearings. This simple, rugged design results in a reliable and economical motor with respect to maintenance costs [6].

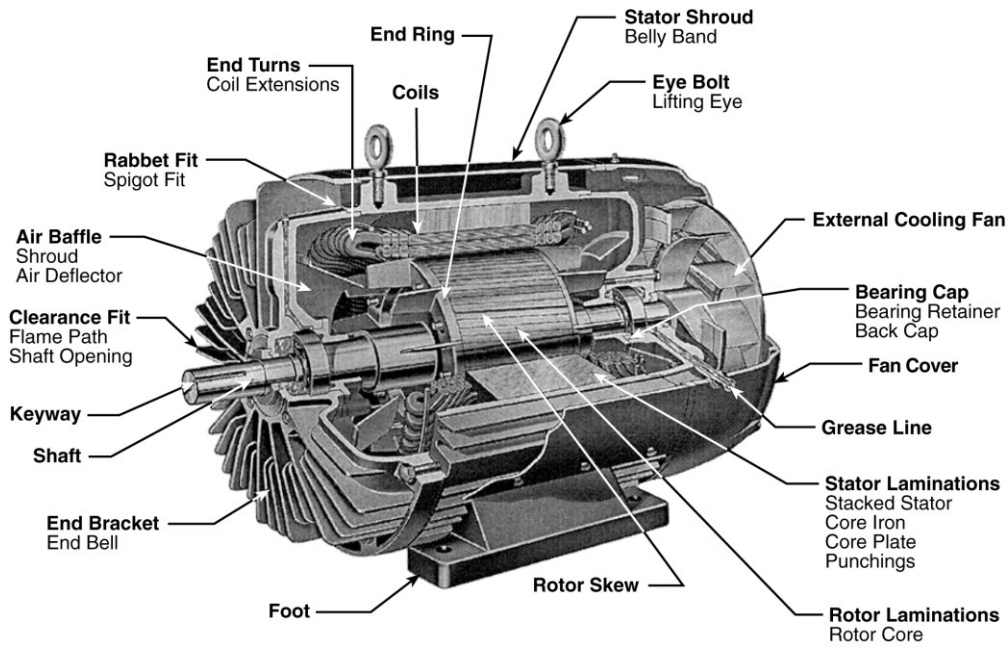


Figure 2-1: Overview of an induction motor with cut-away showing the motor internals. [4]

2.2.2 Principle of operation

When a balanced 3 phase alternating voltage is supplied to the stator of the induction motor, a resultant rotating magnetic field is established in the airgap of the motor. This rotating magnetic field, with a constant amplitude and speed, induces voltage in the stator and shorted-out rotor circuit, causing currents to flow in the rotor. The induced voltages in the stator and rotor can generally be given by:

$$E_{rms} = 4.44fN_{ph}\Phi_pK_w \quad (2.1)$$

as derived from Faradays Law of Induction, where f is the applicable frequency, N_{ph} is the number of turns per phase, Φ_p is the airgap flux per pole and K_w is the applicable winding factor [9].

The induced rotor currents interact with the rotating magnetic field in accordance with Lenz's Law and the resultant force (torque) produced causes the rotor to rotate in the direction of the rotating field so as to reduce the speed difference between the two. The resultant rotating magnetic field has a speed given by the following equation [9], [12]:

$$n_s = \frac{120f_s}{p} \quad (2.2)$$

Where f_s is the supply frequency and p is the number of poles. The rotor thus spins at a speed n which is less than the synchronous speed n_s . The speed difference between the two is characterized by the slip s , given by:

$$s = \frac{n_s - n}{n_s} \quad (2.3)$$

The currents flowing in rotor circuits also produce a rotating magnetic field that rotates at speed n_s with respect to the stator and sn_s with respect to the rotor itself. The two fields are thus stationary with respect to each other. Their interaction and tendency to align can be thought of as the torque production mechanism in the motor [9].

The rotor current and voltage operate at a different frequency compared to the stator frequency f_1 . The rotor frequency f_2 corresponds to the slip speed and is thus related to f_1 by the equation [9]:

$$f_2 = sf_1 \quad (2.4)$$

2.2.3 Performance characteristics

In the induction motor, the rotor resistance (R_2) plays a crucial role in the behaviour of the machine. The mechanical power (P_{mech}) associated with the motor can be expressed in terms of the slip s and rotor resistance as follows [9]:

$$P_{mech} = T_{mech}\omega_{mech} = I_2^2 \frac{R_2}{s} (1 - s) \quad (2.5)$$

By analysing the equivalent circuit associated with the induction machine, it can be shown that the mechanical torque T_{mech} at a specific speed is proportional to the square of the supply voltage [9]. This is demonstrated in the Torque-Speed profile in the figure overleaf:

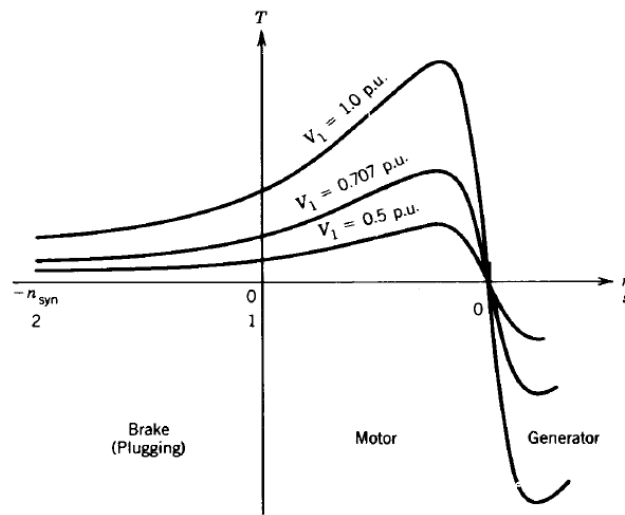


Figure 2-2: Torque versus Speed characteristic for an induction machine at various supply voltages [9].

The maximum or breakdown torque of the machine is independent of the rotor resistance. The rotor resistance has the effect of varying the speed at which the maximum torque occurs [9]. The squirrel cage motor thus has limited adjustability in terms of its torque behaviour. As such these machines are normally divided into classes (A, B, C or D) by the National Equipment Manufacturers Association (NEMA) for the various requirement of industry.

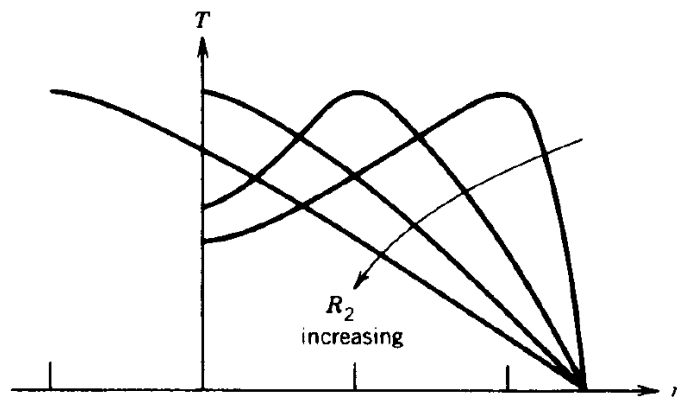


Figure 2-3: Graph of Torque versus Speed demonstrating the effect of changing rotor resistance [9].

2.2.4 Methods of control

Induction motors are ideally suited for processes that require a relatively constant speed such as pump or fan systems. However, in the industrial environment there are often times when variable speeds are required. Induction machines tend to be relatively difficult to control since its torque-speed characteristic is non-linear [10].

To this end, variable frequency converters are required to act as an interface between the induction motor and grid [13]. This concept is depicted in the following figure:

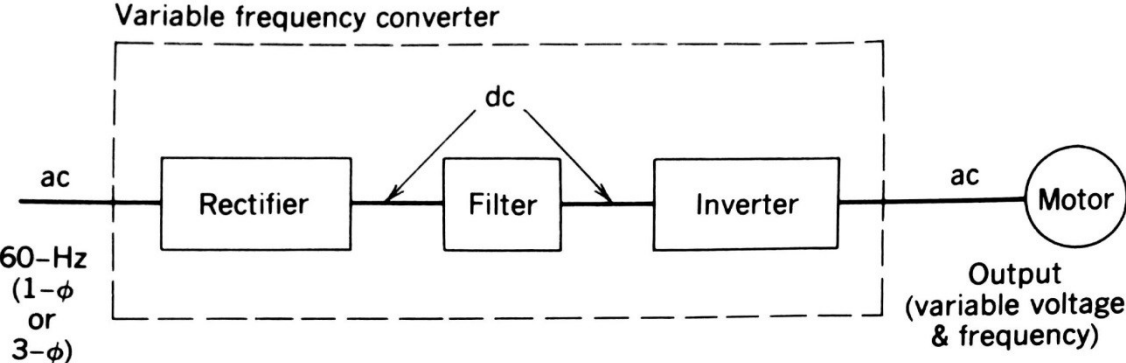


Figure 2-4: Basic concept of supplying variable frequency to an induction motor using power electronics [13].

Speed control techniques for induction motors are broadly divided into open and closed loop control methods. Open loop methods such as Line Voltage and Line Frequency Methods are often employed due to their simplicity. However, closed loop methods naturally provide more accurate speed control due to the process feedback incorporated into the control scheme [9].

Modern inverter drives for induction machines typically employ closed loop control methods without the need for speed feedback from a tachometer [13] and usually have user selectable modes such as speed, torque, flux or volts per hertz control schemes. The inverter drive used during this study was configured for constant volts-per-hertz operation. With this method, the airgap flux density is kept constant by controlling the ratio of supply voltage to frequency, since the torque developed by the motor is proportional to the square of the airgap flux for a given rotor frequency [9]. For frequencies up to the rated frequency, the airgap flux is kept constant and the motor is operated in a constant torque mode. Beyond the rated frequency, the voltage is limited and the airgap flux is consequently weakened, resulting in constant power operation [13]. This method of speed control is depicted in the Figure 2-5 overleaf:

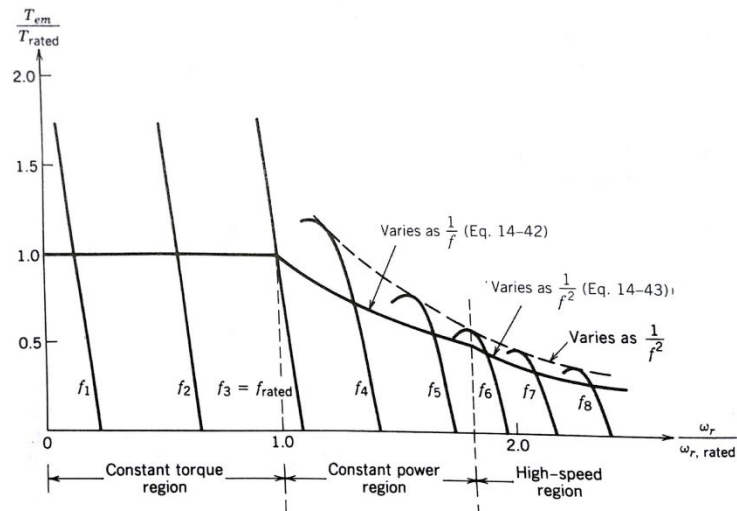


Figure 2-5: Torque versus speed graph showing constant volts per hertz control scheme [13].

2.3 Induction Motor Faults

Though induction machines are widely used in all industries due to their ruggedness and simplicity, they are still subject to failure. These failures manifest for various reasons such as design, manufacturing, loading, maintenance and environmental conditions. Faults can be broadly categorized into electrical faults such as stator winding faults and rotor cage faults; and mechanical faults such as bearing defects, alignment and eccentricity faults [14]. According to the Industry Assessment Study conducted by EPPRI [15], the major component failure percentages associated with the motors in the study are as follows:

Table 2-1: Failure statistics of motors by major component according to EPRI [15].

Major Component	Percentage Failures
Bearing related	41%
Stator related	36%
Rotor related	9%
Other	14%

This study is cited as it includes a healthy sample size of Nuclear Power Stations in the scope of the survey. A similar study conducted by the Power Systems Reliability Subcommittee of the IEEE yielded similar results, with bearing related failures dominating (44%), followed by Stator (26%), Rotor (8%) and other (22%) failures [2]. These faults have several adverse

effects on the machine such as excessive vibration, overheating, torque pulsations, unbalanced voltage and current, and a general reduction in motor efficiency [12]. These imbalances between the mechanical and electro-magnetic forces in the motor (eccentricity) result in additional harmonics in the current spectrum due to the changes in the airgap flux density [14], [16]. This effect will lay the foundation for detecting faults in the machine using the stator current as the medium for detection. With this in mind, the causes of the common induction motor faults are now examined.

2.3.1 Bearing Faults

In applications under 200hp, motors typically use rolling element and ball bearings on the drive and non-drive ends respectively [6]. A typical ball bearing is depicted below, showing its main components, namely outer race (ring), inner race, balls and train containing separators:

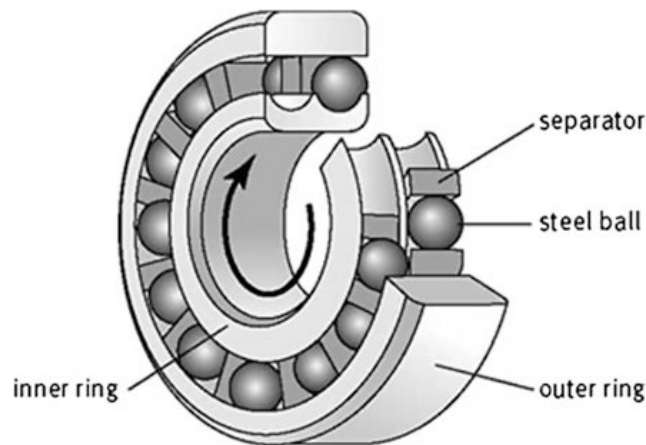


Figure 2-6: Dissection of a typical ball bearing showing its major parts [6].

Bearing defects in motors can be categorised into *Type 1* and *Type 2* faults:

Type 1 defects are localized defects that occur in a specific location in the bearing and produce specific characteristic frequencies. These frequencies are dependent on the motor speed, bearing dimensions and the number of rolling elements [17].

Type 2 defects are distributed and manifest as general roughness of the inner and/or outer raceway. They do not display characteristic faults frequencies and are thus difficult to detect [17].

The main causes of bearing failure are now examined:

Fatigue failure: Bearing fatigue occurs when particles of material are dislodged from the bearing components due to long periods of operation. This progressive fault results in increased levels of noise and vibration [12].

Improper installation, loading and misalignment: By forcing bearings onto the shaft during installation, indentations are formed on the bearing race which results in brinelling [1]. Excessive loading and misalignment causes significant temperature rises which results in annealing of the bearing materials. Additionally, brinelling can occur if the elastic limits of the materials are reached [12], [6].

Contamination and corrosion: The contamination of lubricants by foreign debris and the consequent sanding action on the bearing surfaces is one of the leading causes of bearing failure. Corrosion of bearing material due the motor being exposed to corrosive atmospheres or fluids also has a similar effect and consequence [6], [1], [12].

Improper Lubrication: Adequate lubrication is essential for efficient bearing operation. Under or over lubrication results in high bearing temperatures and surface abrasion due to the deterioration of the lubricant [1], [12].

2.3.2 Stator Faults

Stator faults have the second highest failure prevalence in induction motors and are related to failure of the motor insulation. In low voltage applications, it is generally accepted that insulation degradation cannot be ascertained using online measurements until a fault appears. This is in contrast to high voltage motors where Partial Discharge tests can reliably detect insulation degradation [1], [18]. In low voltage applications, the faults can be classified as follows [12], [18], [4]:

- *Turn-to-turn faults*
- *Coil-to-coil faults*
- *Phase-to-phase faults*
- *Phase-to-earth faults*
- *Open circuit faults*

The less serious turn-to-turn faults usually progress to the more serious ones over a period of time, and result in complete motor failure and its removal from service due to the operation of the protection scheme [1]. The different types of stator faults are illustrated in the figure below:

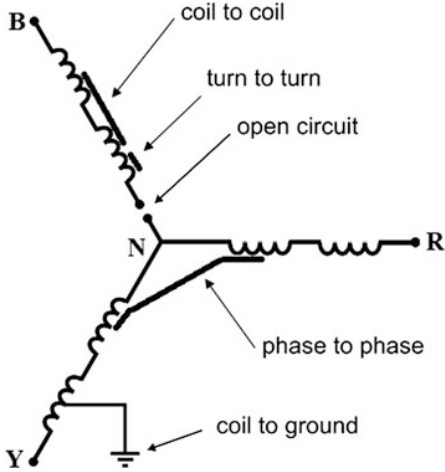


Figure 2-7: Three phase AC motor winding showing different types of stator faults [12].

Insulation failure and the resultant stator faults can occur for several reasons that can broadly be classified into Mechanical, Electrical, Thermal and Environmental stresses [12], [4].

Mechanical stresses occur as a result of movement in the stator windings. Movement can occur due to the forces experienced by the current carrying conductors and due to excessive vibration. This can cause and exacerbate any slack in the core laminations, slot wedges and joints, as well as loosen bracing of end windings [1], [12], [19].

Electrical stresses such as supply transients and electrical discharges due to faults, switching or lightning have a negative impact on the windings of the motor. Repetitive starting also stresses the stator as the motor can typically draw 6 to 8 times its rated current in the process [9], [1], [12].

Thermal stresses occur due to overloading and the resultant high currents, unbalanced supply, poor cooling and high ambient temperatures [1], [12].

Environmental stresses such as ambient temperature in the area of operation and contamination due to moisture, oil and dirt all affect the insulation on the motor and its susceptibility to faults [1], [12].

2.3.3 Rotor faults

Rotor cage failures make up between 5% and 10% of the total induction machine failures as reported by Nandi [1] *et al.* Rotor cage design and manufacture has changed little over the years when compared to its stator counterpart, with cage rotors essentially being of two types, namely, cast and fabricated. Cast rotors occur mostly in smaller machines, the exception being cast ducted rotors in larger machines. Cast rotors are more rugged than fabricated ones used in large machines, but are not repairable [20], [1].



Figure 2-8: Cast rotor showing broken rotor bars [18].

Some of the main causes of rotor cage failure are:

- *Manufacturing defects* resulting in residual stresses in the rotor components.
- *Thermal stresses* due to hotspots, unbalance and thermal overloading due to beyond-design duty cycles.
- *Mechanical stresses* due to defective bearings, fatigued parts and slack laminations
- *Magnetic stresses* caused by unbalanced magnetic pull and vibration.
- *Dynamic stresses* due to centrifugal forces, pulsating torques and cyclic stresses such pulsating mechanical loads.

Rotor cage faults are problematic since they are progressive in nature. This is due to the fact that the rotor bars adjacent to the broken one has to conduct the current due to the breakage. This in turn leads to additional stress on the adjacent bars, thus compounding the problem [20], [1], [12], [6], [5].

2.3.4 Eccentricity related faults

Under ideal conditions, the rotor of the machine rotates coaxially with the stator which results in a completely uniform airgap flux distribution. However, in practice this is not the case as even new machines have some degree of airgap non-uniformity. This condition is known as airgap eccentricity and results in an unbalanced magnetic pull on the rotor. Under severe conditions and most likely at startup, this can result in contact between the rotor and the stator surfaces [1], [12].

Two types of eccentricity faults are distinguished, namely, static and dynamic eccentricity. With static eccentricity, the point of minimum airgap length remains constant in space relative to the position of the stator [1]. In the case of dynamic eccentricity the axis of rotation of the rotor and weight distribution axis are not the same. This results in the position of minimum airgap length rotating with the rotor [12].

The causes of airgap eccentricity in motors can be ascribed to the following causes [1], [12], [4]:

- Imperfect shape of the stator (ovality)
- Incorrect positioning and alignment of the rotor and stator
- Bending in the rotor shaft
- Wear in the bearings

The major faults associated with the induction machine have thus been covered. The next section examines the ways and means to effectively avoid these common faults and failures.

2.4 Maintenance in the Nuclear Power Station Environment

2.4.1 Background

The Nuclear Power and related industries are highly regulated industrial environments due to the risks and consequences associated with the technology. With the establishment of the International Atomic Energy Agency (IAEA) in 1957 and the subsequent adoption by member states of the internationally binding Convention on Nuclear Safety, the industry has taken great strides forward in safety due to improved international policy co-ordination [21]. In its mission of promoting co-operation and the highest safety standards amongst members, the organization publishes Safety Standards and Safety Guides that are based on the Fundamental Safety Principles [22]. Though these documents are not legally binding, it is up to member states to promulgate laws and regulations grounded in these documents to ensure an effective nuclear policy framework, including the establishment of an independent nuclear regulator.

With this in mind, the South African nuclear power industry is subject to the laws and regulations as contained in the Nuclear Energy Act 46 and NNR Act 47 of 1999. *Safety Standards Regulation R388* specifically states as one of its *Requirements for Nuclear Installations* that a maintenance and inspection program needs to be established. Hence at Koeberg Nuclear Power Station, South Africa's only nuclear power station, compliance with the maintenance and inspection provisions forms part of its license conditions [23].

2.4.2 Approach to Maintenance

The nuclear industry has traditionally used the Planned or Periodic Maintenance strategy since the 1980's. This is a logical consequence of the periodic bi-annual refueling required by nuclear power stations which provides an opportunity for other plant maintenance to be performed. During the 1990's, the maintenance strategies at nuclear facilities evolved considerably with the focus shifting to periodic maintenance with a Reliability Centered Maintenance approach. Since then, with guidance from the IAEA, the industry has improved on its maintenance strategies by incorporating Predictive Maintenance technology into plant maintenance [5].

Due to the high cost of maintenance in the nuclear environment, the industry has moved towards a Condition Based Maintenance strategy, which is effectively the evolution and

culmination of previous maintenance methodologies. It can be defined as a process that requires technology, people and the effective use of all available plant data to make informed decisions towards preventive maintenance of plant equipment. It relies heavily on predictive techniques such as condition monitoring to ascertain the state of the equipment and plan maintenance interventions for maximum benefit and least cost [5].

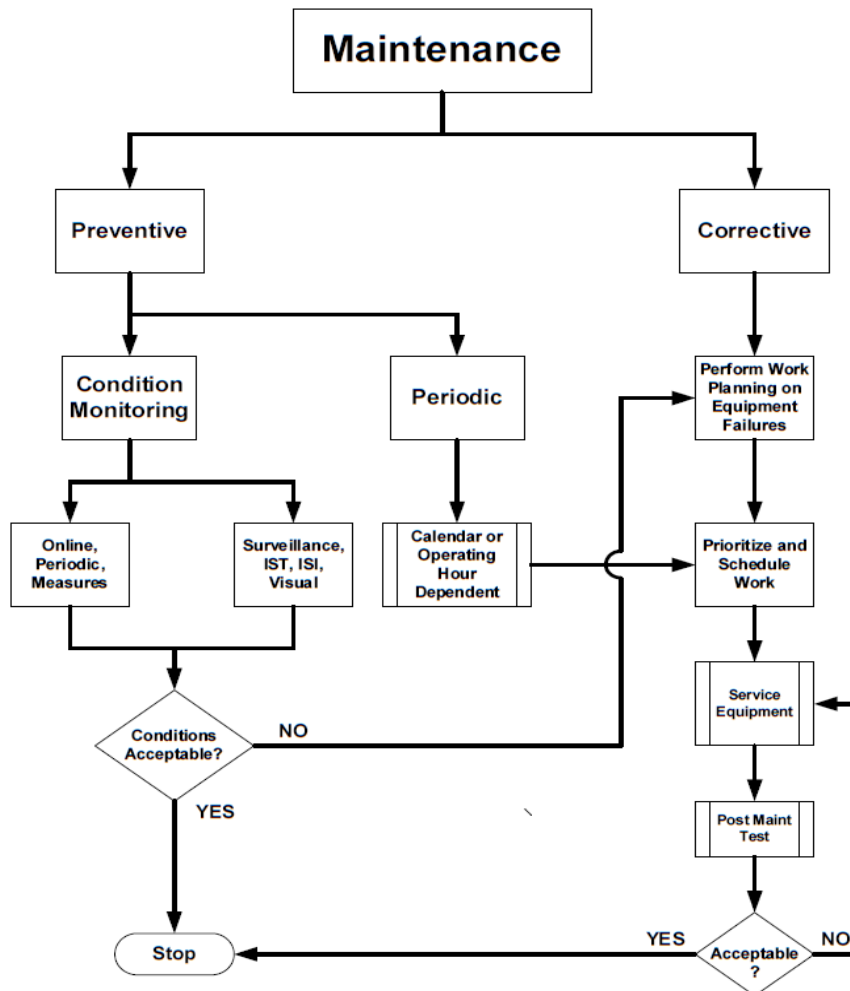


Figure 2-9: Maintenance strategy of a nuclear power station as per IAEA guidelines [5].

Some of the benefits associated with implementing condition based maintenance are [24], [5]:

- Long term reduction in operating costs since unnecessary maintenance is avoided and informed economic decision can be made based on qualitative data.
- Longer intervals between maintenance, increased Mean Time between Failures, improved machine availability and the avoidance of catastrophic failures.
- Reduced inventory of spare parts and the ability to carefully plan manpower requirements based on informed failure predictions.
- The techniques can be used as quality control for repaired and new equipment, thus avoiding early or infant failures.

2.4.3 Condition Based Maintenance of Induction Motors

A typical pressurized water nuclear reactor power plant typically has of the order of 1000 installed motors. As such, all the motors in the population are not mission and safety critical. Hence, EPRI recommends that nuclear plants implement a tiered approach to motor maintenance as part of the Condition Based Maintenance strategy. The approach suggests dividing the motor population into 4 tiers, namely, *Minimum Maintenance*, *Moderate Maintenance*, *Trendable Maintenance* and *Extensive Maintenance*. These tiers are based on evaluation criteria such as safety significance, economic significance, regulatory issues and radiation environment *etc.* [4].

The Minimum and Moderate tiers typically contain motors where faults can be tolerated, and are typically run to failure, despite the application of annual or bi-annual condition monitoring techniques in the Moderate tier. Motors that fall into the Trendable Maintenance tier form the majority of plant motors. Their failure is deemed undesirable and they usually have a broad range of conditioning monitoring techniques applied to them due to the broad variations in size and type. Some of the main condition monitoring techniques applied to this tier of machines are vibration monitoring, thermography, oil sampling, winding and insulation resistance and current monitoring [6], [4], [5].

Motors in the Extensive Maintenance tier are usually safety critical and typically medium voltage with extensive monitoring instrumentation installed. A typical example would be the Reactor Coolant Pump motors in the primary loop of a Pressurized Water Reactor. In addition to the techniques used in the Trendable tier, these motors also typically incorporate testing techniques such as Step DC Hipot, Partial Discharge Testing and periodic external inspections as part of the condition monitoring regime [6], [4], [5].

Most nuclear installations use some form of priority when it comes to motor maintenance, with vibration and thermal monitoring being the most commonly applied techniques [4]. Condition monitoring techniques as they apply to squirrel cage induction motors will now be presented.

2.5 Induction Motor Condition Monitoring Methods

From the previous section it is apparent that condition monitoring forms the backbone of any effective Condition Based Maintenance system. The techniques used for condition monitoring of induction motors tend to be varied, with each having its unique advantages, disadvantages and economic payoff periods [1], [5]. These techniques are now reviewed in detail, with a view of their application in nuclear installations.

2.5.1 Vibration Monitoring

Vibration in equipment can be understood as the repetitive movement of the equipment about an equilibrium position [5], [24]. All rotating equipment, whether healthy or new, have an inherent vibration level. The magnitude of this vibration is a function of the forces acting on the equipment or machine and the response of its structure and mountings to these forces. Vibration monitoring as a condition monitoring technique is concerned with the changes in levels of vibration, both generally and at specific frequencies [14].

In vibration monitoring there are three possible measurands, namely, displacement, velocity or acceleration. In order to measure these quantities and convert the mechanical motion into an electrical signal, one would require a Proximity Probe, a Velocity Probe or an Accelerometer respectively [5], [25]. Each of these devices provides very specific information and has inherent limitations. Hence, selection of the appropriate type and its placement on the machine is critical to achieving the desired outcome [24].

The vibration levels of the machine are then monitored against established acceptable levels for alarming and trending purposes. The International Standards Organization's standard ISO 20816-1:2016 [26] provides practical guidelines to this effect. The time domain electrical signals can also be filtered and converted via the Fourier Transform into the frequency domain for detailed spectral analysis of the data. The spectra are then analysed and compared to baseline machine data to determine the presence and nature of the faults [5]. This is usually a manual process that requires expert knowledge, but can also be automated through the application of artificial intelligence techniques such as neural networks [27].

One of the main advantages of vibration monitoring is that it provides clear insight into common mechanical problems due to the clarity or directness with which the dynamic forces act on the machine components and hence the transducers [24]. Bearing faults at the incipient stage usually produce low energy signals, thus making their detection difficult [28]. To this end, several advanced techniques have been developed to increase the detection accuracy and to automate the task of identifying the fault features. Techniques such as Order Tracking as suggested in [29] can be used to remove the speed dependency of vibration signals. According to Wang *et al.* [30] methods using Kurtosis and Root Mean Squared Functions are the most commonly used parameters to quantify vibration signal features. The application of wavelet analysis, envelope detection and cyclo-stationarity to filtering methods and the design of band-pass filters for pre-processing data have also been studied extensively [30].

2.5.2 Temperature Measurements

The temperature of equipment is frequently the most monitored parameter in the industrial and nuclear environment. As part of typical plant condition monitoring schemes, the temperature of motor bearings and stator windings are monitored and trended. Hence, abnormal temperatures are a strong indicator of developing problems [5]. Depending on the size of the motor, temperature instruments are normally integrated into the components of larger high voltage motors [6].

Temperature measurement methods can essentially be divided into two types, namely *Contact* and *Non-contact* methods. Contact methods typically use instrumentation such as Thermocouples and Resistance Temperature Devices (RTD's) such as Pt100's and Thermistors that are in direct contact with the component to be monitored [5], [6].

Non-contact temperature measurement techniques involve the measurement of infrared radiation emitted by all bodies above absolute zero. The emissivity of the body or equipment is related to the temperature of the body [31]. Infrared Thermography can be described as the visualization technique that converts the infrared energy emitted by an object into the temperature of the object [32]. Temperature measurements using IRT are sensitive to several factors such as emissivity of the object, distance, environmental conditions and camera specifications [33].

It has the natural advantage of being remote from the object, non-intrusive, fast and provides a view of the thermal distribution [5]. As such, this technique has reportedly been used extensively in the nuclear industry as reported by Lewak in [34]. Some areas of application as reported by the U. S. Department of Energy are in the Predictive Maintenance program of the Savannah River Site which processed high level nuclear waste. Here, IRT was used extensively on electrical and mechanical equipment associated with the tank systems such as fan motors, slurry pump assemblies and electrical connections [35].

IRT has mostly been used on static equipment such as transformers, cables, connections, with limited applications to induction machines [5]. The technology does lend itself to increased use since motor faults usually cause an increase in motor temperature, either generally or near the fault location [33]. The IAEA and EPRI highly recommend that IRT be incorporated into the Condition Based Maintenance Strategy with respect to motors, especially those that fall into the Moderate and Extensive Maintenance tiers [4], [5].

2.5.3 Axial Flux Related Methods

Another common condition monitoring method for the detection of faults in induction machines is through the use of axial flux measurements [1]. An ideal machine with perfect symmetry will have no axial flux. However, since all machines have inherent dissymmetry, axial flux measurements are indeed possible [36]. Measurements are made by mounting search coils in the four quadrants of the motor, either internally or externally. Another method as presented by Penman [37] is to mount a search coil concentrically with the rotor. When a fault occurs in the machine, the axial flux distribution in the machine changes and a voltage proportional to the change in the axial flux is generated. These signals are then analysed through spectral analysis to detect the changes in fault components [38].

Penman [37] successfully detected shorted turns and was also able to detect the position of the faults through quadrant mounted coils. Ewert [36] was able to detect shorted turns as well as faulty rotor bars using Axial Flux Monitoring. Behbahanifard [19] also reports that the technique works well even in the presence of switching noise in an inverter driven motor. Chen [38] in a review of the topic mentioned two successful studies at detecting bearing faults using flux monitoring methods. However these required custom probes. More recently Zhang [39] employed a method of axially mounting 8 coils directly in the stator frame to directly detect changes in airgap flux density for the purposes of detecting

bearing faults. Using Principle Component Analysis, bearing faults were reportedly successfully diagnosed in an oil pump assembly.

2.5.4 Acoustic Methods

Acoustic analysis of equipment deals with the generation, transmission, reception and effects of sound. Most machines usually have a consistent acoustic output under steady state operation. The sound emitted under operation can typically be divided into the Sonic (0 - 20kHz) and Ultrasonic (20kHz - 1MHz) ranges. As they age and degrade in operation, the acoustic signatures of machines change. This makes acoustic methods suitable for condition monitoring purposes [5]. Tandon [40] has listed the three acoustic techniques suitable for the condition monitoring of machinery, especially induction machine bearings [7]. These techniques are Acoustic Emissions, Sound Pressure and Sound Intensity Techniques.

Acoustic Emission (AE) involves detecting the ultrasound waves generated by the release of strain energy due to structural changes in materials under mechanical or thermal stress. These high frequency signals of greater than 50kHz are generated primarily by the propagation and generation of cracks and are measured using highly sensitive piezoelectric or strain gauge sensors [5]. The main parameters measured for AE are peak amplitude, ring down counts and events [40]. The main advantage of AE is that it is able to detect sub-surface cracking in bearings, even before it appears on the vibration spectrum [7]. Yadava [7] demonstrated that AE was the most sensitive technique that registered the largest change in normalized levels when detecting induction motor bearing faults. This result was in comparison to Vibration Analysis, Motor Current Signal Analysis and Shock Pulse Methods. The IAEA reports [5] that Acoustic Emission techniques are successfully used in the nuclear environment on Reactor Vessels and related piping, as well as on the Control Rod Housings to monitor the degradation of the metal.

Acoustic Noise Measurement techniques involve the measurement of Sound Pressure or Sound Intensity. These methods can be used to detect the acoustic noise emanating from bearings [5], [7]. Li [41] analysed acoustic, vibration and current spectra for an induction motor with outer bearing race fault and successfully detected the fault in all cases. However, the Sound Pressure measurement showed clearest results spectrum with the least harmonics in the lower frequencies of interest. Sound Pressure measurements

typically have the drawback of being affected by ambient noise, which requires attention before measurements can be made [40]. In comparison, Nakra [42] concluded in a study related to rolling element bearings that Sound Intensity is a more effective method for analysing bearing faults.

2.5.5 Motor Current Signature Analysis

Motor Current Signature Analysis (MCSA) is a condition monitoring technique whereby the stator currents of the motor are captured and analysed for the purposes of fault detection [16]. In this method, the motor itself acts as the transducer to convert physical faults to electrical signals. Motor current is measured remotely and non-intrusively typically using a clamp-on ammeter or current transformer [5]. Faults in the machine create harmonics in the stator current due to its interaction with the airgap flux and the resultant backward rotating field [43]. Spectral analysis of the stator current then ensues whereby the fault frequency components are examined for changes from the baseline values [5], [8].

This constitutes a great advantage over other methods such as vibration monitoring, which require direct access to the motor [44]. This advantage can be leveraged in a nuclear environment where accessibility is limited especially in areas of high radiological risk. To this end the IAEA [5] as well as EPRI [6] recommend incorporating MCSA into plant condition monitoring processes, especially for critical motors such as the Reactor Coolant Pumps that have large flywheels and long start up times that stress the rotor.

Fault detection methods in induction machines using MCSA can effectively be divided into three groups, namely, feature extraction based methods; model based methods and knowledge based methods. Feature extraction methods utilise various analysis techniques to detect the changes introduced by fault conditions. Some of the main methods are now discussed:

Fast Fourier Transform

The acquired current signal data is converted into the magnitude data in the frequency domain through the use of the efficient Fast Fourier Transform algorithm. Spectra produced using the FFT can suffer from the effects of aliasing and spectral leakage. These issues can usually be overcome through correct sample rate selection and

applying appropriate windowing functions to the spectral data [8]. Additionally, FFT based processing can only be applied to relatively stationary signals [16].

Park's Vector Approach

This method processes the three phase stator currents into a two dimensional representation using the Park's Vector. For a healthy motor, when the Park's Vector is plotted on the two dimensional $d-q$ plane, it plots a circular locus with its centre at the origin [45]. When a fault is experienced by the motor, the shape of the locus plotted by the Park's Vector is changed. The deviations from the reference patterns can then be used for fault diagnosis [16]. Cordosa *et al.* [45], [46], [47] reported the successful detection of single phasing faults, inter-turn stator faults and open wound rotor faults using the Park's Vector Approach.

The Enhanced Park's Vector approach builds on the original method and recognises that under fault conditions, the Park's Vector modulus will contain a dc and ac component due to the asymmetries introduced by the fault. Spectral analysis of the ac component then reveals further information about the extension of the fault with a clear frequency component at $2f_s$ [48]. This technique utilises all three motor currents and provides an improvement in fault discrimination when compared to classical FFT based analysis [16]. Cruz *et al.* [48], [49], [50] reported the successful detection of stator winding faults, rotor cage faults, unbalanced supply voltage, misalignment faults as well as bearing faults using the technique.

Bispectrum Technique

The Bispectrum Technique forms part of the field known as Higher Order Spectral Analysis. These statistics are known as Cumulants and provide amplitude as well as phase information about a process [51]. It also automatically suppresses additive Gaussian noise thereby increasing signal-to-noise ratio. These statistics also provide useful tools to detect non-linear systems and are able to extract phase relations [52], [53]. This provides an additional dimension to fault detection over traditional FFT [16]. The technique first computes the third order Cumulant sequence from the stationary time domain signal, whereupon a 2-D discrete Fourier Transform is performed. Benbouzid [16] recommends the technique particularly for electrically based faults in

induction machines. Chow [54] has also reported successful detection of supply unbalance faults using the Bispectrum Technique. Arthur *et al.* [53] have also theoretically verified the reliability and robustness of the technique to create a commercially viable automated fault detection system that does not require *a priori* data. More recently Li *et al.* [52] used an enhanced Bispectrum method with an auxiliary frequency injection to accentuate the fault frequencies, to successfully identify outer bearing race faults in induction motors.

High Resolution Spectral Analysis

Due to the need for increased spectral resolution from classical estimation techniques, researchers turned to subspace methods that are based on Eigen decomposition of the autocorrelation matrix of the signal to be studied. It assumes that the discrete current signal in this instance can be represented by a finite sum of sinusoids and white noise [16]. Boudinar *et al.* [55] noted that this model sufficiently represents the current signal in the discrete time domain. The multiple signal classification (MUSIC) and Root-Music Eigenanalysis-based classifiers have been used successfully to diagnose broken rotor bars [56]. Morinigo-Sotelo [57] has also applied the technique to the zero sequence current of an induction motor and proved the technique to be highly sensitive to rotor bar failures. Boudinar *et al.* [55] reported that the technique proved to be highly discriminative in detecting bearing faults in the tested induction motor. Benbouzid *et al.* [16], [58], [56] noted that the technique is particularly useful where the fault frequencies coincide with and modify main spectral components, since the MUSIC algorithm maintains only the main frequency components, thus also reducing noise.

Wavelet Analysis

Due to classical FFT analysis only being effective under steady state conditions, alternative techniques are required to analyse transient phenomena in induction machines [16]. Researchers turned to alternative methods such as the Short Time Fourier Transform to deal with transient conditions. This method, which effectively windows the input signal such that it converges to zero at its endpoints, received mixed results in practice. This was due to the limitation of the technique using a fixed window size, which results in increased cycles at higher frequency [59]. Wavelet theory provides a solution to this problem since the technique automatically adjust the window for low

and high frequencies. At low frequency the technique uses long windows and at high frequency the technique uses short windows, thus using time dilation and compression as opposed to frequency variations.

The Discrete Wavelet Transform is usually used since incoming data is digitised. The technique can be used for signal decomposition, which is useful for fault detection, as well as for signal reconstruction [60]. In the field of induction motor current signature analysis, wavelet theory has largely been used to examine transient stator current for fault detection. Douglas *et al.* [59] have used the technique in conjunction with an active tracking filter to remove the fundamental from the start-up transient, thereby allowing analysis of the residual to effectively detect a broken rotor bar condition. Similarly, Ye *et al.* [61], [62], [63] using Wavelet Packet Decomposition successfully diagnosed shorted turns, airgap eccentricity and broken rotor bars at various machine loads. In [64], Barendse *et al.* applied wavelet analysis to the ac component of the (Enhanced) Park's Vector Modulus to successfully detect induction motor inter-turn faults during transient conditions. Similarly in [65], incipient bearing faults were successfully detected using the combined approach, and in [66] through using Wavelet Packet Decomposition.

Instantaneous Power Analysis

Instantaneous Power Analysis is another fault detection technique which builds on current signature analysis by including the product of the line voltage. The advantage presented by using the instantaneous power for diagnostic purposes is that its spectrum contains a unique component known as the characteristic frequency, besides the sideband components, which provides an additional piece of information about the motor [67]. The effect on the harmonics is that they are translated into the lower frequency range, typically between 0-100Hz, which represents a great advantage [16]. This technique will be covered in detail in a subsequent chapter.

Trzynadlowski *et al.* [68] initially tested the technique and managed to detect mechanical faults such as misalignment, imbalance and rotor eccentricity. De Tomaso *et al.* [69], reports success in detecting broken rotor bars even in lightly loaded conditions in a comparison with MCSA. Drif *et al.* [70] reports using instantaneous active and reactive power to detect shorted turns in an induction motor, noting that the instantaneous reactive power was more sensitive than the current. Ibrahim *et al.* [28]

successfully detected bearing faults in an induction motor using instantaneous power and instantaneous power factor, with the latter being touted as being superior.

Motor Square Current Signature Analysis

Motor Square Current Signature Analysis (MSCSA) is a newer technique suggested by Pires *et al.* [71], [72]. This technique uses the square of the instantaneous current and produces similar spectra to those produced by using the instantaneous power. The spectra thus also contain two main components, namely, a dc component and a component at $2f_s$ [71], [73]. Pires *et al.* [71], [72], [74] successfully used the technique in comparison to traditional MCSA to detect inter-turn faults, eccentricity related faults, as well as broken rotor bars. This technique will be elaborated on in the subsequent chapter.

Artificial Intelligence based methods

One of the criticisms levelled at MCSA is that it requires expert knowledge to interpret the results of the spectral analysis performed on the input signal. Thus, human intervention is required. In automated systems, extracted features from spectral analysis are usually compared to lookup tables for threshold detection. However, this method is not efficient when dealing with non-linear phenomena as in the case of the induction machine [75]. Artificial Neural Networks and Fuzzy Logic have been used to model systems which are hard to describe mathematically, or too cumbersome to compute when the mathematical model exists [76]. Hence, there has been much research in the use of artificial intelligence techniques to serve as the decision making tool in fault detection schemes [1].

Neural Network-based algorithms have been used extensively in the literature to discriminate between healthy and faulty motor conditions. This method of processing motor data involves a learning process with the network responding by adapting its weighting factors according to the learning rule [77]. This learning process has been cited as a drawback of the method due to time and fault data availability constraints. However, with the development of Continual Online Training, which allows re-weighting on a moving basis, this obstacle has been partially overcome [75]. Martins *et al.* [78] used an unsupervised neural network to detect stator faults and their extent without

using the FFT in the algorithm. Similarly, Schoen *et al.* [79] used an unsupervised neural network in conjunction with a rule-based frequency filter to detect rotor eccentricity and bearing damage. In [80] Ballal *et al.* used an adaptive neural fuzzy inference system with five inputs (current, speed, winding temperature, bearing temperature and noise) to diagnose inter-turn and bearing faults with a 96% accuracy. Nejari and Benbouzid [47] demonstrated the use of the Park's Vector approach in conjunction with a feedforward neural network. By training the network through back propagation, the system was able to detect voltage unbalance as well as open phasing of the machine. Sadeghian *et al.* [81] were able to detect broken rotor bars by using wavelet packet decomposition and feedforward neural networks.

2.6 Concluding Remarks

The preceding sections have covered constructional, operational and technical aspects of the induction motor and its most common failure modes and causes. It then proceeded to cover the need for condition based maintenance with a view of its applicability to nuclear installations. Various condition monitoring techniques were covered and explained, including motor current signature analysis. The various processing techniques associated with motor current signature analysis were reviewed together with important results from essential literature in the field.

3 Theory Development – Fault Signatures and Signal Processing Techniques

3.1 Introduction

In the previous chapter, the induction motor and condition monitoring thereof was reviewed. Spectral analysis of the motor current was discussed in detail. This chapter will now present the theory to be used as the basis for this study.

3.2 Analysis Techniques

Three methods have been selected and their merits and theory with respect to the common motor faults will now be detailed:

3.2.1 Motor Current Signature Analysis

Motor Current Signature Analysis (MCSA), as explained in chapter two deals with analysing the stator current of the motor for signatures indicative of motor faults. The motor faults cause backward rotating harmonic torques which affect the airgap flux, thus allowing its detection in the stator current [43]. This technique will form the basis of this study and the reference for comparison with other techniques.

3.2.2 Instantaneous Power Signature Analysis

Instantaneous Power Signature Analysis (IPSA) is a variation from classical MCSA and utilises the instantaneous power as a medium to detect motor faults. Spectral analysis of the instantaneous power reveals unique components associated with the motor faults and translates the fault components into the lower end of the frequency spectrum [67]. This will be the second technique used to analyze the motor faults and will be compared with the current analysis. In steady state, the instantaneous power can be given by the following equations [82]:

$$\text{Line Voltage} \quad u_{ab}(t) = U_{ml} \cos(\omega_1 t) \quad (3.1)$$

$$\text{Line Current} \quad i_a(t) = I_{ml} \cos(\omega_1 t - \varphi) \quad (3.2)$$

$$\text{Instantaneous Power} \quad p(t) = \frac{3}{2} U_{ml} I_{ml} [\cos(2\omega_1 t - \varphi) + \cos(\varphi)] \quad (3.3)$$

Where U_{ml} is the maximum line voltage, I_{ml} is the maximum line current, ω_1 is the supply frequency and φ is the phase angle of the supply current. From equation (3.3) one is able to deduce that the instantaneous power spectrum contains a dc component and a fundamental component at $2f_1$ [67] [82].

3.2.3 Motor Square Current Signature Analysis

The third technique to be used in this study will be Motor Square Current Signature Analysis (MSCSA). The technique as presented by Pires *et al.* [71], [72], [73] uses the square of the instantaneous stator current in the same manner as classical MCSA, but reveals spectra with similar features as the instantaneous power. The square of the line current can be described by the following equations:

$$i_a(t) = I_{ml} \cos(\omega_1 t) \quad (3.4)$$

$$i_a^2(t) = \frac{I_{ml}^2}{2} + \frac{I_{ml}^2}{2} \cos(2\omega_1 t) \quad (3.5)$$

From equation (3.5), the square current equation reveals a dc component and a fundamental component at $2f_1$, similar to the instantaneous power [71].

3.3 Fault signatures

The three techniques namely MCSA, IPSA and MSCSA were selected for a comparative study as they are fairly simple to implement, non-intrusive and are similar in nature, thereby facilitating a comparison. The motor faults covered in this study together with the signatures associated with each technique are now presented.

3.3.1 Stator faults

According to industry research, induction motor stator faults produce the second highest number of incidents. Hence, the detection of incipient faults within the stator is critical as the timeframe for progression from inter-turn fault to full winding failure is a function of many variables and as such has not yet been resolved [83].

MCSA

When analyzing the stator current in low voltage motors affected by inter-turn faults, harmonic frequencies are produced due to the asymmetry between the three phases. These frequencies can be described by the following equation [1], [18], [84]:

$$f_{st} = f_1 \left[\frac{n}{p} (1 - s) \pm k \right] \quad (3.6)$$

Where f_{st} are the frequency components that are functions of the shorted turns, f_1 is the supply frequency, p is the number of pole pairs, s is the rotor slip, $k = 1, 3, 5$ and $n = 1, 2, \dots, (2p-1)$. A typical frequency spectrum of the stator current for a motor with an inter-turn fault is shown below:

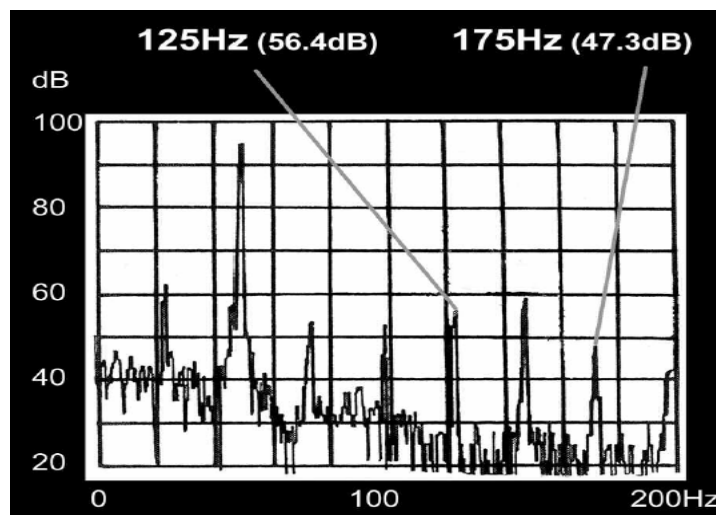


Figure 3-1: Frequency spectrum of stator current showing inter-turn fault components [18]

MSCSA

According to [72], the fault components for inter-turn faults using square current analysis can be found by substituting the upper and lower sideband currents at frequencies given by equation (3.6) into equation (3.5) for the square of the current. This yields the following equations [72]:

$$f_{st1} = 2kf_1 \quad (3.7)$$

$$f_{st2} = 2f_1 \left[\frac{n}{p}(1-s) \pm k \right] \quad (3.8)$$

Due to the limited quantity of literature on the subject of square current analysis, the fault component frequencies for inter-turn stator faults were derived and verified using the aforementioned process. A detailed derivation of these equations can be found in Appendix C.

IPSA

According to [70], stator faults affect the electrical, magnetic and mechanical properties of the motor such that it gives rise to a torque ripple at $2f_1$, thus making the instantaneous power, which itself contains a $2f_1$ component, suitable for the detection of stator faults. This produces disturbance frequencies in the instantaneous power spectrum given by:

$$f_{st1} = 2kf_1 \quad (3.9)$$

It is noted that this is the same equation as (3.7) derived using square current analysis. In the absence of additional literature on the subject of stator faults using the instantaneous power spectrum, and given its similarity to MSCSA, it can reasonably be inferred that the fault component equation (3.8) from the square current analysis should also be applicable in this instance. This inference will be tested experimentally.

3.3.2 Broken Rotor Bar Faults

The second fault type to be examined in this dissertation will be that of an induction motor with broken rotor bars. Rotor cage related faults make up between 5% and 10% of all induction motor related faults [1]. Broken rotor bar faults in the context of the three detection methods used in this study are now discussed:

MCSA

Rotor asymmetry caused by broken rotor bars in induction motors, results in a backward rotating field in the airgap. This field induces current back into the stator which in turn results in torque and corresponding speed oscillations. This effect produces current components with frequencies given by the following formula [84], [82]:

$$f_b = f_1(1 \pm 2ks) \quad (3.10)$$

Where f_1 is the grid frequency, s is the slip and $k = 1, 2, 3$ etc. This produces a spectrum where there are upper and lower sidebands at $\pm 2sf_1$ around the fundamental and its multiples. The lower sideband can be considered present due to the broken rotor bars, whilst the upper sideband appears due to the resultant speed oscillation [1]. A typical spectrum associated with broken rotor bars is shown below:

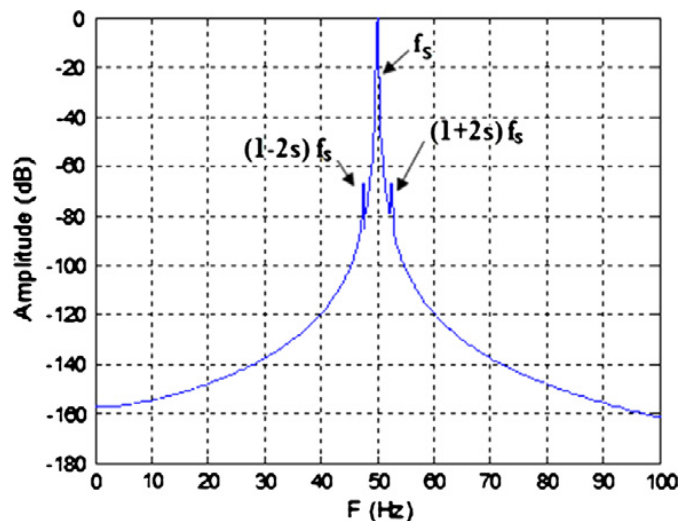


Figure 3-2: Typical frequency spectrum of a broken rotor bar fault in an induction motor [71].

The amplitude of the lower sideband component of $f_1(1 - 2s)$ can be considered to be approximately proportional to the number of broken bars whilst the upper side band $f_1(1 + 2s)$ can provide insight into the severity of the condition. Additionally, it is generally accepted that rotor should be considered healthy if the amplitude difference between the sideband components and the fundamental is greater than 50dB [16].

IPSA

Similar to the method of deriving the stator fault characteristic equations for the instantaneous power, the sideband current components associated with the broken rotor bar in (3.10) are substituted into the instantaneous power equation of (3.3). This derivation reveals several unique frequency components, besides the dc and $2f_s$ components, which can be used for fault detection [82], [85].

$$f_{br1} = 2ksf_1 \quad (3.11)$$

$$f_{br2} = 2f_1(1 \pm ks) \quad (3.12)$$

MSCSA

When including the sideband component of the current into the equation for the square of current in (3.5), the derivation shows additional frequency components that are identical to equation (3.11) and (3.12), thus highlighting the similarity between the square current and instantaneous power spectra [71]. Hence these equations will be used for both methods when evaluating a motor with broken rotor bars.

3.3.3 Bearing faults

Bearing faults are by far the most common cause of failure in induction motors, accounting for almost half of all failures. Bearing failure can be attributed to various factors such as fatigue, improper installation and alignment, overloading, contamination and poor lubrication [6], [1], [12].

MCSA

Type 1 and Type 2 bearing faults effectively cause vibration in the bearing that is detectable via the distortion in the airgap flux, and hence the stator current due to the change in reluctance and flux linkage [8]. Single point defects (Type 1) are known to produce characteristic vibration frequencies that are dependent on the dimensions of the bearing. General roughness defects (Type 2) produce frequency bands in which the fault frequencies manifest [16], [8].

The Type 1 faults can be categorized into inner race faults, outer race faults, ball defect faults and cage defect faults. These faults produce characteristic frequencies given by the following formulae [1], [8], [44]:

$$\text{Inner race fault} \quad f_{irf} = \frac{n}{2} f_r \left[1 + \frac{bd}{pd} \cos\beta \right] \quad (3.13)$$

$$\text{Outer race fault} \quad f_{orf} = \frac{n}{2} f_r \left[1 - \frac{bd}{pd} \cos\beta \right] \quad (3.14)$$

$$\text{Ball defect fault} \quad f_{bf} = f_r \frac{pd}{2 \cdot bd} \left(1 - \left[\frac{bd}{pd} \cos\beta \right]^2 \right) \quad (3.15)$$

$$\text{Cage defect fault} \quad f_{cf} = \frac{1}{2} f_r \left[1 - \frac{bd}{pd} \cos\beta \right] \quad (3.16)$$

Where f_r is rotor mechanical frequency, n is the number of balls, bd is the ball diameter, pd is the ball pitch diameter and β is the contact angle of the balls with the races. These dimensions for a typical ball bearing are illustrated overleaf:

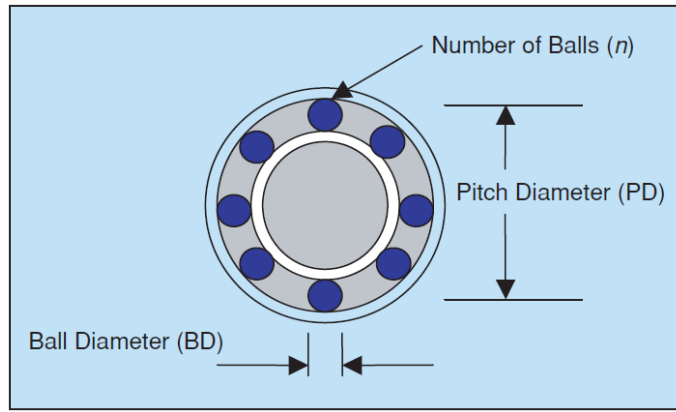


Figure 3-3: Bearing dimensions used for characteristic frequency calculations [77].

These vibration frequencies will then reflect in the current spectrum as follows:

$$f_{bng} = |f_1 \pm m f_v| \quad (3.17)$$

Where $m = 1, 2, 3 \dots$ and f_v is one of the characteristic fault frequencies [86]. The diagram below shows a typical spectrum of actual bearing vibration versus its translation into the current spectrum:

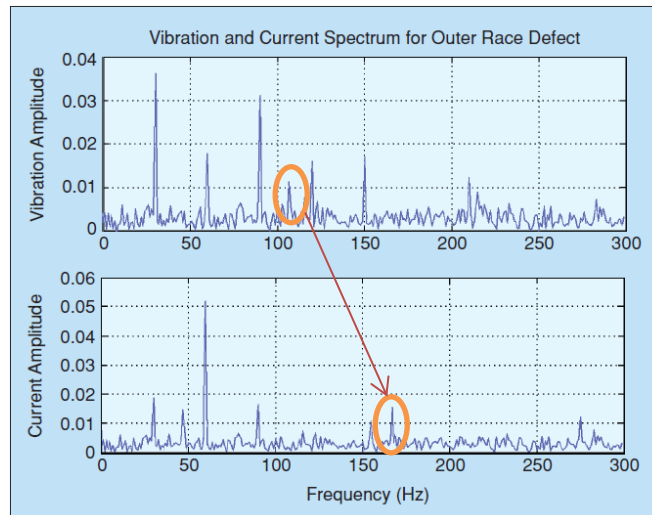


Figure 3-4: Typical outer race bearing defect frequency and its translation into the current spectrum [77].

When exact dimensions of the bearings are not known, the outer and inner race fault frequencies can be approximated by the following formulae for bearings with between 6 and 12 balls [87]:

$$f_{irf} = 0.6nf_r \quad (3.18)$$

$$f_{orf} = 0.4nf_r \quad (3.19)$$

where n is the number of balls. According to ISO 20958-2013, this approximation can also be applied to roller bearings with 12 to 18 rollers [84]. The magnitude of the frequency components associated with the different bearing faults are compared to that of baseline values, where those components will either be absent or significantly lower in amplitude [77].

IPSA

When attempting to detect bearing faults, analysis of the instantaneous power spectrum has the advantage that the faults appear directly at their disturbance frequencies [28], [67]. Hence, the frequencies calculated using equations (3.13) to (3.16) can be sought directly.

MSCSA

Since Motor Square Current Signature Analysis is a relatively new technique, the author found no literature for the technique in applications related to bearing fault detection. However, due to the similarity between MSCSA and IPSA, one could infer that the fault signatures may also appear directly at the disturbance frequencies. This expectation will be tested experimentally in this study.

3.4 Signal Processing Techniques

At the core of MCSA and its counterparts is the processing of the raw data acquired from the induction motor and the estimation of the spectrum associated with the data. The various techniques used in the field of induction motor condition monitoring were discussed in 2.5.5. In this study the analysis of the current, partial instantaneous power and the square current will be done during steady state operation of the motor. The signal processing techniques selected for this task are now presented:

3.4.1 The Fourier Transform and FFT algorithm

The Fourier Transform of a signal effectively represents the signal as the sum of complex exponentials of varying frequencies, magnitudes and phases [88]. The Fourier Transform of a continuous signal $x(t)$ can be stated as [89]:

$$X(\omega) = \int_{-\infty}^{\infty} x(t)e^{-j\omega t} dt \quad (3.20)$$

The inverse transform to synthesize the signal can thus be stated as:

$$x(t) = \frac{1}{2\pi} \int_{-\infty}^{\infty} X(\omega)e^{j\omega t} d\omega \quad (3.21)$$

Since signals are captured digitally, the discrete version of the Fourier transform (DFT) becomes applicable and can be defined for a finite duration discrete signal $x[n]$ as:

$$X[k] = \sum_{n=0}^{N-1} x[n]e^{-jk\omega_0 n} \quad (3.22)$$

$$k = 0, 1, 2 \dots N - 1 \quad \text{and} \quad \omega_0 = \frac{2\pi}{N}$$

And the inverse DFT as:

$$x[n] = \frac{1}{N} \sum_{k=0}^{N-1} X[k]e^{jk\omega_0 n} \quad (3.23)$$

$$n = 0, 1, 2 \dots N - 1 \quad \text{and} \quad \omega_0 = \frac{2\pi}{N}$$

The Fourier Transform of the current signal is implemented using the Fast Fourier Transform (FFT) computational method developed by Cooley and Tukey [90]. The FFT algorithm is computationally efficient and is one of the most utilized signal processing methods for induction motor fault diagnosis [91]. For an N -point transformation, using the resource intensive direct computation method, the time required is proportional to N^2 . Using the FFT algorithm, the computation time is proportional to $N \log_2 N$ [90]. Nonetheless, the FFT has several drawbacks such as sensitivity to signals with a low signal-to-noise ratio, requiring stationary signals and spectral leakage [91].

3.4.2 Windowing and Zero Padding

The FFT algorithm assumes that the signal being processed is periodic, or at least starts at zero and ends at zero in the given period. Since this is rarely the case, spectral leakage occurs, where the energy associated with the signal is smeared out over adjacent frequency bins as opposed to being concentrated at a single point in the spectrum [92]. When attempting to locate and distinguish between closely spaced components in the spectrum the side lobe frequencies caused by the smearing may interfere with each other. A solution to this problem is to apply a window function to minimize the leakage.

A window function typically contains a weighted trigonometric function which starts and ends at zero. Several types of window functions exist, each with different strengths and drawbacks. The most commonly used window in induction motor fault diagnosis is the Hanning Window, which provides good frequency resolution at the expense of amplitude accuracy [91]. Generally, irrespective of the window used, reduction in the sidelobe amplitude results in the widening of the main lobe [93].

To minimize the computational complexity and to smooth the appearance of the spectrum, zeros are added to the sampled data such that the number of samples is an exact power of two [91], [94], [93]. At this point, a periodogram will usually be computed by summing the square of the modulus of the Fourier coefficients, and then finding the average according to the following formula:

$$\mathbb{P}_m = \left| \frac{1}{N} \sum_{n=0}^{N-1} x[n] e^{-jk\omega_o n} \right|^2 \quad (3.24)$$

$$k = 0, 1, 2 \dots N - 1 \text{ and } \omega_o = \frac{2\pi}{N}$$

This produces a power spectrum where the peaks are proportional to the power of the sinusoid processes [93].

3.5 Concluding Remarks

This chapter has described the theory behind the selected techniques and the derivation of the frequency components associated with the three faults types to be analysed in this study. The classical signal processing techniques that will be applied to this study were also briefly reviewed.

4 Experimental Setup and Testing Methodology

4.1 Introduction

Having covered the theory to be applied in this study, this chapter details the test equipment and methodology used in the execution of the experiments.

4.2 The Induction Motor Test Rig

In this study, all tests were conducted using the SpectraQuest Machinery Fault Simulator. This modular package allows one to simulate faults on a variety of industrial equipment such as motors, compressors, journal bearings and centrifugal pumps.

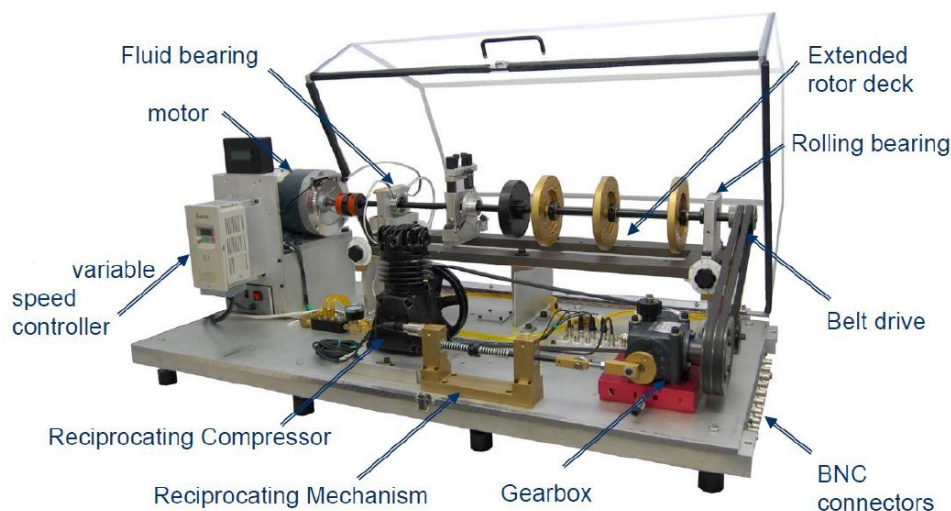


Figure 4-1: The SpectraQuest Machine Fault Simulator used for testing [94].

Interfacing with the simulator is the drive control and electrical fault simulation panel. This panel (Figure 4-2) allows for the selection and execution of the following functions:

- Supply selection (Grid or Inverter)
- Motor Start/ Stop/ Emergency Stop
- Load Selection – No load/ Resistive Load/ Servo Load
- Servo Start/ Stop and Control
- Servo motor Human Machine Interface
- Fault Selection – Inter-turn fault/ Phase loss/ Voltage unbalance



Figure 4-2: Drive Control and Fault Simulation interface panel.

A conceptual representation of the test setup is presented below in Figure 4-3, whilst detailed schematics of the panel can be found in Appendix A.

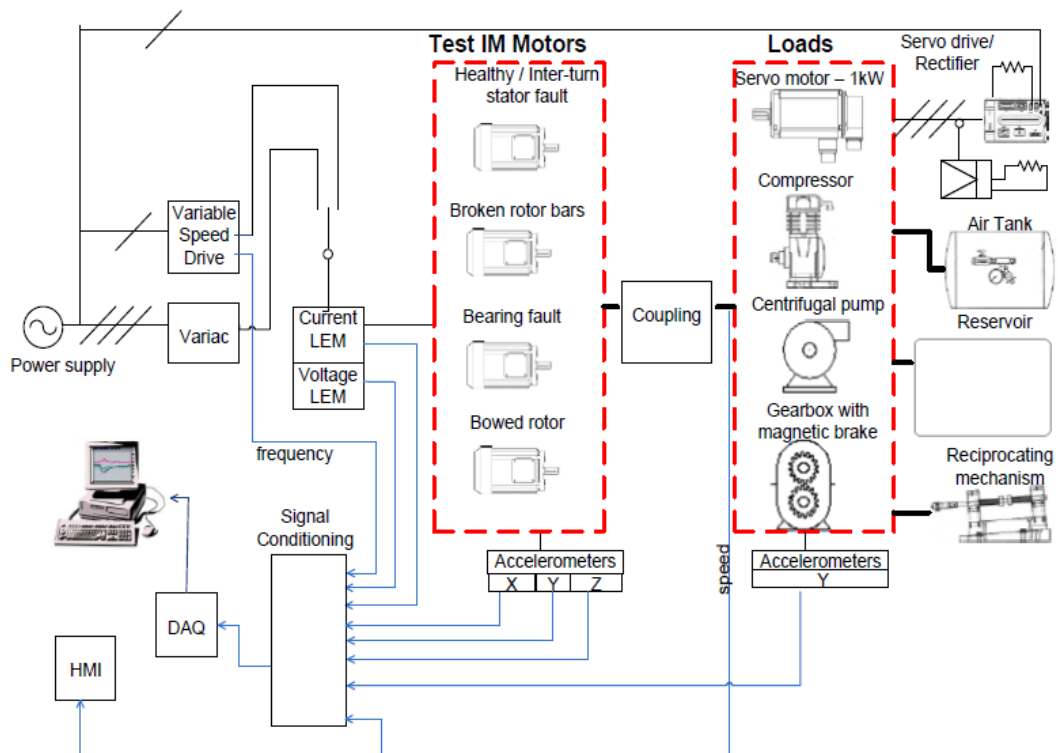


Figure 4-3: A conceptual overview of the test rig used for testing [94].

4.2.1 Instrumentation and Data Acquisition

Analog to Digital Converter

Data acquisition was performed using the National Instruments CompactDAQ system. This portable system allows for the connection of modular I/O such as the NI 9215 Differential Analog Input Module. This module contains four differential inputs with a range of $\pm 10V$ and is able to simultaneously capture 100 000 samples per second at 16-Bit resolution [95]. A conceptual diagram of the input module is presented below:

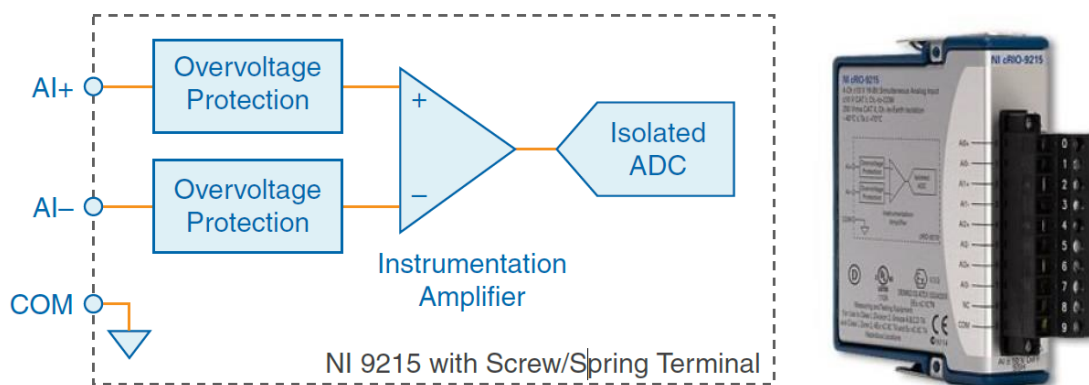


Figure 4-4: NI9215 Analog input module concept [95].

The CompactDAQ connects directly to a PC via USB interface. LabView was used as the software tool to record and visualize the data. Configuration of the three NI9215 modules was also performed via the LabView interface. The following inputs were measured using the system:

- Phase A voltage - v_{ab}
- Phase B voltage - v_{bc}
- Phase C voltage - v_{ac}
- Line current A - i_a
- Line current B - i_b
- Line current C - i_c
- Shaft torque - T
- Shaft speed - n
- Inverter frequency - f_{inv}

The system was setup to record for 30 seconds at a sampling rate of 25 600 samples per second, thus resulting in 768 000 data points per channel. The LabView virtual instrument block diagram used to configure all the signals and ranges can be viewed in Appendix A.

Voltage and Current Measurements

The 3 phase voltage supplied to the motor was measured using LEM LV25-P Hall effect voltage transducers mounted in the drive interface panel. Similarly, the line currents were measured using LEM LA25-NP Hall effect current transducers. The outputs of the transducers are biased to a $\pm 10V$ range and fed into an anti-aliasing low pass filter circuits with a cut-off frequency of 12 kHz. These voltage inputs were then calibrated and linearized in using the LabView DAQ assistant function to obtain the measurements in units of Volts and Amperes.

Speed and Torque Measurements

The induction motor speed was measured using the 20-bit rotary incremental shaft encoder of the coupled servo motor drive. Using the servo drive configuration software, the encoder was set to output the maximum of 128 000 pulses per revolution, thus providing the highest resolution to enable the capturing of speed transients. The speed signal was made available to the data acquisition system by setting up a 0 – 8V analog output from the servo drive.

Shaft torque was measured directly using the Lorenz DR-2112 Torque transducer. The 0 – 10V output from the transducer was wired directly to the analog input module of the data acquisition system, where the voltage is converted to engineering units using the DAQ assistant. The measured shaft torque was used as the reference for motor loading.

4.2.2 Data Processing

The stored motor data was processed using MATLAB R2015a. Programs were coded to import the data and apply the signal processing techniques detailed in section 3.4 to the

stator current, instantaneous power and squared current data. The MATLAB code produced for this study can be found in Appendix A.

4.2.3 Test Motors

The SpectraQuest test rig is supplied with several intentionally faulted induction motors. All the motors are 3 phase, Class B and have identical ratings as detailed in the following table:

Table 4-1: Specifications of the Induction motor used for testing [96].

Induction Motor Specifications	
Rated Power (W)	250
Voltage (V)	190
Frequency (Hz)	50
Number of poles	2
Full load current (A)	1.85
No load current (A)	0.7
Full load torque (Nm)	1.03
Locked rotor torque (Nm)	4.06
Insulation Class	F3
Time rating	Continuous

The faulted motors used in this study are as follows:

Motor with broken rotor bars

The motor used to simulate the broken rotor bar condition has 3 intentionally broken rotor bars of a total of 34.

Motor with faulty bearings

The motor used to simulate the faulted bearing condition contains an NSK 6203 ball bearing with 8 balls. The bearing is preinstalled in the motor with an inner and outer raceway defect.

Motor with inter-turn fault

The motor used to simulate the stator inter-turn fault has two windings that are tapped and brought out to a control box on the outside of the motor. Depending on the combination of connections, 2 or 4 turns can be shorted via an external variable resistance housed in the drive interface panel depicted in Figure 4-2. A high resistance simulates a healthy condition and a low resistance simulates a faulted condition for both fault levels. Hence, this motor is also used as the healthy motor for baseline comparisons.

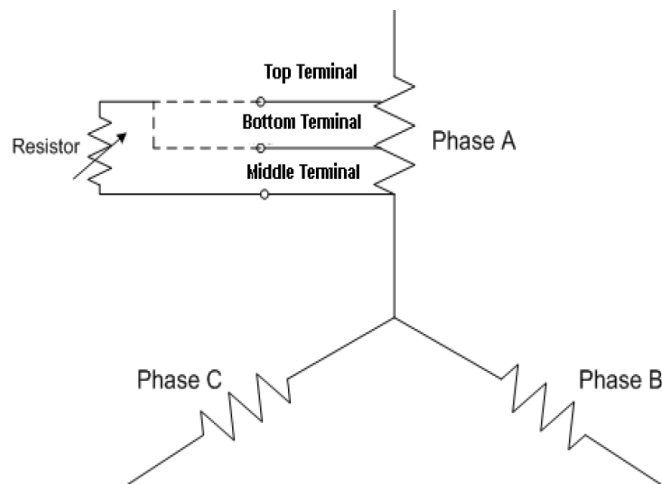


Figure 4-5: Diagram depicting terminal arrangement for simulating a stator fault [94].

When simulating the stator inter-turn faults, the fault control resistor was set to 10Ω to ensure that fault currents do not cause permanent damage to the stator windings. The fault current and fault voltage for each fault level is tabulated below:

Table 4-2: Table of fault voltage and current versus fault severity.

Shorted turns	Fault Resistance [Ω]	Fault Voltage [V]	Fault Current [A]
2	10	10.8	1.1 – 1.2
4	10	20.35	2.5 – 2.6

4.2.4 Motor Supplies and Loads

Grid versus Inverter supply

The drive interface control panel allows for the selection between grid supply and inverter supply for the induction motor. The supplies are first connected to an earth leakage and an isolator, where after the grid supply is connected to an autotransformer (Variac) or the inverter drive.

The inverter drive supplied with the test rig is the Lenze SMVector. The drive is configured and used in the constant-volts-per hertz operating mode as explained in section 2.2.4. A list of the critical parameters configured for the drive can be found in Appendix A.

Resistive Load versus Servo Load

The induction motor was loaded in two ways during testing; both involved the operation of the servo machine and servo drive. A resistance controlled variable load was presented to the induction motor by rectifying the outputs of the coupled servo machine and dissipating the dc current through the variable resistor mounted on the drive interface control panel. This open loop configuration can be seen in the schematics found in Appendix A, sheet [3](#).

The second method of loading the induction machine involves running the servo machine in closed loop control. The drive is selected to control the torque via the servo system’s HMI, where a negative torque can be precisely selected to load the induction motor. The energy generated by the servo machine is dissipated in the drive by raising its bus voltage, or through an external 1kW regenerative resistor if need be [97]. The list of servo system parameters as set during testing can be found in Appendix A.

The motor was loaded to three levels during the various tests as shown in the table below:

Table 4-3: Percentage loading and the corresponding shaft torque versus current dissipated.

Load [%]	Torque [Nm]	Resistor Current [A]
0	0	0
50	0.54	1.21
100	1.03	2.57

Table 4-3 maps the rated torque at rated voltage to the current dissipated in the resistor via the servo machine in open loop control. When the servo machine is operated in closed loop control, the required negative torque is input directly into the Servo Drive via the HMI.

4.3 Experimental Methodology

4.3.1 Baseline Conditions

Mechanical Alignment

The SpectraQuest test rig and motors have keyed alignment slots to allow motors to be changed out quickly. Nonetheless, whenever motors were changed, the alignment was checked using the reverse clock gauge method.

Motor warm-up

Before any tests were conducted, the motor was operated at full load for a period of 15 minutes to allow the motor and drive components to reach thermal stability.

Laboratory Electrical Supply

The laboratory supply connected to the drive control interface panel was checked for balance and total harmonic distortion. Individual phases were adjusted using a three phase Variac to supply rated voltage to the motor. The Total Harmonic Distortion for the incoming supply was calculated to be less than 1%, which is acceptable according to IEC STD 519-2014. A detailed schematic of the motor supply and drive controls can be found in Appendix A.

4.3.2 Experimental Procedure

Fault Simulation Procedure

During the experiments to simulate and detect the motor faults, the following testing procedure was adhered to:

1. Ensure that the main electrical supply is disconnected, and then proceed to install the desired test motor.
2. Torque all mounting bolts to the required torque setting and check the shaft alignment using the clock gauge.
3. Reconnect the motor electrical supply and de-isolate the main supply.
4. Select the motor to Grid or Inverter supply.
5. Select the required loading type, namely, No Load, Resistive Load or Servo Load.
6. Select the required load level using the variable resistor or the Servo Drive HMI.
7. Start the induction motor and the servo machine if necessary, and allow at least 15 minutes to heat soak.
8. With LabView running the Instrument Block Diagram, start a recording and save the data when prompted. Check the plausibility of the data on the graphs as well as in the text file.
9. If the previous data set is plausible, initiate another recording and save the data to the PC hard drive.
10. Repeat the procedure sequentially as needed when varying the load or selecting a different supply.

Fault Detection Procedure

The fault detection procedure is based on inputting valid, plausible data into the MATLAB data processing programs. The programs were constructed to execute the following sequence of functions:

1. Import the valid data for the healthy and faulty motor.
2. Define critical parameters such as sampling frequency, number of samples, time and frequency vectors.
3. Apply the Window Function to the current and/or voltage data.
4. Zero pad the windowed data to the next power of two for smoother FFT output.
5. Apply the FFT function to the data and create a single sided spectrum.
6. Calculate the Power Spectral Density and normalize the output.

7. Plot the voltage, current and PSD for the healthy versus faulty motor.
8. Calculate the standard deviation of the speed measurement and hence slip.
9. Calculate the expected fault component frequencies for the healthy and faulty motors.
10. Analyze the spectra in the vicinity of the calculated frequencies (including the deviation) and identify the fault related peaks.
11. Record the amplitude difference between the healthy and faulty components.
(Convention: Amplitude difference = Healthy Amplitude – Faulty Amplitude)
12. Repeat this process for different supply types, loads and fault conditions.

4.4 Concluding Remarks

In this chapter the hardware and software used to conduct the experiments on the healthy and faulty motors were presented. The essential features of the software, hardware and instrumentation were described. The experimental procedure followed for capturing and analysing the motor data was also discussed.

5 Results and Discussion

5.1 Introduction

In this chapter the results obtained by following the experimental methodology and applying the theoretical concepts will be presented. The chapter is structured to cover the three faults and the application of the three analysis methods to each fault. The results will be analysed and discussed with a view of the efficacy of each technique in detecting the given fault.

By following the experimental methodology, the three fault types, namely, stator inter-turn fault, broken rotor bar fault and bearing race faults were implemented with the respective motor in steady state. The fault detection procedure was implemented using the compiled MATLAB programs for each fault type and analysis technique. The results obtained are now presented.

5.2 Stator fault tests using Motor Current Signature Analysis

Firstly, tests were conducted on the healthy motor, to serve as baseline recordings of all motor variables in accordance with the testing procedure. Recordings were taken for grid and inverter-fed conditions, at varying loads in accordance with the values in Table 4-3.

5.2.1 MCSA: Inter-turn fault – 4 shorted turns

As per procedure, the stator fault condition was implemented by shorting out 4 turns and allowing a fault current of approximately 2.5A to flow through the fault resistor. This test was conducted at 0%, 50% and 100% load with the motor connected to the grid. Using equation (3.6), the expected fault frequencies were calculated for various combinations of n and k . The standard deviation associated with the measured speed and hence frequency was calculated to be 0.07Hz. This provided the area of interest around which the fault component was sought. While processing the data, the combination $n = 1$ and $k = 1, 3, 5$ consistently produced the strongest peaks at the expected fault frequencies. The spectra for the motor with 4 shorted turns at full load, for the chosen combinations of n and k , are presented below:

PSD of Motor Line Current

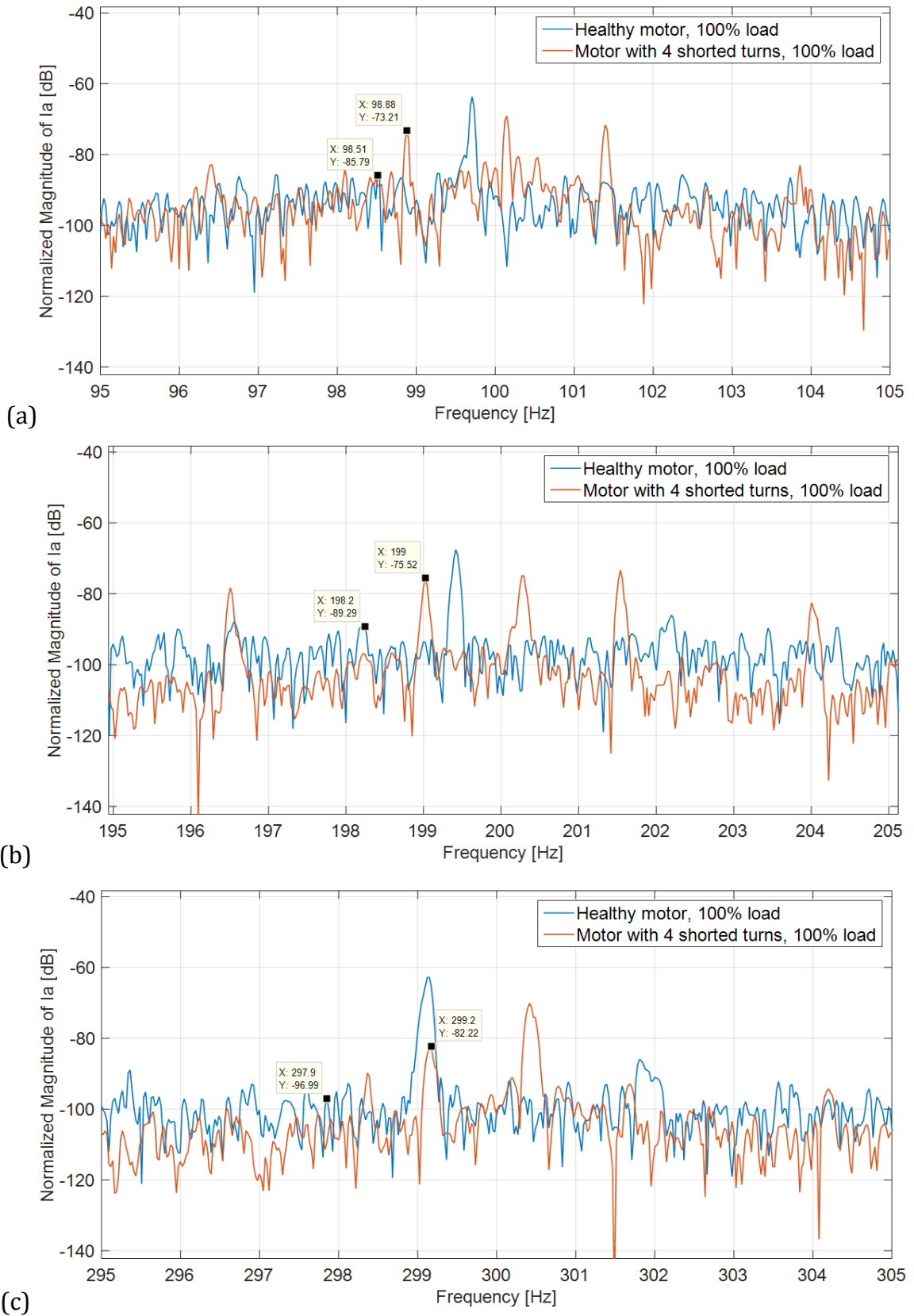


Figure 5-1: PSD of the motor current at full load for selected n and k values (a) $n=1, k=1$; (b) $n=1, k=3$; (c) $n=1, k=5$;

Table 5-1: Table of results for the motor at full load with 4 shorted turns using MCSA.

Load = 100%	Healthy Motor		Motor with 4 shorted turns		Result
n; k	Frequency [Hz]	Amplitude [dB]	Frequency [Hz]	Amplitude [dB]	Amplitude difference [dB]
1; 1	98.51	-85.79	98.88	-73.21	-12.58
1; 3	198.2	-89.29	199.0	-75.52	-13.77
1; 5	297.9	-96.99	299.2	-82.22	-14.77

From Figure 5-1, it can be seen that the inter-turn fault can be detected clearly in all three instances, with the calculated fault frequencies typically matching with the actual frequencies to within 0.02Hz. The amplitude difference between the healthy and faulty motor varied between -12dB and -14dB. In the second case (n=1; k=3) the fault component is approximately 23 times larger in amplitude than the healthy component, in absolute terms. The variation in the frequency between the healthy motor components and the faulty motor components can be attributed to the difference in grid frequency between the two sets of data. Depending on the time of day, the grid frequency typically varies between 49.85Hz and 50.15Hz. In this instance, the fundamental frequency for the healthy and faulty case was 49.85Hz and 50.07Hz respectively.

When the author examined the results for all stator related faults, the combination of n=1; k=3 produced the most consistent results. Thus, henceforth this combination of n and k will be presented for the rest of the results. The results for the other combinations of n and k can be found in Appendix B.

5.2.2 MCSA: Inter-turn fault with load variation – 4 shorted turns

With 4 shorted turns, the motor was also tested at different load levels in accordance with the values in Table 4-3, using the resistive load. The results of these tests are summarized in the table below:

Table 5-2: Table of fault components (n=1; k=3) and amplitudes for a motor with 4 shorted turns at various load levels using MCSA.

Load [%]	Healthy Motor		Motor with 4 shorted turns		Result
	Frequency [Hz]	Amplitude [dB]	Frequency [Hz]	Amplitude [dB]	Amplitude difference [dB]
0	199.9	-97.16	199.9	-75.77	-21.39
50	199.1	-92.53	200.0	-73.56	-18.97
100	198.2	-89.29	199.0	-75.52	-13.77

The spectra associated with the results above for 0% and 50% load are presented below:

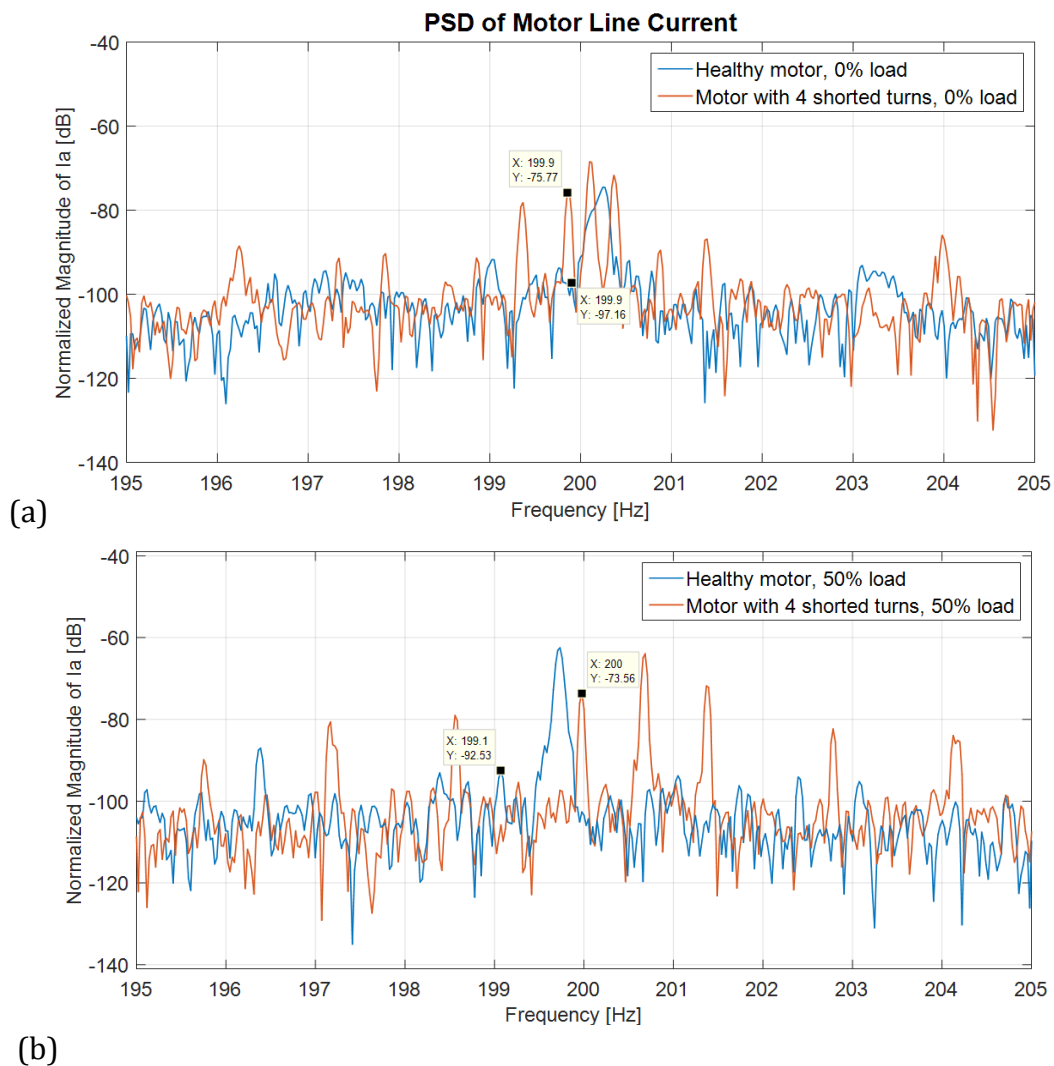


Figure 5-2: Current Spectra of a motor with 4 shorted turns at (a) 0% and (b) 50% load showing fault components.

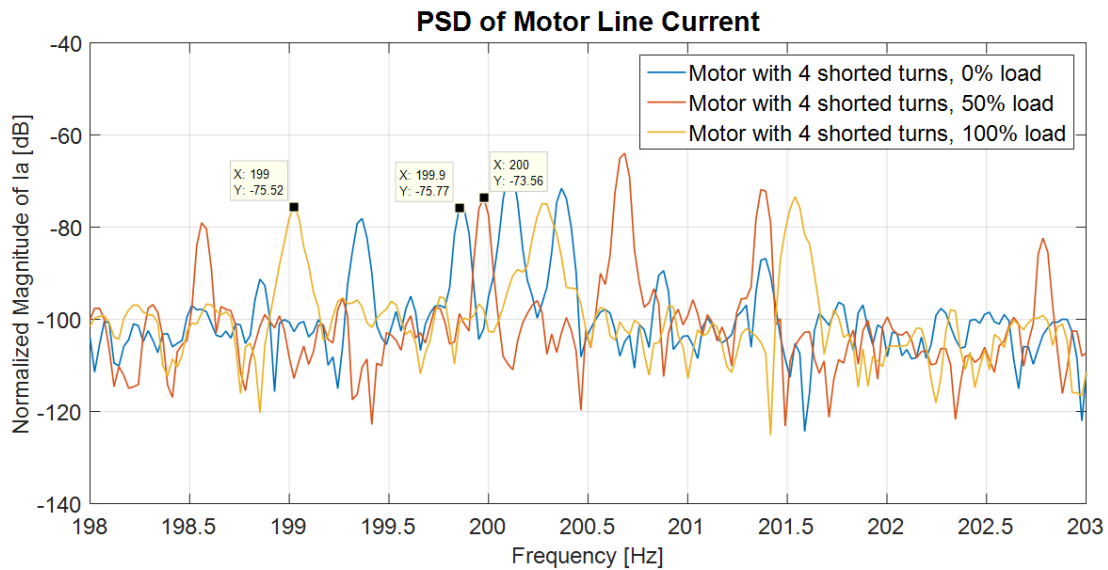


Figure 5-3: Current spectrum of motor with an inter-turn fault at various loads.

From examination of the data in Table 5-2 and the associated spectra, the amplitude of the fault component remains almost constant at approximately -75dB despite the variation in load. This can clearly be seen in Figure 5-3. When examining the healthy motor's results, the associated component seems to be load sensitive and increases with load. This results in the fault level (difference) increasing as load the decreases, ranging from -13.77dB at full load to -21.39dB at no load.

The slip dependence of the stator fault component can also be observed in Figure5-3 by the movement of the component to a reduced frequency as the load increases. The components at no-load and 50% load are swapped in this instance due to the difference in the fundamental grid frequency between the two data sets, (50.02Hz and 50.17Hz respectively). Thus in summary, the fault components were successfully detected in steady state when 4 turns were shorted and when the load torque was varied from no load to full load.

5.2.3 MCSA: Reduction in fault severity – 2 shorted turns

By changing the connections to the motor, two turns were shorted, thereby reducing the fault severity. With two turns shorted a fault current of approximately 1.2A flows through the control resistor. The following spectrum was obtained with the motor at full load as shown in Figure 5-4.

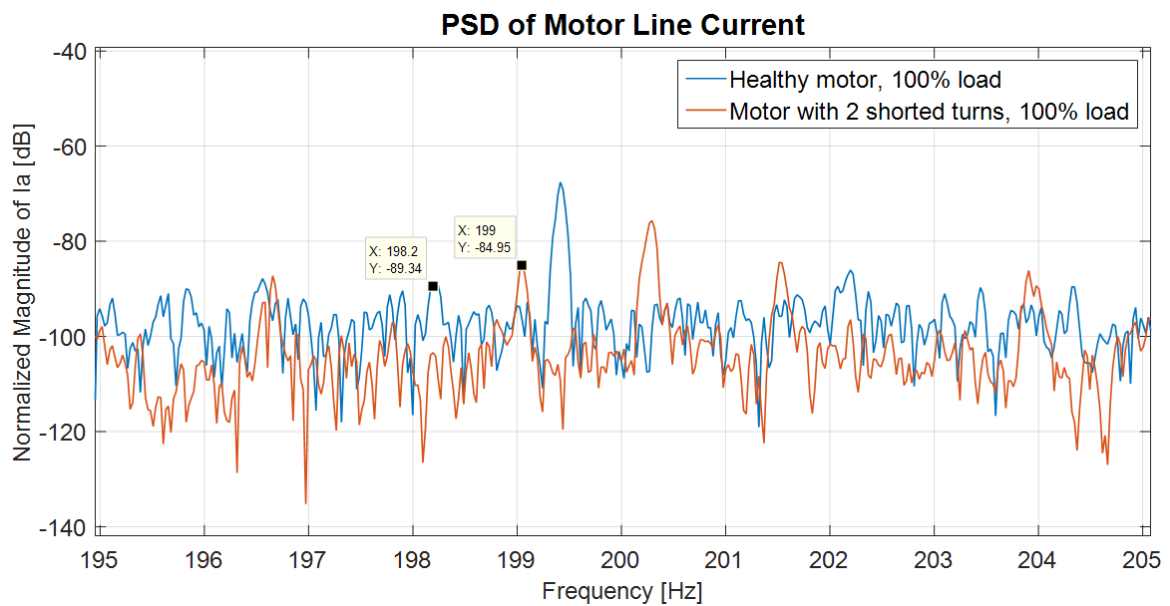


Figure 5-4: Current spectrum of motor with 2 shorted turn at 100% load.

From the spectrum it is clear that the fault component amplitude has decreased significantly from -75.52 dB to -84.95dB by reducing the number of shorted turns from 4 to 2. The difference in amplitude between the healthy and faulty motor was also reduced from -13.77dB to -4.39dB. This represents a significant decrease in real terms and shows that the method is sensitive to changes in fault severity.

5.2.4 MCSA: Inter-turn fault with load variation – 2 shorted turns

With 2 turns shorted, the load was varied from full load to no-load. The following results and spectrum were obtained:

Table 5-3: Table of fault components (n=1; k=3) and amplitudes for motor with 2 shorted turns at various loads.

Load [%]	Healthy Motor		Motor with 2 shorted turns		Result
	Frequency [Hz]	Amplitude [dB]	Frequency [Hz]	Amplitude [dB]	Amplitude difference [dB]
0	200.0	-93.72	199.9	-89.18	-4.54
50	199.1	-92.53	199.5	-85.89	-6.64
100	198.2	-89.34	199.0	-84.95	-4.39

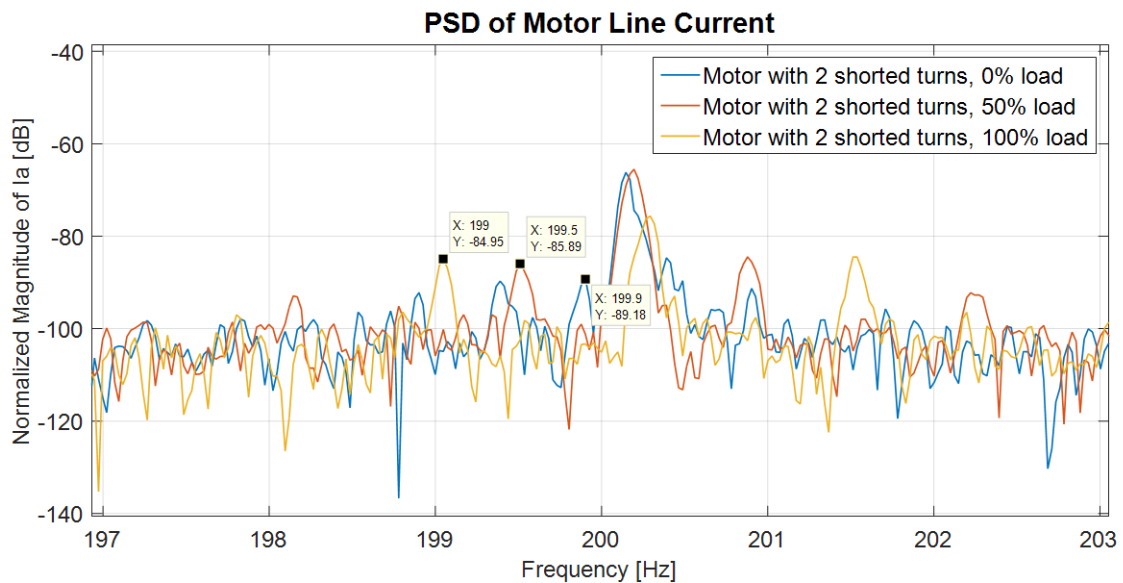


Figure 5-5: Current spectrum of faulty motor with 2 shorted turns at various loads.

With 2 turns shorted, the fault component amplitudes are reduced because of the reduced fault current, across all load conditions. The results show more variance in amplitude than with 4 shorted turns, but seem to suggest that the fault level is relatively independent of load. The fault component frequencies' dependence on slip can also clearly be seen in this instance. In summary, with reduced fault severity, the inter-turn fault could still be detected at all tested loads, even though the difference in amplitude between healthy and faulty motors is significantly reduced.

5.2.5 MCSA: Inverter connected motor with inter-turn fault

The faulted motor was connected to the inverter drive and ramped up to the 50Hz fundamental frequency. With 4 shorted turns, the motor was operated at various loads and the captured data processed and compared to the healthy inverter driven motor. With the motor at 100% load, the spectra shown in Figure 5-6 were obtained:

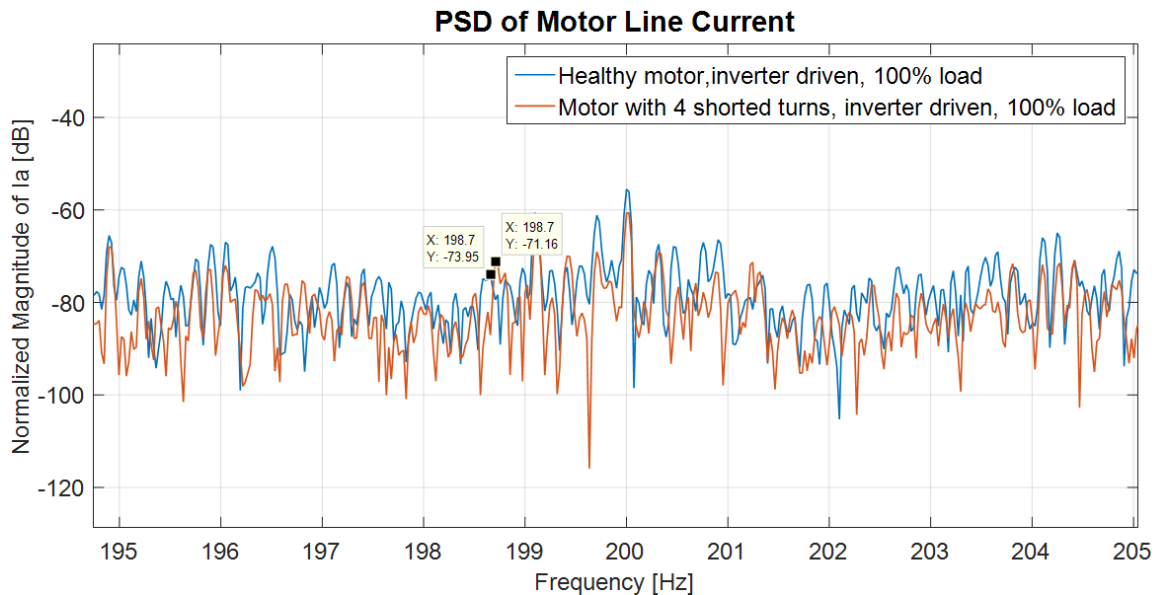


Figure 5-6: Current spectrum of an inverter driven motor with 4 shorted turns versus a healthy motor at full load.

At the calculated fault frequency of 198.7Hz, the fault component had an amplitude of -71.16dB while the equivalent healthy component had an amplitude of -73.95dB. Despite an amplitude difference of -2.79dB the signals are very close to the noise floor. Hence the result has increased uncertainty and inspires low confidence. Similarly, poor results were obtained for all load levels and reduced fault severity, with the faults components often deeply embedded in the noise floor. These results are available in Appendix B. The increased noise can be attributed to the increased harmonics from the switching action of the inverter [94].

5.3 Stator fault detection using Motor Square Current Signature Analysis

The PSD's of the squared current were then attained for the data sets used in the previous section. Equations (3.7) and (3.8) were used to calculate the expected fault component frequencies. The results were recorded for various values of n and k . In this case, the combination of $n = 1$ and $k = 5$ produced the most consistent results. Detailed results for all test combinations can be found in Appendix B, however, the more significant findings are discussed below.

5.3.1 MSCSA: Inter-turn fault - 4 shorted turns

The fault frequency equations when using the square of the current take on a different form to those of the classical current method, thus providing two unique frequencies to evaluate. The results and spectrum for the motor at full load with 4 turns shorted are presented below:

Table 5-4: Squared Current PSD results for motor with 4 shorted turns at full load.

Load = 100% n=1; k=5	Healthy Motor		Faulty Motor 4 shorted turns		Result
	Frequency [Hz]	Amplitude [dB]	Frequency [Hz]	Amplitude [dB]	Amplitude diff. [dB]
$f_{st1} = 2kf_1$	498.60	-17.88	500.70	-13.69	-4.19
$f_{st2} = 2f_1 \left[\frac{n}{p}(1-s) + k \right]$	595.90	-49.31	598.33	-54.26	4.95

From the table above it is evident that only the first fault component produced a valid result of -4.19dB. This represents a significant change in amplitude between the healthy and unhealthy motor. The first fault component frequency bears the advantage that it is significantly higher than the noise floor (Figure 5-7). The shift between the two peaks is again due to the difference in grid frequency between the two data sets (49.85Hz and 50.07Hz respectively). The second component produced inconclusive results with the healthy component amplitude exceeding the fault component amplitude. The spectrum showing the first fault component is shown overleaf:

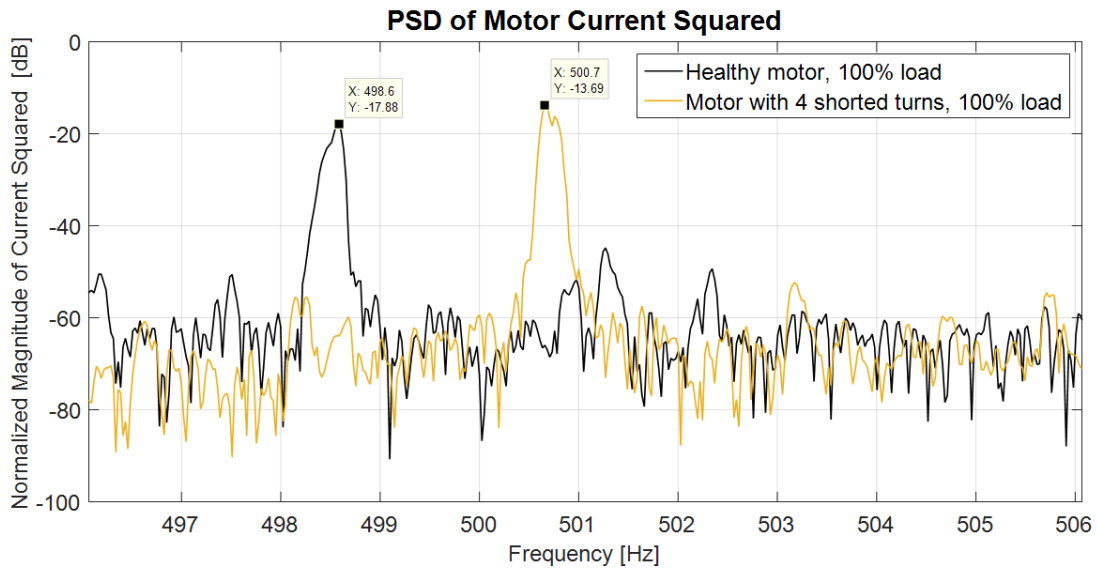


Figure 5-7: Spectrum of the squared current for the first fault component at full load.

5.3.2 MSCSA: Inter-turn fault with load variation – 4 shorted turns

When varying the load with 4 turns shorted, the following results were obtained at the calculated frequencies:

Table 5-5: Table of fault component frequencies ($n=1; k=5$) and amplitudes from the squared current spectra for a motor with 4 shorted turns at various loads.

$n=1; k=5$	Healthy Motor		Faulty Motor 4 shorted turns		Result
	Frequency [Hz]	Amplitude [dB]	Frequency [Hz]	Amplitude [dB]	Amplitude diff. [dB]
Load = 0%					
$f_{st1} = 2kf_1$	500.70	-25.61	500.30	-18.29	-7.32
$f_{st2} = 2f_1 \left[\frac{n}{p}(1-s) + k \right]$	600.10	-46.61	599.90	-41.51	-5.10
Load = 50%					
$f_{st1} = 2kf_1$	499.30	-17.68	501.70	-12.25	-5.43
$f_{st2} = 2f_1 \left[\frac{n}{p}(1-s) + k \right]$	597.82	-47.03	600.63	-48.16	1.13
Load = 100%					
$f_{st1} = 2kf_1$	498.60	-17.88	500.70	-13.69	-4.19
$f_{st2} = 2f_1 \left[\frac{n}{p}(1-s) + k \right]$	595.90	-49.31	598.33	-54.26	4.95

The first fault component f_{st1} consistently produced results indicative of the fault across all tested loads. The amplitude difference between the healthy and faulty components were strongest at no-load (-7.32dB) and decreased with increasing load to -4.19dB at full load. The second fault component f_{st2} only produced a valid result at no-load (-5.1dB), whilst producing inconclusive results at 50% load and full load.

5.3.3 MSCSA: Reduction in fault severity – 2 shorted turns

The data for the inter-turn fault at reduced severity was then processed using the squared current algorithm. This was also done for the motor at various loads. The table of results is presented below for discussion:

Table 5-6: Table of fault component frequencies (n=1; k=5) and amplitudes from the squared current spectra for a motor with 2 shorted turns at various loads.

n=1; k=5	Healthy Motor		Faulty Motor 2 shorted turns		Result
	Frequency [Hz]	Amplitude [dB]	Frequency [Hz]	Amplitude [dB]	Amplitude diff. [dB]
Load = 0%					
$f_{st1} = 2kf_1$	500.70	-25.61	500.40	-21.66	-3.95
$f_{st2} = 2f_1 \left[\frac{n}{p}(1-s) + k \right]$	600.10	-29.31	600.09	-50.05	6.28
Load = 50%					
$f_{st1} = 2kf_1$	499.30	-17.78	500.60	-21.54	3.76
$f_{st2} = 2f_1 \left[\frac{n}{p}(1-s) + k \right]$	597.82	-47.03	599.30	-52.09	5.06
Load =100%					
$f_{st1} = 2kf_1$	498.60	-17.88	500.70	-19.76	1.88
$f_{st2} = 2f_1 \left[\frac{n}{p}(1-s) + k \right]$	595.90	-49.31	598.40	-53.44	4.13

At reduced fault severity, the square current technique generally produced poor results. A valid result indicative of the shorted turns was only produced at no-load when examining the amplitudes associated with first fault component. At no-load, the fault level reduced from -7.32dB to -3.95dB when the fault severity was reduced from 4 to 2 shorted turns. The second fault component f_{st2} produced inconclusive results at all loads with reduced fault severity.

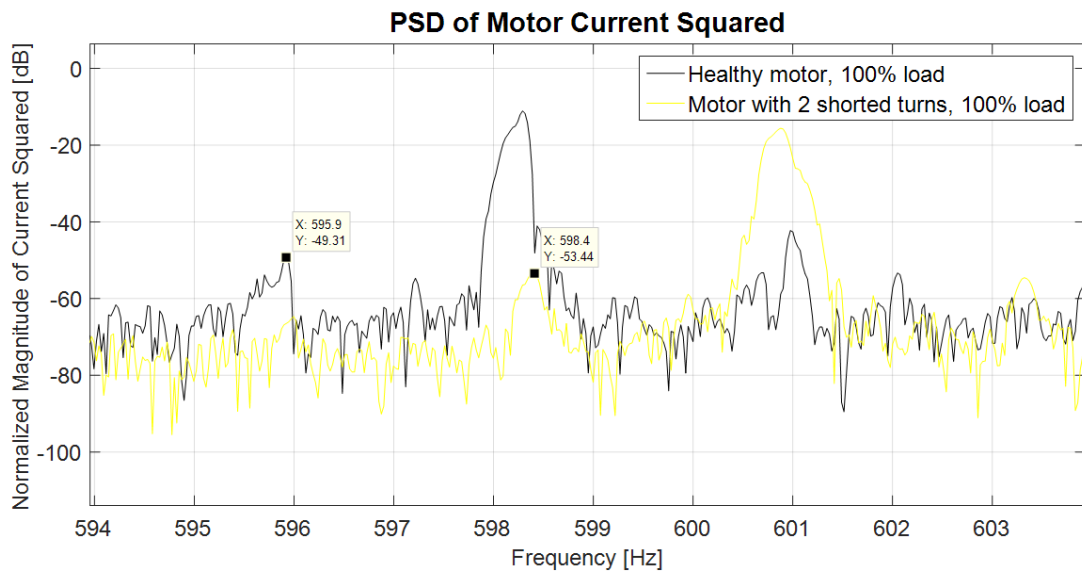


Figure 5-8: Spectrum of the squared current for the second fault component at full load.

5.3.4 MSCSA - Inverter connected motor with inter-turn fault

For the inverter driven motor at various loads with an inter-turn fault, frequencies of interest were analysed for various combinations of n and k (Appendix B), none of which produced conclusive results. This result was largely expected since the square current technique already fared relatively poorly in the grid connected case. The results suggest that the basic technique is not reliable for inverter driven induction motor applications.

5.4 Stator fault detection using Instantaneous Power Signature Analysis

The PSD's of the partial instantaneous power were then attained for the data sets used in the previous sections. Equations (3.7) and (3.8) were used to calculate the expected fault component frequencies. The findings for the combination of $n = 1$ and $k = 5$ are discussed below.

5.4.1 IPSA: Inter-turn fault – 4 shorted turns

From Table 5-7 below, the first fault component frequency f_{st1} produced results indicative of the stator fault. The resultant amplitude differences are generally smaller in magnitude than those obtained from analyzing the square current spectra and show no clear trend with motor loading.

Table 5-7: Table of fault component frequencies (n=1; k=5) and amplitudes from the instantaneous power PSD's for a motor with 4 shorted turns at various loads.

n=1; k=5	Healthy Motor		Faulty Motor 4 shorted turns		Result
	Frequency [Hz]	Amplitude [dB]	Frequency [Hz]	Amplitude [dB]	Amplitude diff. [dB]
Load = 0%					
$f_{st1} = \frac{n}{p}(1-s)f_1$	500.70	-26.08	500.30	-21.58	-4.50
$f_{st2} = f_1 \left[\frac{n}{p}(1-s) + 2k \right]$	600.10	-51.07	599.90	-45.58	-5.49
Load = 50%					
$f_{st1} = \frac{n}{p}(1-s)f_1$	499.30	-19.51	501.70	-14.34	-5.17
$f_{st2} = f_1 \left[\frac{n}{p}(1-s) + 2k \right]$	597.82	-67.60	600.63	-59.84	-7.76
Load = 100%					
$f_{st1} = \frac{n}{p}(1-s)f_1$	498.60	-19.77	500.70	-17.19	-2.58
$f_{st2} = f_1 \left[\frac{n}{p}(1-s) + 2k \right]$	595.90	-60.20	598.33	-58.13	-2.07

As expected, the instantaneous power and square current spectra were very similar (Figure 5-9) with the first fault f_{st1} components showing similar patterns and results. In section 3.3.2, the inference was made that equation (3.8) for the second fault component frequency f_{st2} should be applicable to the instantaneous power spectrum. To this end, the second fault

component frequency f_{st2} produced significant amplitude changes across all tested loads, in contrast to the results using the square of the current, where a valid result was only obtained at no-load. Due to the results only agreeing at no-load, no firm conclusions can be drawn as to the direct applicability of the equation (3.8) to the instantaneous power spectrum. Further investigation would be required to eliminate any other disturbances or sources of error to reconcile the difference between the results.

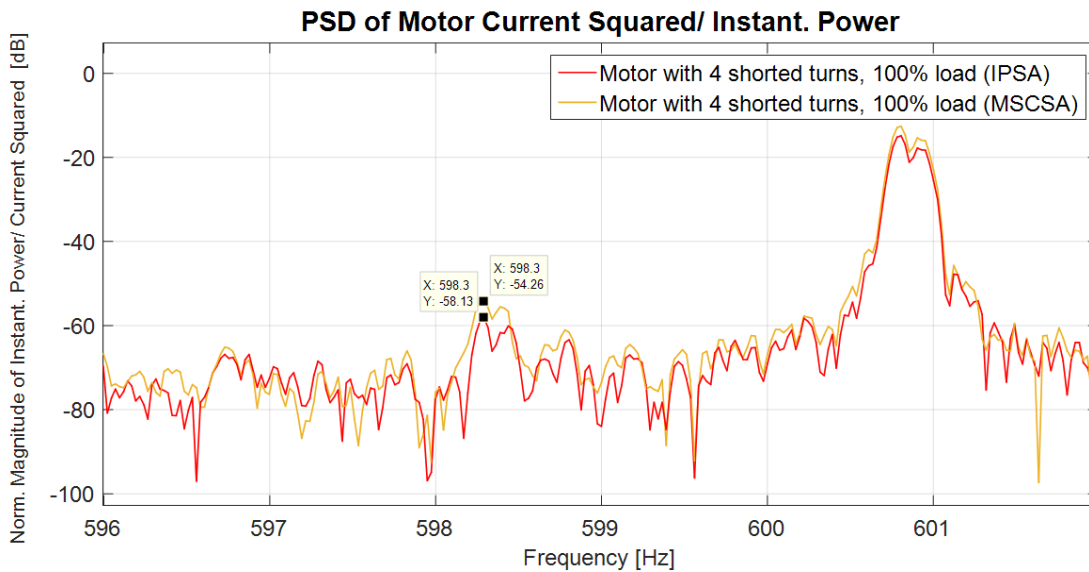


Figure 5-9: Comparison of instantaneous power and squared current spectra showing fault component f_{st2} at full load.

5.4.2 IPSA: Reduction in fault severity – 2 shorted turns

When reducing the fault severity by only shorting out 2 turns, the IPSA technique similarly produced poor results. The reduced fault component amplitudes coupled with the generally noisy spectrum only produced a result indicative of the fault at no-load using the first fault component equation f_{st1} . The resultant amplitude difference of -2.19dB is approximately half that of the result when 4 turns were shorted at no-load (-4.5dB). The table of results is presented overleaf.

Table 5-8: Table of fault components frequencies (n=1; k=5) and amplitudes from the instantaneous power PSD's for a motor with 2 shorted turns at various loads.

n=1; k=5	Healthy Motor		Faulty Motor 2 shorted turns		Result
	Frequency [Hz]	Amplitude [dB]	Frequency [Hz]	Amplitude [dB]	Amplitude diff. [dB]
Load = 0%					
$f_{st1} = \frac{n}{p}(1-s)f_1$	500.70	-26.08	500.40	-23.89	-2.19
$f_{st2} = f_1 \left[\frac{n}{p}(1-s) + 2k \right]$	600.10	-35.59	600.09	-51.74	16.15
Load = 50%					
$f_{st1} = \frac{n}{p}(1-s)f_1$	499.30	-19.51	500.60	-23.05	3.54
$f_{st2} = f_1 \left[\frac{n}{p}(1-s) + 2k \right]$	597.82	-67.60	599.40	-66.01	-1.59
Load =100%					
$f_{st1} = \frac{n}{p}(1-s)f_1$	498.60	-19.77	500.70	-19.76	-0.01
$f_{st2} = f_1 \left[\frac{n}{p}(1-s) + 2k \right]$	595.90	-60.20	598.40	-61.18	0.98

5.4.3 IPSA: Inverter connected motor with inter-turn fault

Using the set of inverter driven motor data with the inter-turn fault, spectra of the instantaneous power were produced. As expected, the spectra were affected by the switching noise of the inverter, especially since the voltage is included in the calculation. Hence, no valid results were obtained when examining the spectra at the calculated fault frequencies at all loads and fault severities.

5.4.4 Summary of stator inter-turn fault detection

In this section inter-turn faults were simulated and the data processed using the three different techniques. Using MCSA, the inter-turn faults could be detected at all loads and at reduced severity, except for the case of the inverter driven motor, where the technique provided a marginal result in one case only (maximum severity and full load).

MSCSA and IPSA provided two unique fault frequencies to investigate. The first fault component frequency, which is effectively a harmonic of twice the line frequency, was the only component to produce consistent results using both methods. The two techniques produced similar spectra, and fault features were identified using the first fault component at full fault severity across all tested loads. At reduced fault severity and when the motor was inverter driven, the techniques proved inadequate at detecting the inter-turn faults. The applicability of equation (3.8) to the IPSA technique could not be ascertained from the results.

5.5 Broken Rotor Bar Fault Detection using Motor Current Signature Analysis

Following the stator fault tests, the test motor was changed to one with three broken rotor bars. Tests were conducted as per the procedure described in section 4.3.2. The recorded data for the healthy and faulty motor were processed using MCSA algorithm in MATLAB. The resultant spectra were checked against the anticipated fault frequencies calculated from equation (3.10) for $k = 1, 2$ and 3 . The associated amplitudes for the healthy and faulty components were then recorded at the actual fault frequencies. For the sake of brevity, only the results for $k = 1$ are discussed in this section since this is the most commonly analysed component in the literature. Detailed results for the other components can be found in Appendix B.

5.5.1 MCSA: Broken Rotor Bars at 100% load

With the faulty motor at full load in steady state operation, the following current spectrum was obtained when the data was processed and compared to the healthy motor:

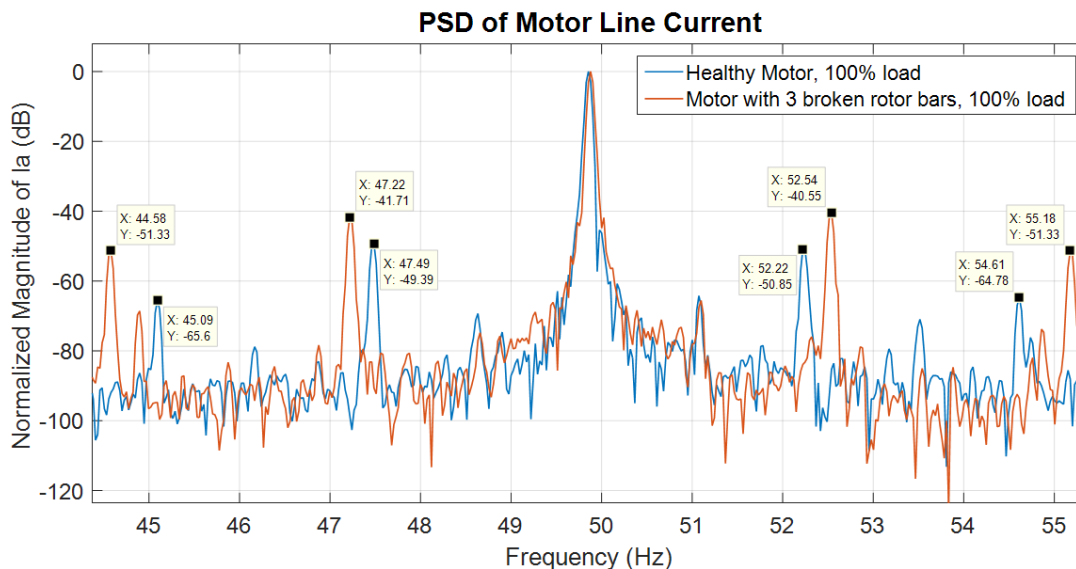


Figure 5-10: PSD of motor current showing broken rotor bar upper and lower sideband components.

From the spectrum above, the upper and lower sideband components about the fundamental can be observed. For $k = 1$, the amplitude of the lower sideband components associated with healthy and unhealthy motor were -49.39dB and -41.71dB respectively.

Hence, the lower sideband component changed by -7.68dB due to the presence of the broken rotor bars. Similarly, the first upper sideband component ($k = 1$) resulted in an amplitude difference of -10.3dB between the healthy and unhealthy case. The associated frequencies and amplitudes for the motor at full load are listed in the table below:

Table 5-9: Fault component frequencies and amplitudes associated with broken rotor bars with motor at full load.

Load = 100% k =1	Healthy Motor		Faulty Motor with 3 broken bars		Result
	Frequency [Hz]	Amplitude [dB]	Frequency [Hz]	Amplitude [dB]	Amplitude diff. [dB]
$f_{bu} = f_1(1 + 2ks)$	52.23	-50.85	52.53	-40.55	-10.30
$f_{bl} = f_1(1 - 2ks)$	47.47	-49.39	47.23	-41.71	-7.68

5.5.2 MCSA: Broken rotor bar fault with load variation

From full load, the motor was decreased in load to 50% and then to no-load. The recorded data was then processed and fault frequencies re-calculated based on the decreased slip. The results are presented in the table below:

Table 5-10: Fault component frequencies and amplitudes associated with the broken rotor bar motor at various loads.

k=1	Healthy Motor		Faulty Motor with 3 broken bars		Result
	Frequency [Hz]	Amplitude [dB]	Frequency [Hz]	Amplitude [dB]	Amplitude diff. [dB]
Load = 0%					
$f_{bu} = f_1(1 + 2ks)$	50.55	-46.27	50.53	-38.48	-7.79
$f_{bl} = f_1(1 - 2ks)$	49.55	-45.34	49.43	-38.26	-7.08
Load = 50%					
$f_{bu} = f_1(1 + 2ks)$	51.27	-46.54	51.43	-38.67	-7.87
$f_{bl} = f_1(1 - 2ks)$	48.59	-46.56	48.47	-38.69	-7.87
Load =100%					
$f_{bu} = f_1(1 + 2ks)$	52.23	-50.85	52.53	-40.55	-10.30
$f_{bl} = f_1(1 - 2ks)$	47.47	-49.39	47.23	-41.71	-7.68

From Table 5-10, the fault component amplitude of approximately -38dB showed negligible change between no-load and 50% load operation. Similarly, the amplitude difference between the healthy motor frequency components and faulty motor frequency components remained relatively constant at approximately -7dB. At full load, the upper sideband component showed an increase to -10.3dB whereas the lower sideband remained in the range of -7dB. According to [16] *et al.* the lower sideband is approximately proportional to the number of broken rotor bars, thus explaining why this component remains relatively constant. The decrease in load also naturally reduces the slip thus moving the sidebands closer to the fundamental frequency. This makes detecting broken bars especially difficult when motors are lightly loaded or when newer high efficiency motors are used. The features above can be seen on the following spectrum:

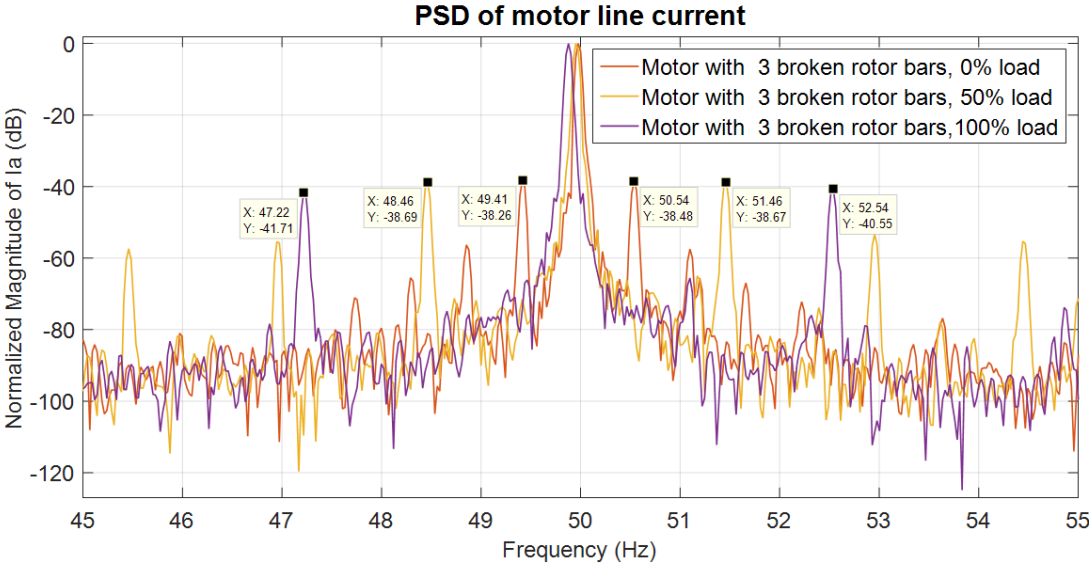


Figure 5-11: Current spectrum of motor with broken rotor bars at various loads.

5.5.3 MCSA - Inverter driven motor with broken rotor bars

After varying the load in the previous test, the motor supply was connected to the inverter drive and run at no load and full load. The following set of results was obtained:

Table 5-11: Fault component frequencies and amplitudes associated with the inverter driven, broken rotor bar motor at no-load and full load.

k = 1	Healthy Motor (inverter)		Faulty Motor with 3 broken bars (inverter)		Result
	Frequency [Hz]	Amplitude [dB]	Frequency [Hz]	Amplitude [dB]	Amplitude diff. [dB]
Load = 0%					
$f_{bu} = f_1(1 + 2ks)$	50.51	-45.59	50.59	-38.93	-6.66
$f_{bl} = f_1(1 - 2ks)$	49.49	-46.19	49.41	-38.85	-7.34
Load = 100%					
$f_{bu} = f_1(1 + 2ks)$	52.66	-53.26	52.81	-41.14	-12.12
$f_{bl} = f_1(1 - 2ks)$	47.34	-50.77	47.19	-42.11	-8.66

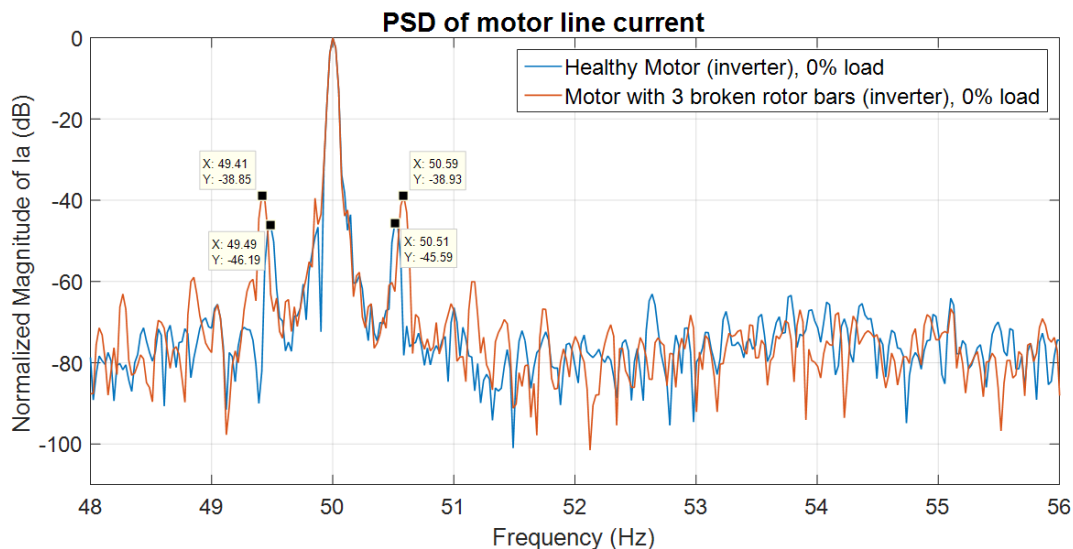


Figure 5-12: Current spectrum of inverter driven motor with broken rotor bars at no-load.

Despite the higher noise level associated with the switching of the inverter drive, the frequency components associated with the broken rotor bar faults are still clearly identifiable, as can be seen in the figure above for the no load case. The spectra produced similar amplitudes at the calculated fault frequencies as compared to the case of the grid connected motor. The amplitude differences are again between -6dB and -8dB, with the exception again being the upper sideband component at full load resulting in a difference of -12.12dB. Thus even with the faulty motor being inverter driven, the broken rotor bars fault were conclusively detected in all cases.

5.6 Broken Rotor Bar Fault Detection using Instantaneous Power Signature Analysis

Having successfully detected the broken rotor bar condition under various conditions using MCSA, the data was reprocessed using IPSA to produce spectra of the instantaneous power.

5.6.1 IPSA: Broken Rotor Bars at 100% load

With the motor at 100% load, the following spectra were produced, showing the two fault component frequencies and their multiples.

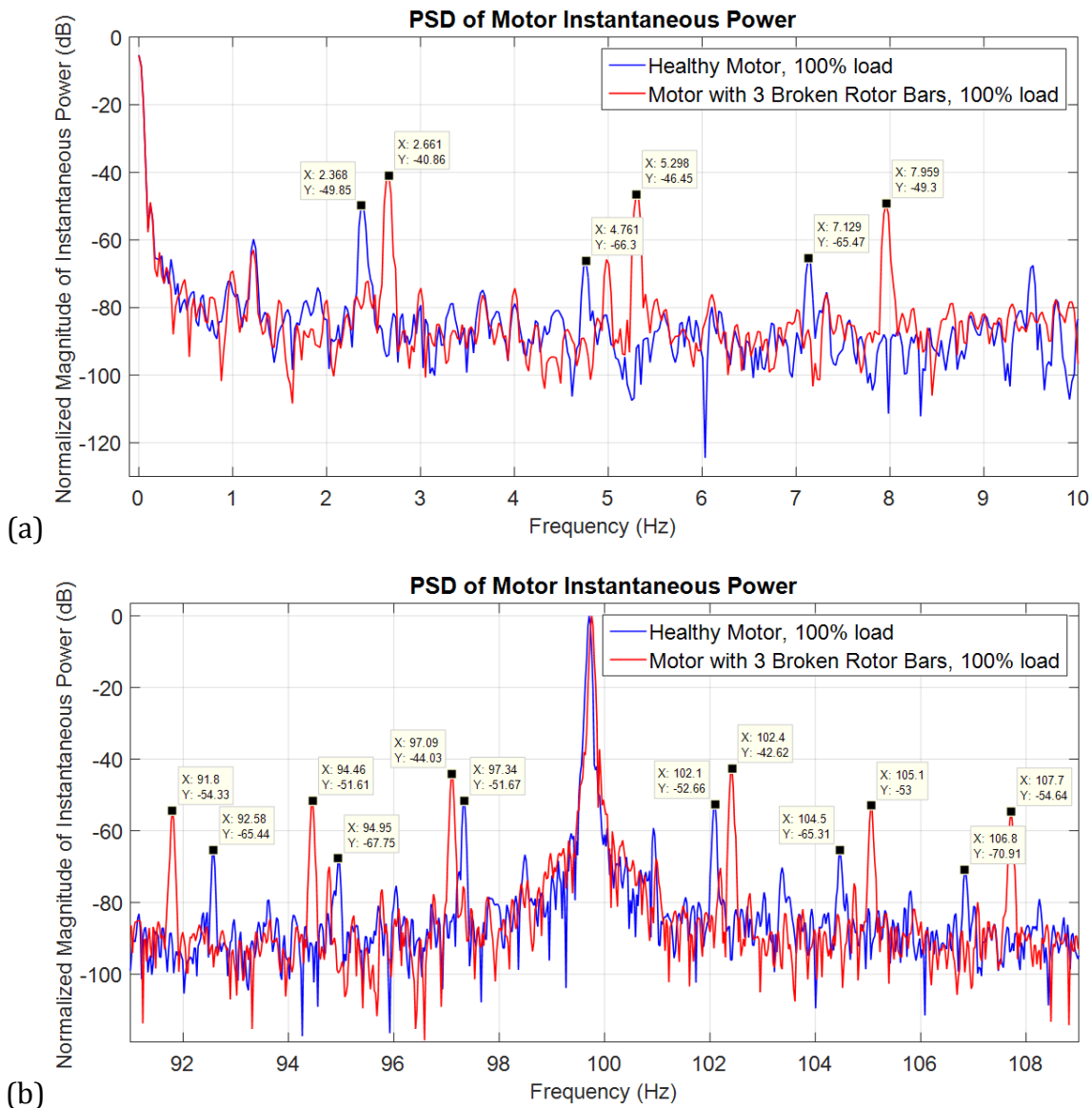


Figure 5-13: PSD's of motor instantaneous power showing broken rotor bar components (a) f_{br1} and (b) f_{br2}

From the results it clear that the fault components associated with the broken rotor bars are unique when compared to classical MCSA. For the sake of comparison, $k = 1$ is chosen for discussion. The first component f_{br1} at twice the slip frequency produces a unique low frequency component which showed significant amplitude change of -8.99dB when the fault was introduced. The second sideband components showed the translation to twice the line frequency expected when using the instantaneous power. From Table 5-12 below, the sideband components showed significant change in amplitude to conclusively detect the presence of the fault. The results are also very close to the values obtained using MCSA, which produced upper and lower sideband amplitude differences of -10.3dB and -7.68dB respectively.

Table 5-12: Fault component frequencies and amplitudes associated with broken rotor bars with motor at full load using IPSA.

Load = 100% k=1	Healthy Motor		Faulty Motor with 3 broken bars		Result
	Frequency [Hz]	Amplitude [dB]	Frequency [Hz]	Amplitude [dB]	Amplitude diff. [dB]
$f_{br1} = 2ksf_1$	2.368	-49.85	2.661	-40.86	-8.99
$f_{br2U} = 2f_1(1 + ks)$	102.1	-52.66	102.4	-42.62	-10.04
$f_{br2L} = 2f_1(1 - ks)$	97.34	-51.67	97.09	-44.03	-7.64

5.6.2 IPSA: Broken rotor bar fault with load variation

The data for the faulty motor with broken rotor bars at 0% and 50% load were also reprocessed using the IPSA algorithm. From the data (Table 5-13) and accompanying spectra, it is evident that the fault component amplitudes show little variation with load, remaining on average at approximately -40dB.

However, the amplitude difference used for detecting the fault shows different behavior for the different components and sidebands. The first fault component at twice slip frequency f_{br1} shows a consistent increase in fault level (difference) as the motor load is increased. Similarly, the upper sideband of the second fault component f_{br2U} shows a similar trend. The lower sideband component f_{br2L} remains relatively stable with load at approximately -8dB. Hence, the broken rotor bar faults could be detected at all tested loads. It is also

notable that the sideband components displayed similar behavior and fault levels when compared to the MCSA results.

Table 5-13: Fault component frequencies and amplitudes associated with the broken rotor bar motor at various loads using IPSA.

k = 1	Healthy Motor		Faulty Motor with 3 broken bars		Result
	Frequency [Hz]	Amplitude [dB]	Frequency [Hz]	Amplitude [dB]	Amplitude diff. [dB]
Load = 0%					
$f_{br1} = 2ksf_1$	0.488	-45.16	0.5615	-40.51	-4.65
$f_{br2U} = 2f_1(1 + ks)$	100.6	-45.69	100.5	-40.01	-5.68
$f_{br2L} = 2f_1(1 - ks)$	99.63	-48.18	99.39	-39.93	-8.25
Load = 50%					
$f_{br1} = 2ksf_1$	1.343	-47.12	1.489	-39.81	-7.31
$f_{br2U} = 2f_1(1 + ks)$	101.2	-48.44	101.4	-39.93	-8.51
$f_{br2L} = 2f_1(1 - ks)$	98.54	-48.14	98.41	-40.09	-8.05
Load = 100%					
$f_{br1} = 2ksf_1$	2.368	-49.85	2.661	-40.86	-8.99
$f_{br2U} = 2f_1(1 + ks)$	102.1	-52.66	102.4	-42.62	-10.04
$f_{br2L} = 2f_1(1 - ks)$	97.34	-51.67	97.09	-44.03	-7.64

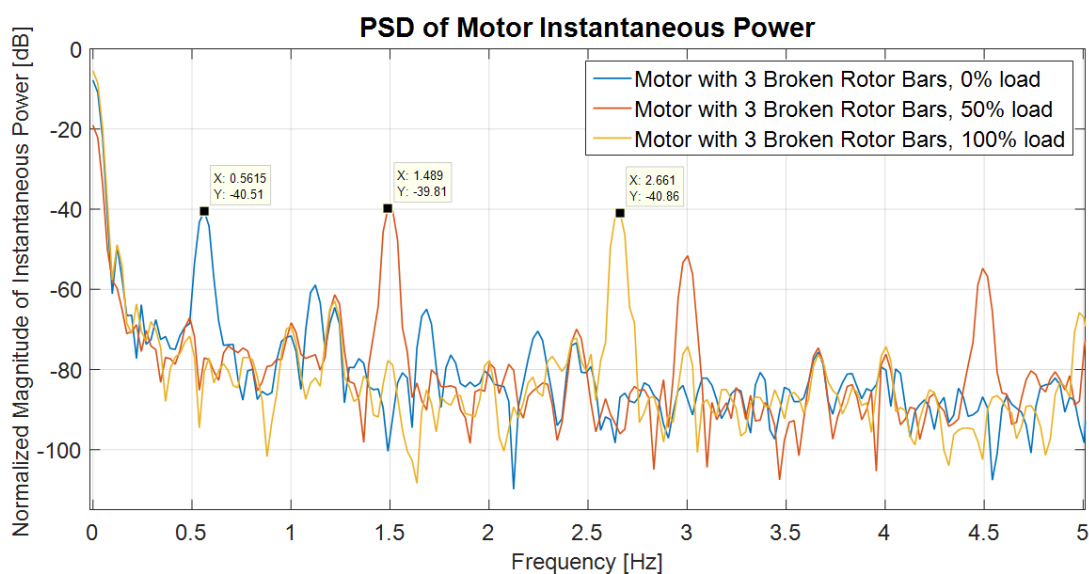


Figure 5-14: Instantaneous power spectrum of motor with broken rotor bars at various loads showing f_{br1} frequencies.

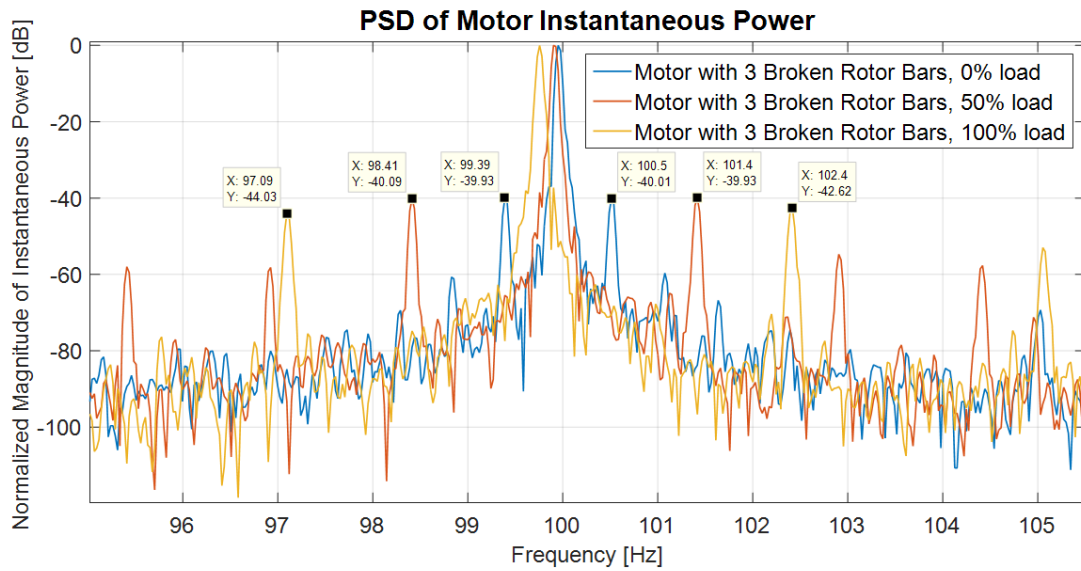


Figure 5-15: Instantaneous power spectrum of motor with broken rotor bars at various loads showing f_{br2} upper and lower sideband frequencies.

5.6.3 IPSA - Inverter driven motor with broken rotor bars

The data sets for the inverter driven motor with broken rotor bars were reprocessed using the IPSA algorithm. The results for the frequency components for $k = 1$ with the motor at no-load and full load are presented in Table 5-14 below.

Table 5-14: Fault component frequencies and amplitudes associated with the inverter driven, broken rotor bar motor at no-load and full load processed using IPSA.

IPSA; k=1	Healthy Motor (inverter)		Faulty Motor with 3 broken bars (inverter)		Result Amplitude diff. [dB]
	Frequency [Hz]	Amplitude [dB]	Frequency [Hz]	Amplitude [dB]	
Load = 0%					
$f_{br1} = 2ksf_1$	0.5127	-47.67	0.5859	-41	-6.67
$f_{br2U} = 2f_1(1 + ks)$	100.5	-46.96	100.6	-38.2	-8.76
$f_{br2L} = 2f_1(1 - ks)$	99.49	-47.07	99.41	-39.35	-7.72
Load = 100%					
$f_{br1} = 2ksf_1$	2.832	-41.46	2.661	-50.68	-9.22
$f_{br2U} = 2f_1(1 + ks)$	102.8	-41.6	102.7	-52.06	-10.46
$f_{br2L} = 2f_1(1 - ks)$	97.17	-44.82	97.36	-52.32	-7.5

Similar to the grid connected case, the broken rotor bar fault could be detected through all three components, while producing similar fault levels to the former case. The spectra associated with these tests are presented below:

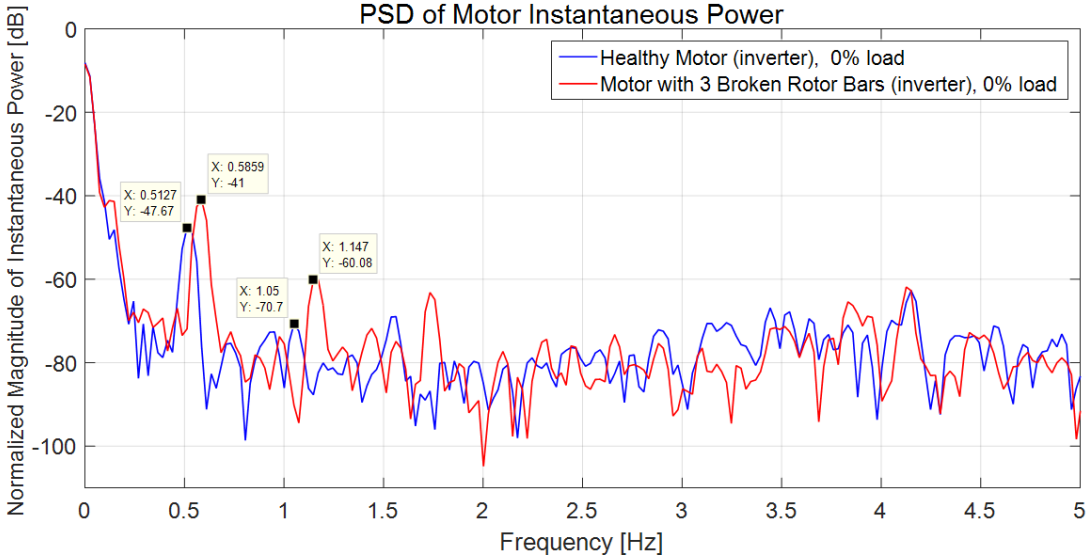


Figure 5-16: Instantaneous power spectrum of inverter driven motor with broken rotor bars at no-load showing f_{br1} frequencies for $k = 1$ and 2 .

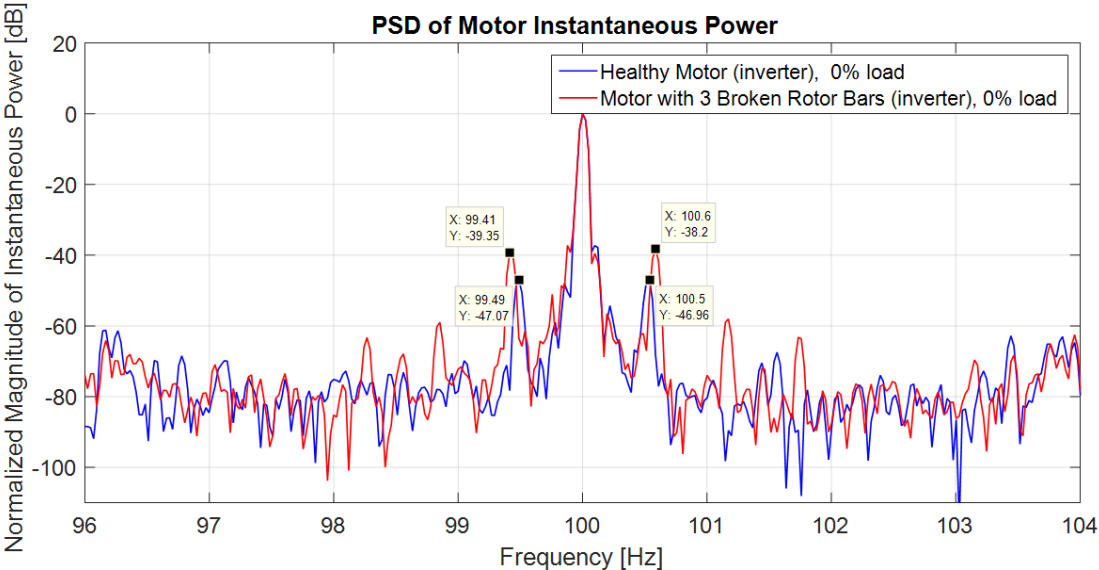


Figure 5-17: Instantaneous power spectrum of inverter driven motor with broken rotor bars at no-load showing f_{br2} upper and lower sideband frequencies for $k = 1$.

5.7 Broken Rotor Bar Fault Detection using Motor Square Current Signature Analysis

The dataset used in the previous broken rotor bar tests was reprocessed and analysed by using the square of the instantaneous current signal. The results are now presented:

5.7.1 MSCSA: Grid connected broken rotor bar motor

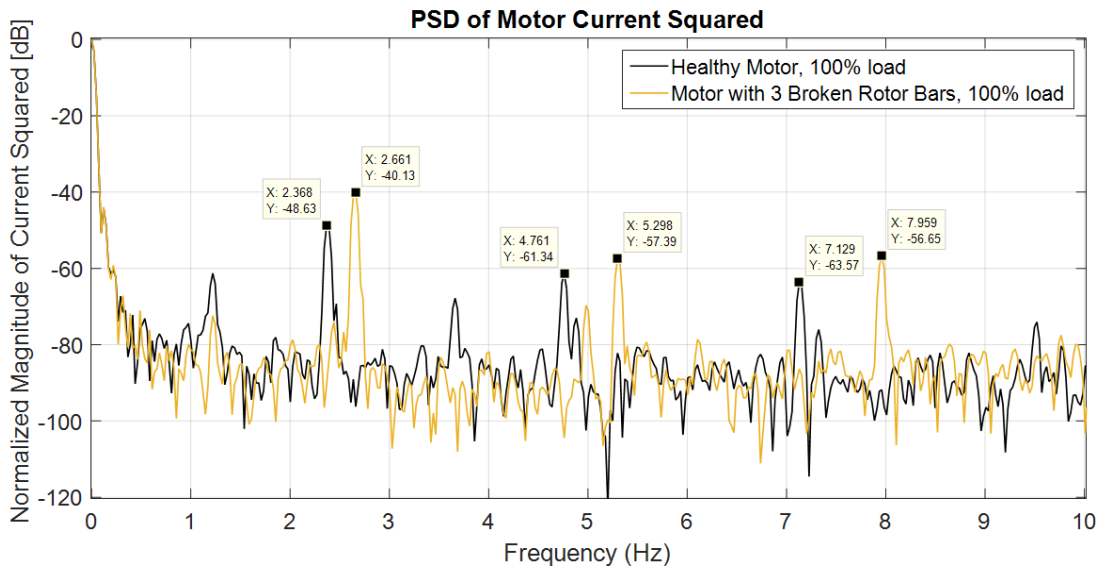
The results for the grid connected case for all tested load conditions are presented below. The results show that the fault component amplitudes display similar behavior with load as the results using IPSA. The amplitude difference between the healthy and faulty components show that the broken rotor bar condition for the grid connected motor could be detected by significant changes in all the fault components at all tested loads.

Table 5-15: Fault component frequencies and amplitudes associated with the broken rotor bar motor at various loads using MSCSA.

k = 1	Healthy Motor		Faulty Motor with 3 broken bars		Result
	Frequency [Hz]	Amplitude [dB]	Frequency [Hz]	Amplitude [dB]	Amplitude diff. [dB]
Load = 0%					
$f_{br1} = 2ksf_1$	0.4883	-40.44	0.5615	-33.74	-6.7
$f_{br2U} = 2f_1(1 + ks)$	100.6	-48.81	100.5	-39.89	-8.92
$f_{br2L} = 2f_1(1 - ks)$	99.63	-49.69	99.39	-40.6	-9.09
Load = 50%					
$f_{br1} = 2ksf_1$	1.343	-43.23	1.489	-35.86	-7.37
$f_{br2U} = 2f_1(1 + ks)$	101.2	-49.03	101.4	-40.12	-8.91
$f_{br2L} = 2f_1(1 - ks)$	98.54	-48.41	98.41	-40.82	-7.59
Load = 100%					
$f_{br1} = 2ksf_1$	2.368	-48.63	2.661	-40.13	-8.5
$f_{br2U} = 2f_1(1 + ks)$	102.1	-52.96	102.4	-42.14	-10.82
$f_{br2L} = 2f_1(1 - ks)$	97.34	-50.45	97.09	-44.08	-6.37

The spectra for the motor at full load are presented overleaf:

(a)



(b)

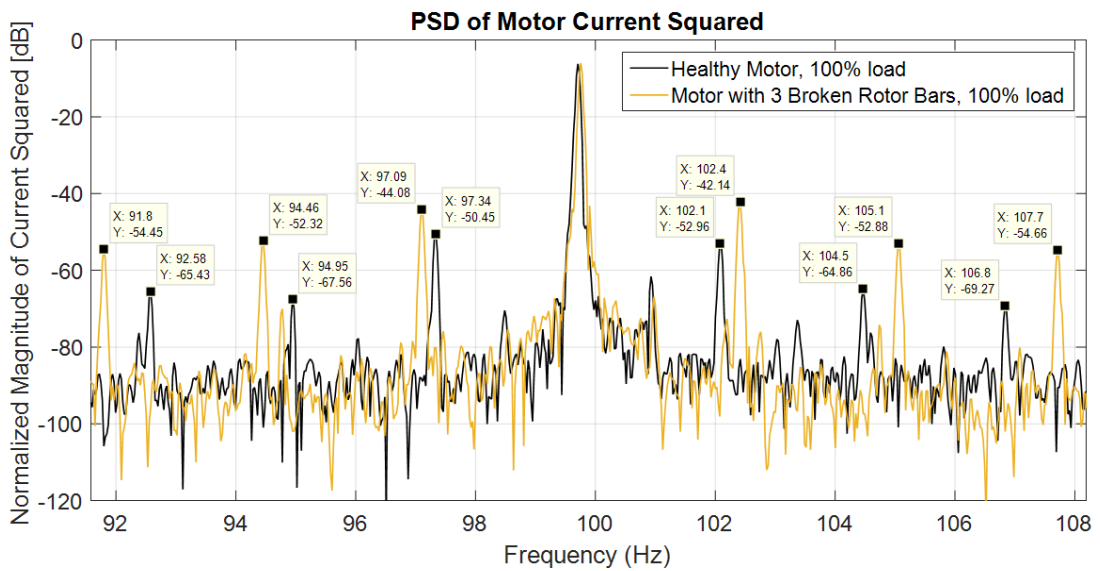


Figure 5-18: PSD's of motor squared current showing broken rotor bar components (a) f_{br1} and (b) f_{br2} for $k = 1, 2, 3$.

From the spectra, showing healthy and faulty component frequencies for $k = 1, 2, 3$, the difference between healthy and faulty components can clearly be seen.

5.7.2 MSCSA - Inverter driven motor with broken rotor bars

The inverter supplied motor data was subsequently processed using the MSCSA algorithm. The results in Table 5-16 below clearly show a significant difference in amplitude between the faulty and healthy frequency component amplitudes, thus conclusively showing the presence of the broken rotor fault.

Table 5-16: Fault component frequencies and amplitudes associated with the inverter driven broken rotor bar motor at various loads using MSCSA.

MSCSA; k = 1	Healthy Motor (inverter)		Faulty Motor with 3 broken bars (inverter)		Result Amplitude diff. [dB]
	Frequency [Hz]	Amplitude [dB]	Frequency [Hz]	Amplitude [dB]	
Load = 0%					
$f_{br1} = 2ksf_1$	0.5859	-41.08	0.5127	-33.26	-7.82
$f_{br2U} = 2f_1(1 + ks)$	100.5	-47.87	100.6	-39.14	-8.73
$f_{br2L} = 2f_1(1 - ks)$	99.49	-46.29	99.41	-39.97	-6.32
Load = 100%					
$f_{br1} = 2ksf_1$	2.661	-50.74	2.832	-40.73	-10.01
$f_{br2U} = 2f_1(1 + ks)$	102.7	-52.84	102.8	-41.14	-11.7
$f_{br2L} = 2f_1(1 - ks)$	97.36	-50.79	97.17	-44.07	-6.72

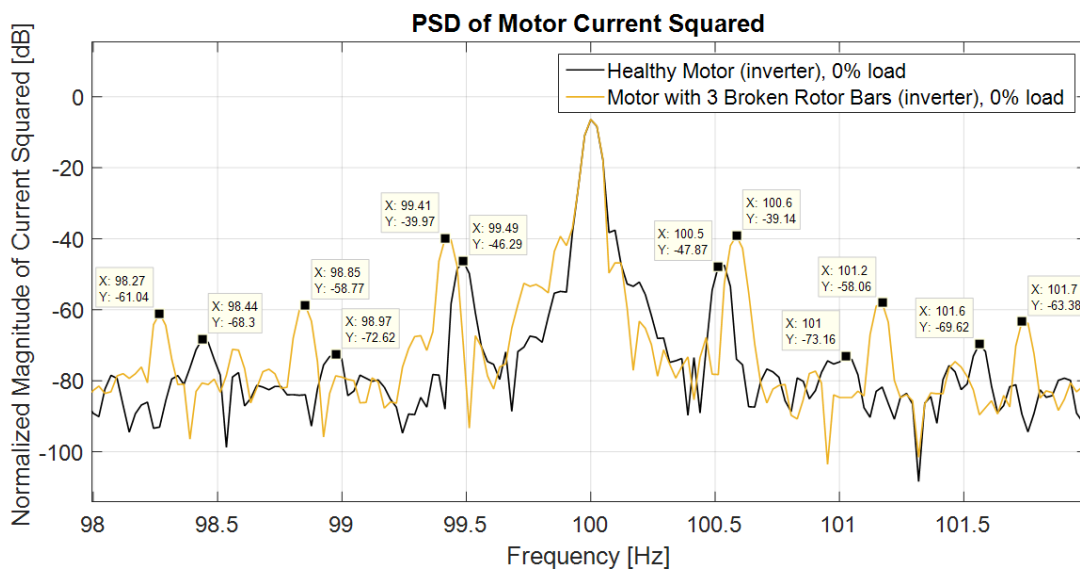


Figure 5-19: Squared Current spectrum of the inverter driven motor with broken rotor bars at no-load showing f_{br2} upper and lower sideband frequencies for k = 1, 2, 3.

5.7.3 Similarities between IPSA and MSCSA

From the theory presented in 3.2, it is expected that the spectra of the instantaneous power and the square of the current would be very similar to each other in all aspects. This can be seen in the spectrum below, which overlays the squared current and instantaneous power.

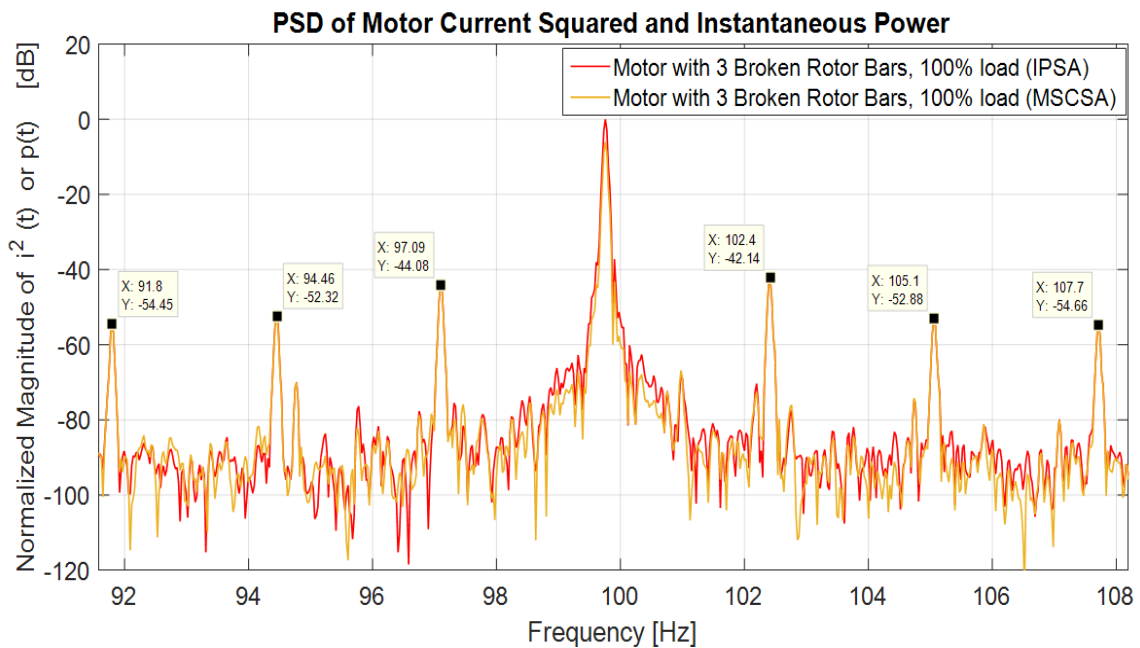


Figure 5-20: Comparative spectrum of the squared current and instantaneous power for $k = 1, 2, 3$.

A summary of the fault levels obtained using the instantaneous power and the squared current is presented in Table 5-17 and 5-18 overleaf for the grid and inverter connected cases. From the data it can be observed that the two techniques yield very similar fault levels for the same set of data.

Hence both techniques serve to confirm the results obtained from classical current analysis, with the former techniques both providing conclusive results using unique frequencies when compared to those associated with the current.

Table 5-17: Results comparison between IPSA and MSCSA for broken rotor bar case.

Grid; k=1	IPSA	MSCSA
	Amplitude diff. [dB]	Amplitude diff. [dB]
Load = 0%		
$f_{br1} = 2ksf_1$	-4.65	-6.7
$f_{br2U} = 2f_1(1 + ks)$	-5.68	-8.92
$f_{br2U} = 2f_1(1 - ks)$	-8.25	-9.09
Load = 50%		
$f_{br1} = 2ksf_1$	-7.31	-7.37
$f_{br2U} = 2f_1(1 + ks)$	-8.51	-8.91
$f_{br2U} = 2f_1(1 - ks)$	-8.05	-7.59
Load = 100%		
$f_{br1} = 2ksf_1$	-8.99	-8.5
$f_{br2U} = 2f_1(1 + ks)$	-10.04	-10.82
$f_{br2U} = 2f_1(1 - ks)$	-7.64	-6.37

Table 5-18: Results comparison between IPSA and MSCSA for broken rotor bar case using the inverter drive.

Inverter; k=1	IPSA	MSCSA
	Amplitude diff. [dB]	Amplitude diff. [dB]
Load = 0%		
$f_{br1} = 2ksf_1$	-6.67	-7.82
$f_{br2U} = 2f_1(1 + ks)$	-8.76	-8.73
$f_{br2U} = 2f_1(1 - ks)$	-7.72	-6.32
Load = 100%		
$f_{br1} = 2ksf_1$	-9.22	-10.01
$f_{br2U} = 2f_1(1 + ks)$	-10.46	-11.7
$f_{br2U} = 2f_1(1 - ks)$	-7.5	-6.72

5.8 The Effect of Field Weakening on Broken Rotor Bar Fault Detection

In section 2.2.3, the performance characteristics of the induction machine were reviewed. Importantly, it was noted that the mechanical torque developed by the machine at a given speed is proportional to the square of the supply voltage of the machine [9]. From the foregoing test results, it is evident that the most difficult condition to detect broken rotor bars is when the machine is lightly loaded or at no-load. This may also be the case when high efficiency motors are employed that operate at low slip, thus resulting in the fundamental frequency masking the sidebands associated with the rotor fault in the current spectrum. Theoretically, a simple way to distance the sidebands from the fundamental is to increase the load and hence the slip. However, when the load torque is fixed for a given process, as is commonly the case, and is relatively low in magnitude, detecting broken rotor bars can be problematic. Thus from the previously stated theory, to increase the slip for a fixed load torque, the supply voltage could be decreased, which mimics the effect of field weakening since the motor is grid connected and the frequency is fixed. This effectively results in lower operating currents and speed. This effect will now be tested and quantified in the following section.

5.8.1 Motor at no-load with 10% supply voltage reduction

The first test conducted was at rated voltage (190V) reduced by 10%. The Variac that forms part of the experimental setup was adjusted to 170V. As a result, the motor at no-load drew 1.1A of current during steady state operation. This was done to the healthy motor as well as the faulty motor to obtain experimental data. The data was then compared to the broken rotor bar case at rated voltage and processed using the three techniques to assess the impact of the field weakening. Using MCSA, the following spectrum was obtained:

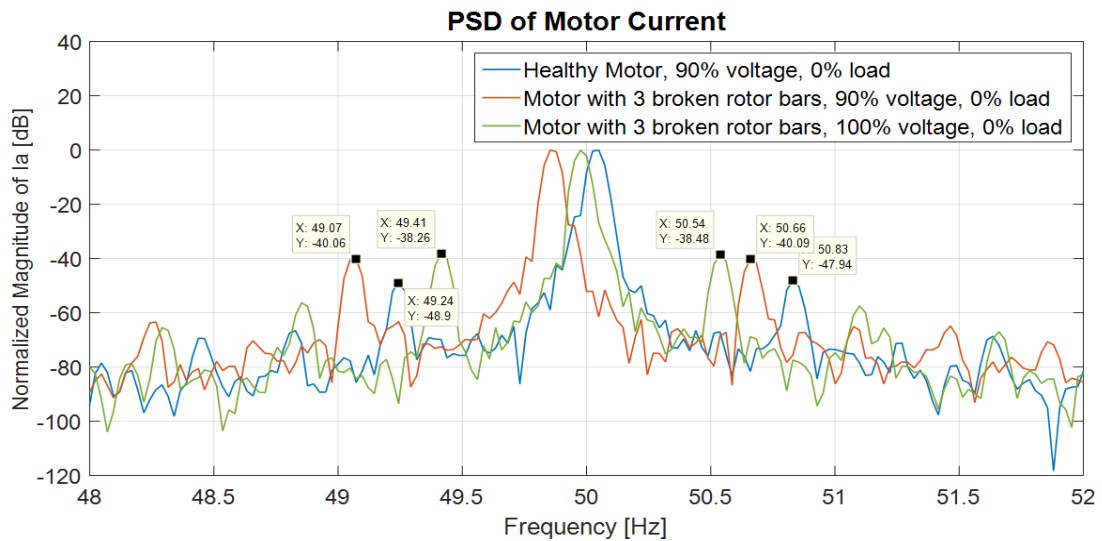


Figure 5-21: PSD of motor current for a 10% voltage reduction compared to a broken rotor bar fault at rated voltage.

From the spectrum it can be observed that the upper and lower sideband components at the reduced voltage show a reduction in amplitude when compared to the same motor at rated voltage. This is expected due to the slight reduction in steady state current. However, the difference in amplitude between the fault components at reduced voltage show minimal change when compared to the previous results at rated voltage. The amplitude difference between the healthy and faulty components at reduced voltage were found to be -7.87dB and -8.84dB for the upper and lower sidebands respectively, in comparison to -7.79dB and -7.08dB at rated voltage.

To quantify the effect of the change in voltage on the position of the sidebands, the frequency difference between the fault component and its associated fundamental is computed, since the fundamental frequency is different between the data sets. The following results were obtained.

Table 5-19: Summary of sideband distance from the fundamental frequency using MCSA.

MCSA Load = 0%	Healthy motor 90% V	Faulty motor 90% V	Faulty motor 100% V	Frequency shift between fault components [Hz]
	Frequency [Hz]	Frequency [Hz]	Frequency [Hz]	
Fundamental Frequency	50.05	49.85	49.98	
Distance from fundamental f_{brU}	-0.78	-0.81	-0.56	0.25
Distance from fundamental f_{brL}	0.81	0.78	0.57	-0.21

From the results above, it is evident that the 10% reduction in voltage resulted in an average absolute change of 0.23Hz to the position of the sidebands with respect to the sidebands at rated voltage. The effects are now examined in the instantaneous power spectrum.

Table 5-20: Summary of sideband distance from the fundamental frequency using IPSA.

IPSA Load = 0%	Healthy motor 90% V	Faulty motor 90% V	Faulty motor 100% V	Frequency shift between fault components
	Frequency [Hz]	Frequency [Hz]	Frequency [Hz]	[Hz]
2 X Fundamental Frequency	100.1	99.7	99.96	
Distance from DC component f_{br1}	0.81	0.81	0.56	0.24
Distance from 2 X fundamental f_{br2U}	0.80	0.80	0.54	0.26
Distance from 2 X fundamental f_{br2L}	-0.77	-0.83	-0.57	-0.26

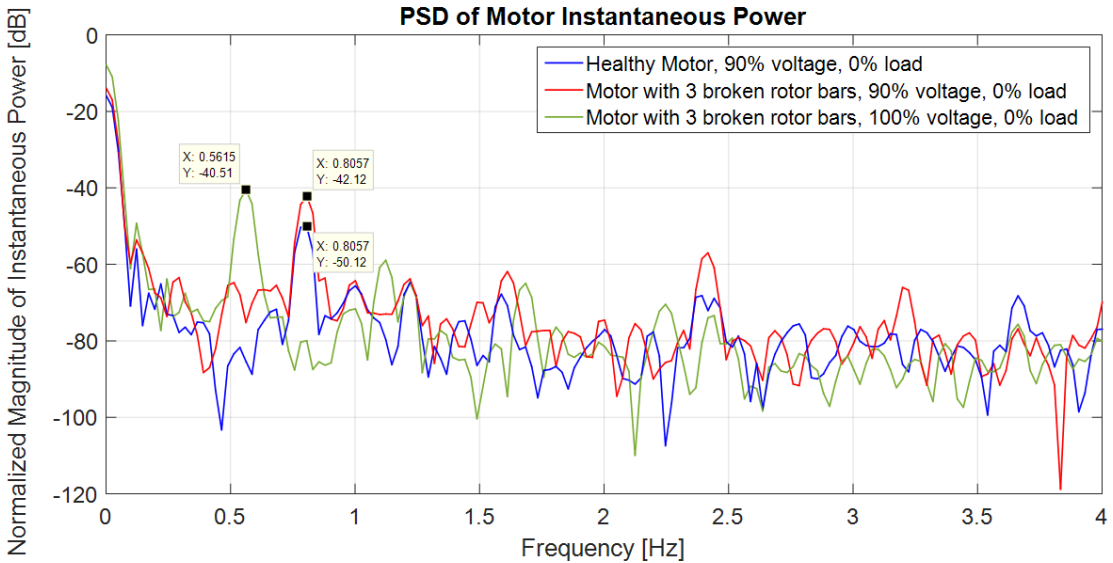


Figure 5-22: PSD of motor instantaneous power showing a shift in frequency between fault components f_{br1} due to field weakening.

From Table 5-20, the field weakening effect is translated into the instantaneous power spectrum as can be seen by the similar frequency shift in all the fault components. Hence the power spectrum brings no new information in this regard, except showing the frequency shift at different points in the spectrum. Since the spectra of instantaneous power and the square of the current are very similar, the results for square current analysis are included in Appendix B for completeness.

5.8.2 Motor at no-load with 20% supply voltage reduction

Further tests were conducted with the supply voltage reduced by 20% to 150V, with the motor operating at no-load in steady state. By decreasing the supply voltage by an additional 10%, the frequency shift effectively doubled from that of the previous test when MCSA spectra were used. Similar results were obtained when using instantaneous power and squared current spectra. These results are summarized in Table 5-21 and 5-22 below:

Table 5-21: Summary of sideband distance from the fundamental frequency using MCSA at 80% rated voltage.

MCSA Load = 0%	Healthy motor 80% V	Faulty motor 80% V	Faulty motor 100% V	Frequency shift between fault components
	Frequency [Hz]	Frequency [Hz]	Frequency [Hz]	[Hz]
Fundamental Frequency	50.05	49.85	49.98	
Distance from fundamental f_{brU}	-1.01	-1.01	-0.56	0.45
Distance from fundamental f_{brL}	1	1.02	0.57	-0.45

Table 5-22: Summary of sideband distance from the fundamental frequency using IPSA at 80% rated voltage.

IPSA Load = 0%	Healthy motor 80% V	Faulty motor 80% V	Faulty motor 100% V	Frequency shift between fault components
	Frequency [Hz]	Frequency [Hz]	Frequency [Hz]	[Hz]
2 X Fundamental Frequency	100.04	100.04	99.96	
Distance from DC component f_{br1}	0.97	1.00	0.55	0.45
Distance from 2 X fundamental f_{br2U}	0.96	0.96	0.54	0.42
Distance from 2 X fundamental f_{br2L}	-0.97	-1.02	-0.57	-0.45

5.8.3 Concluding remarks

The three analysis techniques tested on the motor with broken rotor bars proved conclusive in detecting the fault under all load and supply conditions. The effect of field weakening at no-load was also tested to quantify the effect on the fault component position relative to the fundamental.

5.9 Bearing Fault Detection using Motor Current Signature Analysis

The final test case was for a motor with a bearing inner and outer race fault. Data was recorded for the motor supplied by the grid and an inverter at varying loads, in accordance with the experimental procedure from section 4.3.2. Based on the bearing information, the fault frequencies for the inner and outer race faults were calculated using the frequency estimation equations (3.18) and (3.19). The fault component translation into the current spectrum was then calculated using equation (3.17) and compared to the spectra generated using the MATLAB algorithm. The results for the positive components are now presented. Detailed results can be found in Appendix B.

5.9.1 MCSA: Bearing outer race fault

The stationary outer race of the test motor contained a single point defect that manifested in the current spectrum due to the resultant vibration affecting the airgap flux density [8]. The calculated fault frequencies based on equations (3.17) for the current spectrum are presented below:

Table 5-23: Calculated frequencies of outer raceway fault components for healthy and faulty motors at various loads.

Load [%]	Healthy Motor	Faulty Motor
	Calculated Frequency [Hz]	Calculated Frequency [Hz]
0	209.4	209.9
50	207.6	207.7
100	206.6	206.7

The data for the faulty motor was processed using the MCSA algorithm and produced the spectra presented overleaf. From the spectra the actual fault frequencies were obtained and presented below:

Table 5-24: Actual outer race fault frequencies and amplitudes at various motor loads.

Load [%]	Healthy Motor		Faulty Motor (outer race)		Result
	Actual Frequency [Hz]	Amplitude [dB]	Actual Frequency [Hz]	Amplitude [dB]	Amplitude difference [dB]
0	203.7	-103.5	203.7	-93.16	-10.34
50	203.1	-95.2	203.3	-75.32	-19.88
100	201.6	-98.57	201.7	-85.69	-12.88

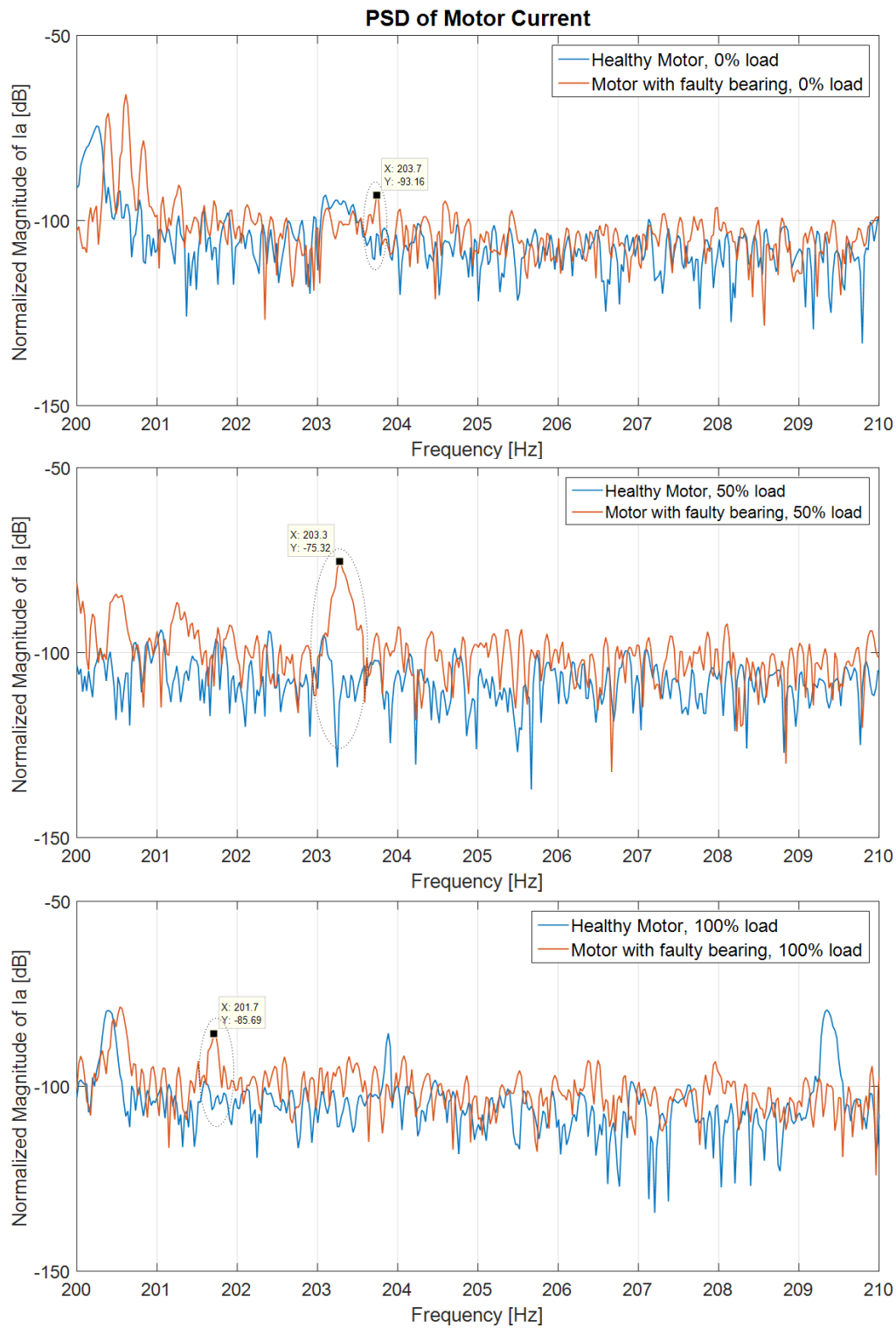


Figure 5-23: PSD of motor current showing bearing outer race fault components at 0%, 50% and 100% load respectively.

From the spectra it can be observed that the actual outer race fault frequencies are different to the calculated values. This is due to the nature of the equation used, as well as the fact that the bearing fault in the test motor is manufactured, thus making the fault behaviour more unpredictable with time when compared to normal fault progression [24].

The results show that the amplitude difference of the fault components associated with the outer race fault exhibit no clear relationship with load. However, the frequency of the fault components decreases with load, since the fault frequency is speed dependent. In conclusion, the outer race fault was detected at all load levels in the grid connected motor with all fault components showing amplitude changes of greater than 10dB.

5.9.2 MCSA: Bearing inner race fault

From the same data set and spectra, the bearing inner race fault frequencies and PSD’s were calculated. The calculated bearing fault frequencies for various load levels are listed below:

Table 5-25: Calculated frequencies of inner raceway fault components for healthy and faulty motors at various loads.

Load [%]	Healthy Motor	Faulty Motor
	Calculated Frequency [Hz]	Calculated Frequency [Hz]
0	289.1	289.8
50	286.4	286.6
100	284.8	284.9

The actual inner race fault frequencies and magnitudes were obtained from the current spectra overleaf.

Table 5-26: Actual inner race fault frequencies and amplitudes at various motor loads.

Load [%]	Healthy Motor		Faulty Motor (inner race)		Result
	Actual Frequency [Hz]	Amplitude [dB]	Actual Frequency [Hz]	Amplitude [dB]	Amplitude difference [dB]
0	289	-103	289.1	-95.63	-7.37
50	284.7	-108.2	284.6	-96.14	-12.06
100	284	-103.1	283.9	-89.06	-14.04

From the table of results above, the inner race fault amplitude differences shows a more consistent increase in magnitude with increasing load. This is likely due to the shorter transmission path for the vibration through the rotor structure when compared to the

outer race. The fault location in terms of frequency also shows the expected decrease as load and thus slip is increased. Hence, the inner race fault components were successfully identified in this test.

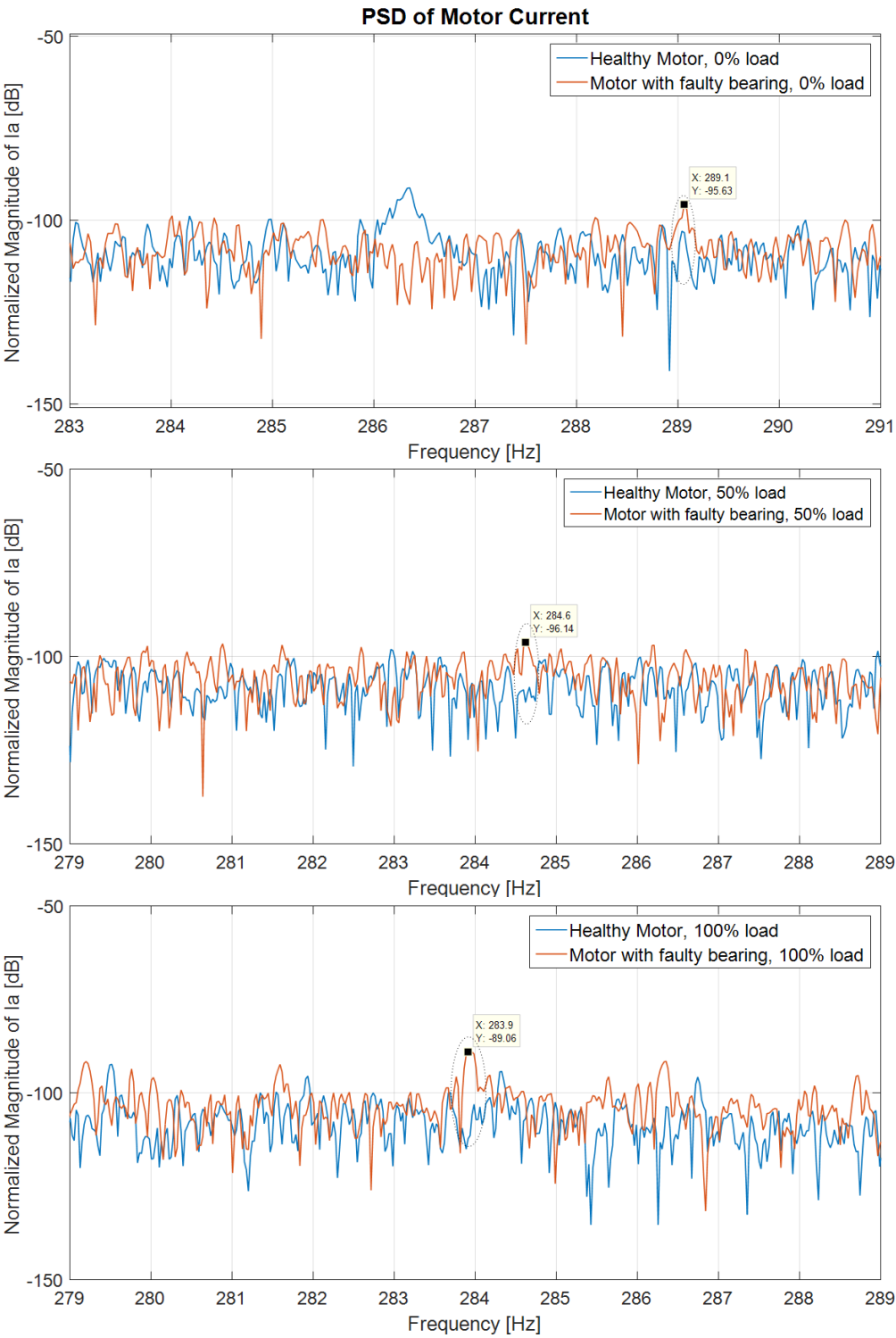


Figure 5-24: PSD's of motor current showing bearing inner race fault components at 0%, 50% and 100% load respectively.

5.9.3 Effects of the inverter on bearing fault detection using MCSA

With the faulty motor connected to the inverter drive, tests were conducted at no-load and full load. At no-load, both the inner and outer race fault could not be detected conclusively due to the increased noise in the spectrum. The higher noise floor combined with the fact that bearing fault signals are low energy signals makes fault detection difficult [28]. At full load, the bearing faults were detected in both races. The full load results are presented below:

Table 5-27: Results for inverter driven motor with bearing fault at full load.

Load = 100 [%]	Healthy Motor		Faulty Motor (outer race)		Result
	Actual Frequency [Hz]	Amplitude [dB]	Actual Frequency [Hz]	Amplitude [dB]	Amplitude difference [dB]
Outer race fault	200.8	-67.03	200.7	-58.77	-8.26
Inner race fault	285.5	-76.1	285.5	-61.96	-14.14

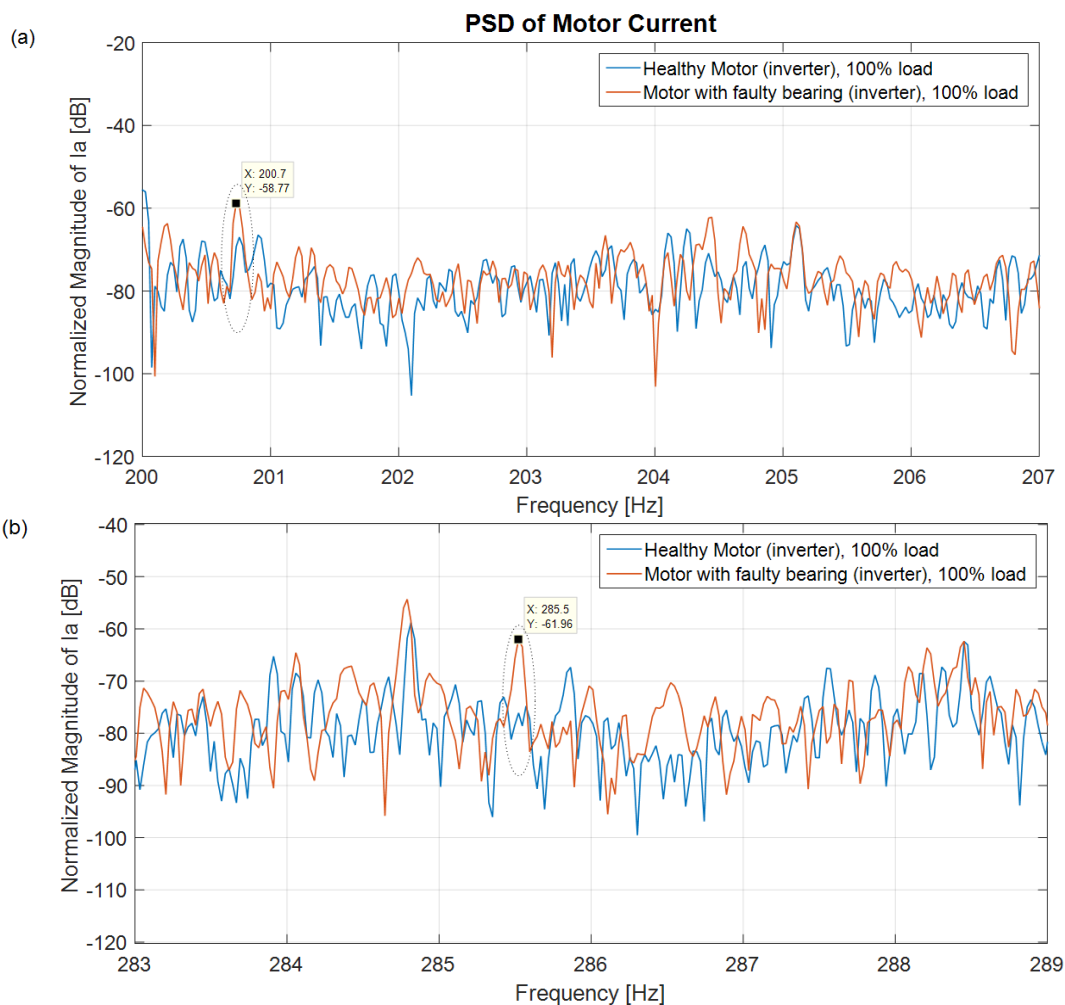


Figure 5-25: Current spectra of inverter driven motor showing (a) outer race and (b) inner race fault components.

5.10 Bearing Fault Detection using Instantaneous Power Signature Analysis

Using the same data for the healthy and faulty motor from the previous section, the Instantaneous Power Signature Analysis technique was applied with aim of detecting the inner and outer race faults.

5.10.1 IPSA: Bearing outer race fault

As explained in section 3.3, the bearing fault frequencies appear directly in the power spectrum at the disturbance frequency. As such, equations (3.18) and (3.19) are used to directly calculate the anticipated inner and outer race fault frequencies. Table 5-28 below presents the calculated values for the different load levels.

Table 5-28: Calculated mechanical frequencies of outer raceway fault components for healthy and faulty motors at various loads.

Load [%]	Healthy Motor	Faulty Motor
	Calculated Frequency [Hz]	Calculated Frequency [Hz]
0	159.4	159.8
50	157.6	157.7
100	156.5	156.6

Using the spectra of the instantaneous power (overleaf) and the calculated fault frequencies, the actual fault frequencies and amplitudes were obtained for the various load levels.

Table 5-29: Actual outer race fault frequencies and amplitudes at various motor loads.

Load [%]	Healthy Motor		Faulty Motor (outer race)		Result
	Actual Frequency [Hz]	Amplitude [dB]	Actual Frequency [Hz]	Amplitude [dB]	Amplitude difference [dB]
0	153.7	-94.6	154.1	-87.45	-7.15
50	153.2	-92.19	153.3	-74.22	-17.97
100	151.6	-86.78	151.6	-77.02	-9.76

Despite producing fault signals with greater magnitudes than classical MCSA, the amplitude difference between the healthy and faulty components is less due to the higher noise floor associated with the instantaneous power spectrum. The fault component amplitudes as

well as the amplitude difference display the same trends with load as the values obtained using classical MCSA. Despite the outer race components being detected, the high noise floor decreases the confidence in the results and hence the technique in the detection of bearing faults.

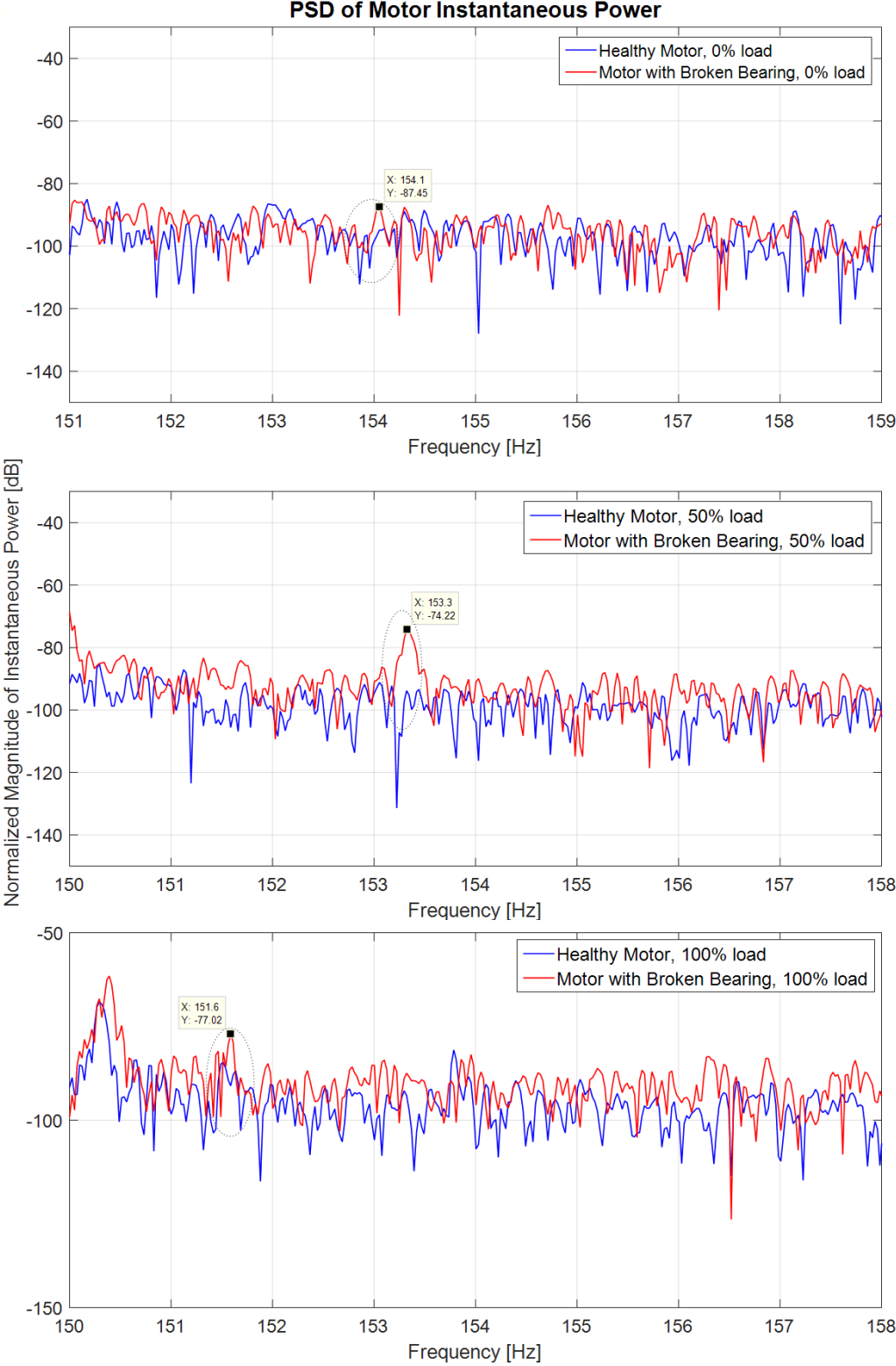


Figure 5-26: Instantaneous power spectra of motor with bearing outer race fault operating at various loads.

5.10.2 IPSA: Bearing inner race fault

Similarly with inner race fault, the anticipated frequencies were calculated and then used to find the actual frequencies in the instantaneous power spectrum. The results for calculated and actual values are presented below.

Table 5-30: Calculated mechanical frequencies of inner raceway fault components for healthy and faulty motors at various loads for use with the instantaneous power spectrum.

Load [%]	Healthy Motor	Faulty Motor
	Calculated Frequency [Hz]	Calculated Frequency [Hz]
0	239.0	239.6
50	236.5	236.6
100	234.7	234.8

Table 5-31: Actual inner race fault frequencies and amplitudes at various motor loads obtained from the instantaneous power spectrum.

Load [%]	Healthy Motor		Faulty Motor (inner race)		Result
	Actual Frequency [Hz]	Amplitude [dB]	Actual Frequency [Hz]	Amplitude [dB]	Amplitude difference [dB]
0	240.2	-99.22	240.1	-90.58	-8.64
50	234.9	-98.55	235.1	-89.45	-9.1
100	231.5	-95.12	231.4	-87.51	-7.61

From the results and the spectra overleaf, the inner race fault components show an increase in magnitude with an increase in load. The fault location on the frequency axis also shifted lower as the motor slip increased with load. Despite showing higher fault component amplitudes than the MCSA equivalents, the power spectrum produces mixed results when the amplitude difference between the healthy and faulty components is computed. This can be attributed to the higher noise levels associated with the instantaneous power spectrum [16]. Hence, similar to the outer race, the inner race fault can be detected, but the results inspire less confidence due to the noisy nature of the spectrum.

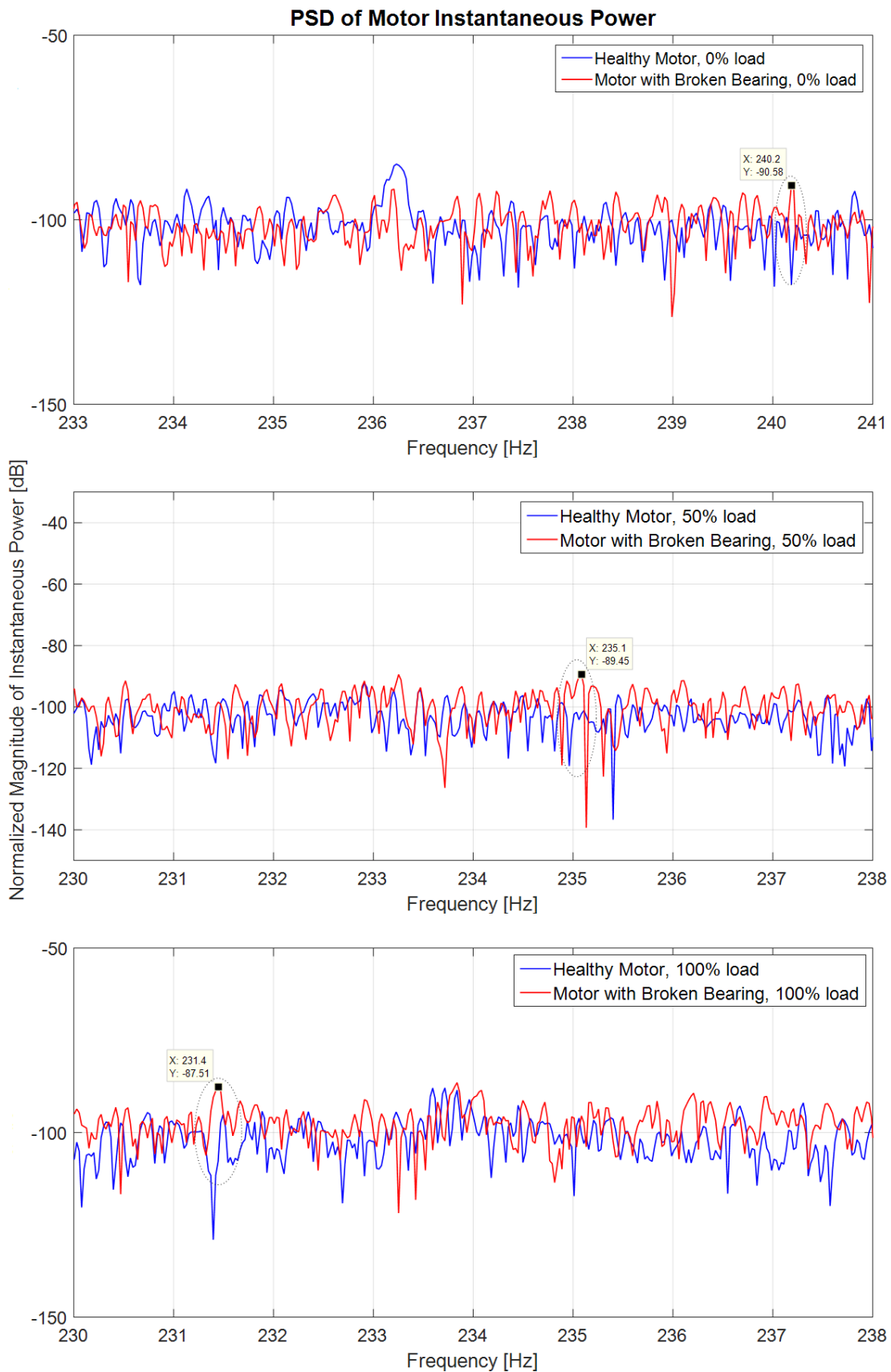


Figure 5-27: PSD of motor instantaneous power showing bearing inner race fault components at 0%, 50% and 100% load respectively.

5.10.3 Effects of the inverter on bearing fault detection using IPSA

Using the inverter driven motor data, and applying the IPSA algorithm, the fault detection procedure was followed in order to detect the inner and outer race faults at no load and full load. In this case, the fault components could not be detected in the instantaneous power spectrum. This is likely due to the inherent noise in the power spectrum coupled with the noise induced in the spectrum due to the switching of the inverter. Figure 5-28 below shows the spectrum in the expected vicinity of the of the outer race fault.

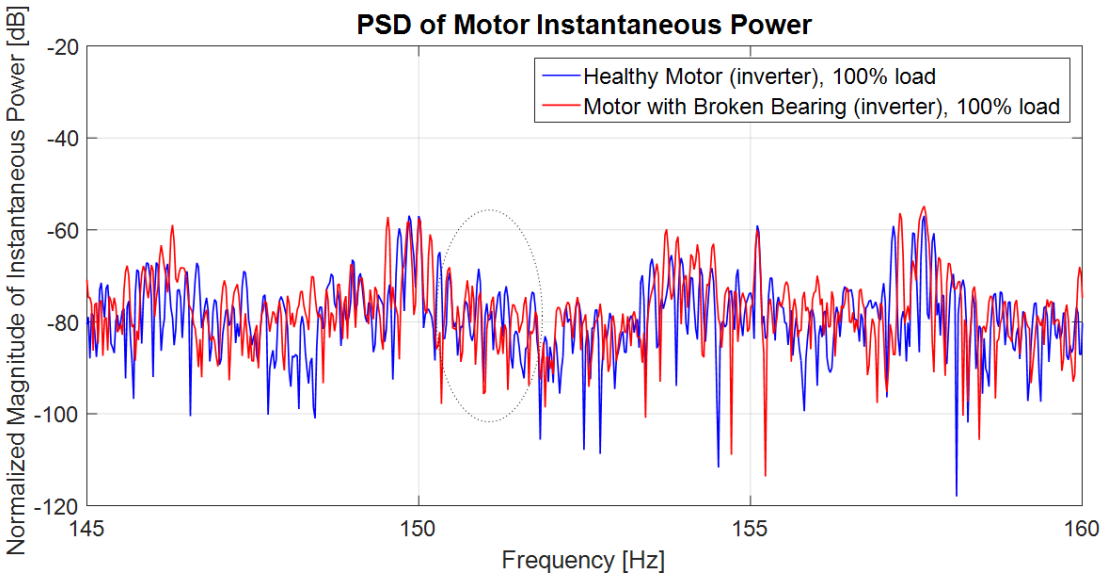


Figure 5-28: PSD of motor instantaneous power showing expected location of the outer race fault for the inverter driven motor at full load.

5.11 Bearing Fault Detection using Motor Square Current Signature

Analysis

The datasets for the motor with the faulty bearing were reprocessed using the square current algorithm. At the time of writing, there had been no work published on detecting bearing faults using the motor square current approach. Based on the similarity of the instantaneous power and square current spectra, one could infer that the vibration disturbances could also appear directly in the square current spectrum. This inference can be tested experimentally by checking the same points in the square current spectrum where the faults were detected in the instantaneous power spectrum.

5.11.1 MSCSA: Bearing outer race fault

With reference to the results in Table 5-29 for the outer race fault components based on instantaneous power, the following results were obtained in the square current spectrum:

Table 5-32: Results of outer race fault component frequencies and amplitudes at various motor loads based on the squared current spectrum.

MSCSA Load [%]	Healthy Motor		Faulty Motor (outer race)		Result
	Actual Frequency [Hz]	Amplitude [dB]	Actual Frequency [Hz]	Amplitude [dB]	Amplitude difference [dB]
0	153.8	-92.15	154	-90.2	-1.95
50	153.2	-94.72	153.3	-77.78	-16.94
100	151.6	-87.27	151.6	-87.39	0.12

At the points of interest, the square current spectrum showed lower amplitudes than the instantaneous power spectrum. At 50% load, a strong outer race fault signal was detected, albeit with a lower amplitude than the comparative signal in the instantaneous power spectrum. At no-load and full load, the fault component amplitudes were embedded in the noise floor of the spectrum and could thus not be detected. Thus for the outer race fault, the square current spectrum at the points investigated provided ambiguous information. The square current spectra largely suffer from the same level of noise as the instantaneous power spectra. Figure 5-29 overleaf shows the outer race fault components at no-load, where the poor signal-to-noise ratio can be observed.

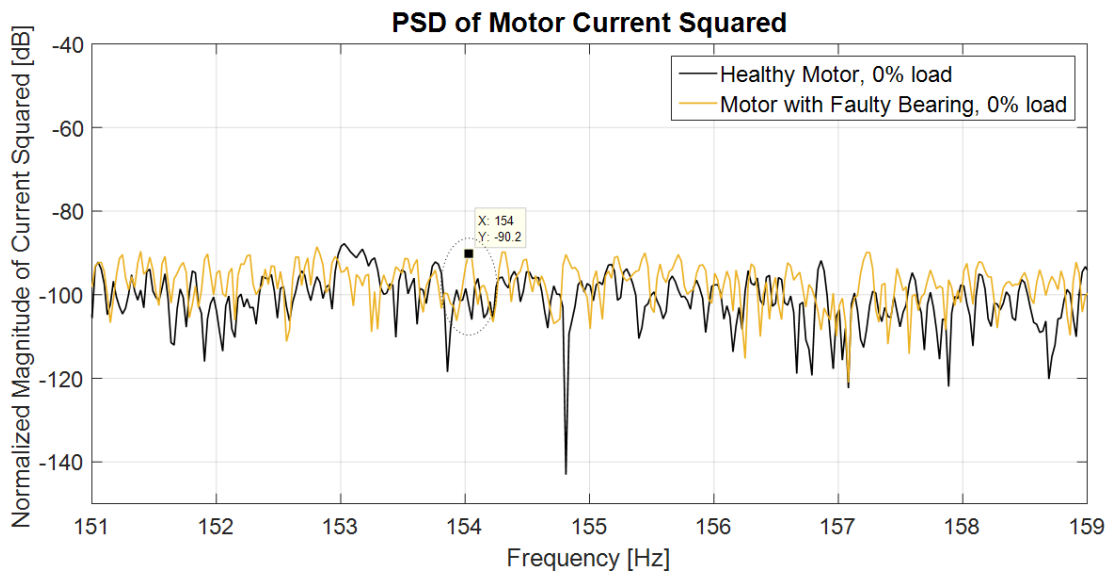


Figure 5-29: PSD of the square of the motor current highlighting the anticipated position of the outer race fault component.

5.11.2 MSCSA: Bearing inner race fault

The inner race fault frequency component locations obtained from the instantaneous power spectrum were examined in the square current spectrum, yielding the following set of results:

Table 5-33: Results of inner race fault component frequencies and amplitudes at various motor loads based on the square current spectrum.

Load [%]	Healthy Motor		Faulty Motor (inner race)		Result
	Actual Frequency [Hz]	Amplitude [dB]	Actual Frequency [Hz]	Amplitude [dB]	Amplitude difference [dB]
0	240.2	-100.4	240.1	-97.11	-3.29
50	235	-101.1	235	-92.77	-8.33
100	231.5	-95.22	231.5	-95.54	0.32

Similar to the result for the outer race fault, the inner race fault components showed lower magnitudes than their counterparts in the instantaneous power spectrum, as well as producing its clearest signal at 50% load. The no-load and full load fault components at -97.11dB and -95.54dB also appear close to the noise floor, thus resulting in small amplitude differences between the healthy and faulty components. As such, the results for the inner race fault using the square of the current are largely inconclusive.

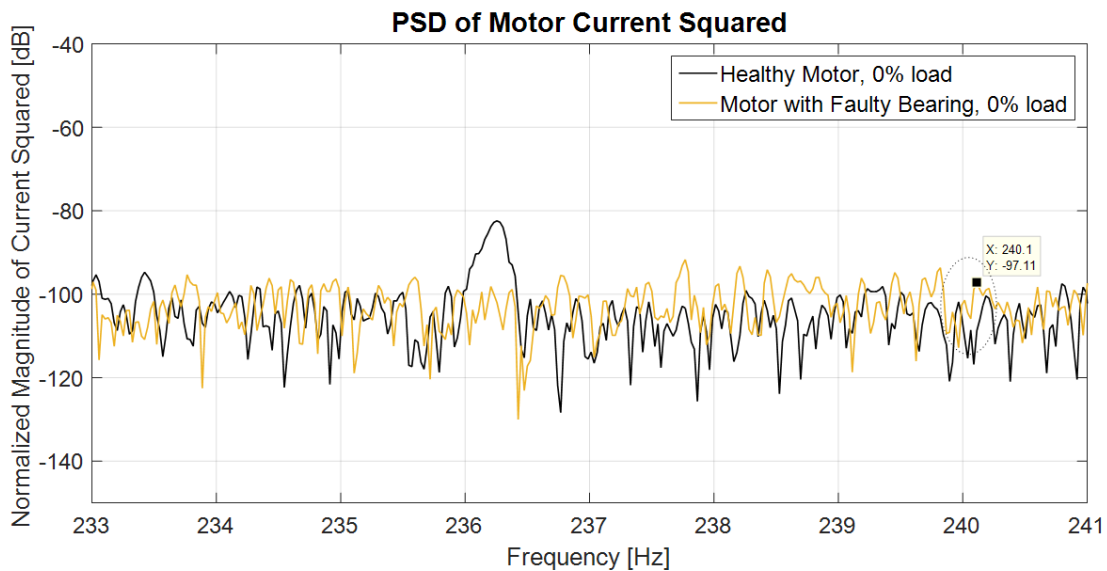


Figure 5-30: PSD of the motor current squared showing the anticipated position of the inner race fault component.

5.11.3 Effects of the inverter on bearing fault detection using MSCSA

Using the data for the inverter driven motor with faulty bearings, the square current analysis produced inconclusive results, similar to those of the instantaneous power. The spectra of the square current suffer from similar noisiness, thus making fault detection unreliable. Figure 5-31 below shows these effects around the area where the outer race fault is expected.

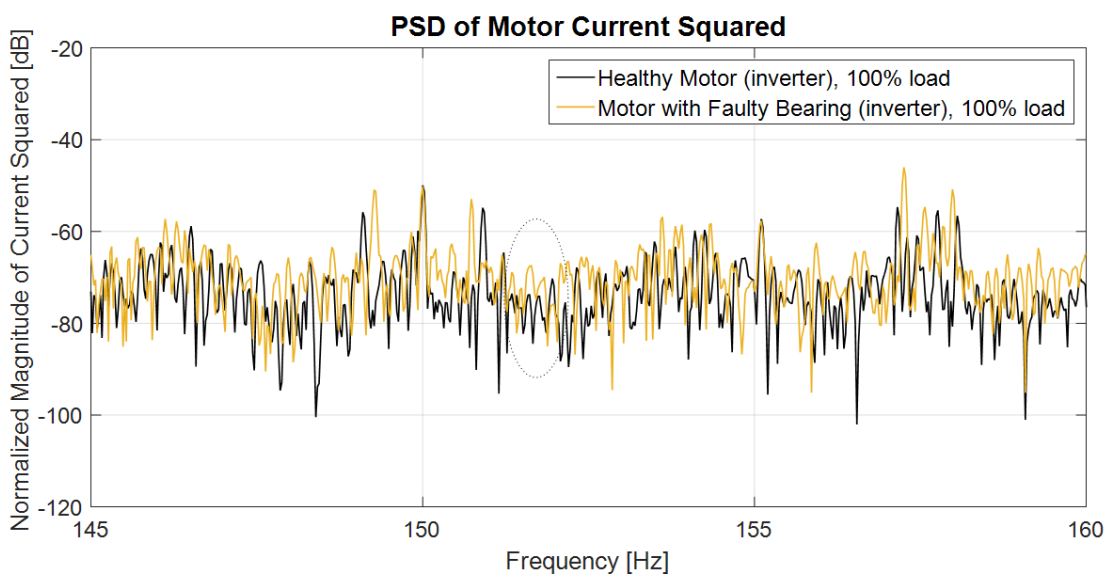


Figure 5-31: PSD of motor square current showing expected location of the outer race fault for the inverter driven motor at full load.

5.11.4 Bearing Fault Detection Summary

The results from the three analysis techniques were presented in this section on the data from the test motor with the faulty bearing. The first technique analysed the stator phase current and both the inner and outer fault components were successfully detected at all loads in the grid connected case. Results were only obtained at full load for the inverter driven motor when using current analysis.

Applying spectral techniques to the partial instantaneous power drawn by the motor for the detection of bearing faults produced less reliable results than using the current only, which is largely due to the noisiness associated with the power signal.

Using the square of the motor current, it was inferred that the bearing related disturbances would appear directly on the spectrum at the mechanical fault frequency, due to its similarity with the instantaneous power. The results from these tests proved largely inconclusive.

5.12 Summary of Results

In Table 5-34 below, a qualitative summary of results is presented. The unique aspects as well as shortcomings of each technique as applied to the three faults are also summarized:

Table 5-34: Summary of results for the three fault detection techniques as applied to stator, rotor bar and bearing faults.

	MCSA	IPSA	MSCSA
Stator fault	<ul style="list-style-type: none"> - Faults detected at all loads and reduced fault severity. - Marginal results with inverter drive. 	<ul style="list-style-type: none"> - Unique fault frequency. - Fault characteristic detected at all loads and at full severity. - Poor results at low fault severity or with inverter drive. 	<ul style="list-style-type: none"> - Unique fault frequency. - Fault characteristic detected at all loads and at full severity. - Poor results at low fault severity or with inverter drive.
Broken rotor bar fault	<ul style="list-style-type: none"> - Faults detected at all loads with grid and inverter drive. 	<ul style="list-style-type: none"> - Three unique fault frequencies. - Faults detected at all loads with grid and inverter drive. 	<ul style="list-style-type: none"> - Three unique fault frequencies. - Faults detected at all loads with grid and inverter drive.
Bearing fault	<ul style="list-style-type: none"> - Outer and inner race faults detected at all loads with grid connection. - Limited results when using inverter drive. 	<ul style="list-style-type: none"> - Outer and inner race faults detected at all loads with grid connection. - No results when using inverter drive. - Higher noise levels, hence lower confidence in results. 	<ul style="list-style-type: none"> - Outer and inner race faults only detected under some loads with grid connection. - No conclusive results when using inverter drive. - Higher noise levels, hence lower confidence in results. - Lower amplitude differences than IPSA.

6 Conclusions and Recommendations

6.1 Conclusions

In this dissertation, the common faults that afflict induction motors were studied using three different spectral analysis techniques. After reviewing the literature on the field of condition monitoring and developing an experimental methodology, tests were conducted on motors with stator, rotor cage and bearing faults. All the tests were conducted in steady state, using either grid or inverter supplies. The induction motor was loaded in two ways to various levels, while fault severity was varied (in the case of the stator fault) to investigate the effects on the fault characteristics.

The first fault investigated was that of an induction motor with inter-turn fault. The three analysis techniques were applied to the recorded data. Using Motor Current Signature Analysis, the inter turn faults were successfully detected under all test loads and severities, the exception being the inverter driven case where the inter-turn fault could only be detected at full load and maximum severity.

Analysis of the same data set using IPSA and MSCSA resulted in unique frequencies to evaluate when compared to MCSA. The inter-turn faults were successfully detected at all loads and maximum fault severity using the first fault component frequency despite the spectra being noisier than the current spectra. However, the results show significantly smaller amplitude changes when compared to classical MCSA. At reduced fault severity or when the motor was inverter driven, IPSA and MSCSA performed poorly. Using MSCSA, the second fault component frequency produced inconclusive results and its applicability to instantaneous power spectra could not be ascertained conclusively. Based on the findings from this study, it can be concluded that classical MCSA proved to be a robust and sensitive technique for stator fault detection in grid connected motors but proved less capable when the motor was inverter driven. The IPSA and MSCSA techniques produced satisfactory results under certain circumstances, and as such should be used with caution as a secondary technique to MCSA.

The second fault investigated was that of a motor with three broken rotor bars. Using MCSA, the broken rotor bar fault was conclusively detected, at all motor loads, including when the motor was inverter driven. The data was subsequently processed using the IPSA and MSCSA techniques which both used the same fault component equations. The latter techniques

introduced new fault component frequencies at twice the line frequency and at twice the slip frequency. At these unique points in the spectra, the broken rotor bar faults were conclusively detected at all loads using grid and inverter supplies. Hence, based on the results, the tested techniques proved equally reliable in detecting the broken rotor bar condition, with square current analysis requiring no extra measurements and minimal extra computational effort. Similar results were reported by Pires *et al.* [71] [73] when comparing MCSA and MSCSA in the detection of broken rotor bar faults.

The final fault investigated was that of the motor with an inner and outer race fault. Current analysis of the data proved successful in detecting both faults at all tested loads in the grid connected motor. In the inverter driven case the bearing faults could only be detected at full load. When the instantaneous power spectrum was analysed in the vicinity of the estimated disturbance frequencies, the fault component for the inner and outer race fault were detected but were located closer to the noise floor than in the case of the current spectra. This reduces confidence in the technique and the results for bearing fault detection and relegates it to being a secondary technique better used for verification. The inference that the square current spectra would behave similarly to the instantaneous power spectra with respect to bearing faults could not be proven conclusively in this study, as only the data at 50% load produced a meaningful result.

The three spectral analysis techniques of MCSA, IPSA and MSCSA applied across the three fault scenarios showed that no single technique is able to detect motor faults under all circumstances typically encountered by motors in industry. The MCSA technique proved the most capable of the three techniques as it was able to detect faults under most conditions, but generally suffered poor results in inverter driven motor applications. The IPSA and MSCSA techniques performed selectively when compared to MCSA and were relatively successful when detecting the mechanical faults. The fact that the former techniques produce results at unique points in the spectrum would suggest that they are more suitable for verifying results.

As part of a comprehensive condition monitoring scheme, as required by a large population of the motors on a nuclear power station, the three techniques presented in this study could readily be incorporated into the Condition Based Maintenance framework. The findings of the study suggest that the classical MCSA can readily be applied to grid connected motors in the Trendable Maintenance Tier to reliably detect the commonly encountered electrical and

mechanical faults. The selective strengths of IPSA and MSCSA can also be implemented in such a manner that the strengths of each technique are uniquely exploited. An example being that in the case of a motor with suspected broken rotor bars in a radiologically sensitive area, the results of MCSA can easily be confirmed by examining the unique frequency components of the square of the current with no extra measurements and minimal extra computational effort. Similarly, with bearing faults, IPSA can be used to verify the results obtained from MCSA.

6.2 Recommendations

In light of the conclusions presented, recommendations can be made for further avenues of investigation. The instantaneous power and square current techniques offer some advantages over traditional current analysis, but suffer from noisy spectra. A recommendation to further improve the results of this study would be to apply additional filtering to the data to reduce the noise level. In [28] the application of a Wiener filter is suggested to reduce the dynamics of the power supply and thereby accentuate the mechanical frequencies. This would then facilitate an interesting comparison between actual vibration and filtered instantaneous power as the fault frequencies would appear directly in both spectra. Further study could also be directed at furthering the theoretical framework for stator faults and bearing faults as they would manifest in the instantaneous power and square current spectra respectively.

7 List of References

- [1] S. Nandi, H. A. Toliyat and X. Li, "Condition Monitoring and Fault Diagnosis of Electrical Motors," *IEEE TRANSACTIONS OF ENERGY CONVERSION*, vol. 20, no. 4, pp. 719-720, 2005.
- [2] IEEE Motor Reliability Working Group, "Report of Large Motor Reliability Survey of Industrial and Commercial Installations, Part II," *IEEE transactions on industry applications*, Vols. 1A-21, no. 4, pp. 865-872, 1985.
- [3] Eskom Generation, *Reactor Coolant System (RCP) Part 3 - Reactor Coolant Pumps*, 2013.
- [4] EPRI, "Electric Motor Tiered Maintenance Program," EPRI, 2002.
- [5] IAEA - International Atomic Energy Agency, "Implementation Strategies and Tools for Condition Based Maintenance at Nuclear Power Plants," IAEA, Vienna, 2007.
- [6] EPRI, "Electric Motor Predictive and Preventive," EPRI, 1992.
- [7] N. Tandon, G. Yadava and K. Ramakrishna, "A comparison of some condition monitoring techniques for the detection of defect in induction motor ball bearings," *Science Direct - Mechanical Systems and Signal Processing*, vol. 21, p. 244–256, 2007.
- [8] B. Corne, B. Vervisch, C. Debruyne, J. Knockaert and J. Desmet, "Comparing MCSA with Vibration Analysis in order to detect Bearing Faults - A Case Study," IEEE, Belgium, 2015.
- [9] P. C. Senn, *Principles of Electric Machines and Power Electronics*, John Wiley and Sons, 1996.
- [10] J. James L. Kirtley, H. W. Beaty, N. K. Ghai, S. B. Leeb and R. H. Lyon, *Electric Motor Handbook*, McGraw-Hill Professional, 1998.
- [11] R. K. Rajput, *Electrical Machines*, 2006: Firewall Media.
- [12] S. Karmakar, S. Chattopadhyay, M. Mitra and S. Sengupta, *Induction Motor Fault Diagnosis*, Springer, 2016.
- [13] N. Mohan, T. Undeland and W. Robins, *Power Electronics*, Wiley, 2003.
- [14] G. Singh, S. Kazzaz and S. A. Ahmed, "Induction machine drive condition monitoring and diagnostic," *Elsevier - Electric Power Systems Research 64 (2003)*, vol. 64, pp. 145-158,

2003.

- [15] P. Albrecht, J. Appiarius and D. K. Sharma, ASSESSMENT OF RELIABILITY OF MOTORS IN UTILITY APPLICATIONS - UPDATED, EPRI /IEEE, 1986.
- [16] M. E. H. Benbouzid, "A Review of Induction Motors Signature Analysis as a Medium for Faults Detection," *IEEE TRANSACTIONS ON INDUSTRIAL ELECTRONICS*, vol. 47, no. 5, pp. 984-993, 2000.
- [17] M. Irfan, N. Saad, R. Ibrahim, V. S. Asirvadam, M. Magzoub and N. Hung, "An Approach to Diagnose Inner Race Surface Roughness Defects in Bearing of Induction Motors," in *IEEE International Conference on Signal and Image Processing Applications (ICSIPA)*, 2015.
- [18] R. J. G. William T. Thompson, "MOTOR CURRENT SIGNATURE ANALYSIS IN INDUCTION MOTOR DRIVES - FUNDAMENTALS, DATA INTERPRETATION AND INDUSTRIAL CASE HISTORIES," in *PROCEEDINGS OF THE THIRTY SECOND TURBOMACHINERY SYMPOSIUM*, 2003.
- [19] H. Behbahanifard, H. Karshenas and A. Sadoughi, "Non-invasive On-line Detection of Winding Faults in Induction Motors –A Review," in *2008 International Conference on Condition Monitoring and Diagnosis*, Beijing, China, April 21-24, 2008.
- [20] M. Drif and A. J. M. Cardoso, "The Use of the Instantaneous-Reactive-Power Signature Analysis for Rotor-Cage-Fault Diagnostics in Three-Phase Induction Motors," *IEEE TRANSACTIONS ON INDUSTRIAL ELECTRONICS*, vol. 56, no. 11, pp. 4606-4614, 2009.
- [21] A. BREDIMAS and W. J. NUTTALL, "A Comparison of International Regulatory Organizations and Licensing Procedures for New Nuclear Power Plants".
- [22] IAEA, "The International Atomic Energy Agency," [Online]. Available: <https://www.iaea.org/about>. [Accessed 02 February 2018].
- [23] DEPARTMENT OF MINERALS AND ENERGY, "NATIONAL NUCLEAR REGULATOR ACT, 1999 (ACT NO. 47 OF 1999)," 28 04 2006. [Online]. Available: <http://www.nnr.co.za/acts-regulations/regulations-and-government-notices/>. [Accessed 02 February 2018].
- [24] SpectraQuest, Inc., *Applied Vibration Analysis Training Manual & Laboratory Exercises*, SpectraQuest, Inc..
- [25] J. L. Taylor, *The Vibration Analysis Handbook*.

- [26] I. S. Organisation, "Mechanical vibration — Measurement and evaluation of machine vibration, Part 1: General guidelines," ISO, 2016.
- [27] H. Su and K. T. Chong, "Induction Machine Condition Monitoring Using Neural Network Modeling," *IEEE TRANSACTIONS ON INDUSTRIAL ELECTRONICS*, vol. 54, no. 1, pp. 241-249, 2007.
- [28] A. Ibrahim, M. E. Badaoui, F. Guillet and F. Bonnardot, "A New Bearing Fault Detection Method in Induction Machines Based on Instantaneous Power Factor," *IEEE TRANSACTIONS ON INDUSTRIAL ELECTRONICS*, vol. 55, no. 12, pp. 4252-4259, 2008.
- [29] I. Sadeghi, H. Ehya, J. Faiz and H. Ostovar, "Online Fault Diagnosis of Large Electrical Machines using Vibration Signal-A Review," IEEE, 2017.
- [30] D. Wang, K.-L. Tsui and Q. Miao, "Prognostics and Health Management: A Review of Vibration based Bearing and Gear Health," IEEE, 2017.
- [31] S. Bagavathiappan, B. Lahiri, T. Saravanan, J. Philip and T. Jayakumar, "Infrared thermography for condition monitoring – A review," *Infrared Physics & Technology*, vol. 60, pp. 35-55, 2013.
- [32] P. Redón, M. J. Picazo-Ródenas and J. Antonino-Daviu, "Processing tool for failure diagnosis based on isothermal representation for infrared-based fault detection in induction motors under transient state," IEEE, 2017.
- [33] D. Lopez-Perez and J. Antonino-Daviu, "Application of Infrared Thermography to Failure Detection in Industrial Induction Motors: Case Stories," *IEEE TRANSACTIONS ON INDUSTRY APPLICATIONS, VOL. 53, NO. 3, MAY/JUNE 2017*, vol. 53, no. 3, pp. 1901-1908, 2017.
- [34] R. Lewak, *Infrared Methodology and Technology*, Gordon and Breach Science Publishers, 1992.
- [35] David Gleaton, U. S. Department of Energy, "Infrared Thermography at the Savannah River Site," [Online]. Available: <<http://www.osti.gov/bridge>>.. [Accessed 29 12 2017].
- [36] P. Ewert, "Use of Axial Flux in the Detection of Electrical Faults in Induction Motors," Wrocław University of Science and Technology, Wrocław, Poland, 2017.
- [37] J. Penman, H. G. Sedding, B. A. Lloyd and W. T. Fink, "Detection and location of interturn short circuits in the stator windings of operating motors," *IEEE Trans. Energy Conversion*, vol. 9, p. 652-658, 1994.

- [38] C. Jiang, S. Li and T. G. Habetler, "A Review of Condition Monitoring of Induction Motors Based on Stray Flux," *IEEE*, 2017.
- [39] S. Zhang, Q. Cheng, Q. Zhang, W. Chen and L. Zhang, "Fault Detection of Motor Bearing with Embedded coils and PCA Algorithm," in *Proceedings of the 36th Chinese Control Conference*, Dalian, China, 2017.
- [40] N. Tandon and A. Choudhury, "A review of vibration and acoustic measurement methods for the detection of defects in rolling element bearings," *Tribology International*, vol. 32, p. 469–480, 1999.
- [41] W. LI and C. K. MECHEFSKE, "Detection of Induction Motor Faults: A Comparison of Stator Current, Vibration and Acoustic Methods," *SAGE - Journal of Vibration and Control*, vol. 12, no. 2, p. 165–188, 2006.
- [42] T. N and N. BC, "The application of the sound intensity technique to defect detection in rolling element bearings," *Applied Acoustics*, vol. 29, no. 3, 1990.
- [43] P. V. J. Rodriguez, M. Negrea and A. Arkkio, "A simplified scheme for induction motor condition monitoring," *Science Direct - Mechanical Systems and Signal Processing*, vol. 22, p. 1216–1236, 2008.
- [44] X. Liang and K. Edomwandekhoe, "Condition Monitoring Techniques for Induction Motors," in *IEEE - PSEC*, 2017.
- [45] A. J. M. Cordosa and E. S. Saraiva, "Computer-Aided Detection of Airgap Eccentricity in Operating Three-phase Induction Motors by Park's Vector Approach," *IEEE TRANSACTIONS ON INDUSTRY APPLICATIONS*, vol. 29, no. 5, pp. 897-901, 1993.
- [46] A. J. M. Cardoso, S. M. A. Cruz, J. F. S. Carvalho and E. S. Saraiva., "Rotor Cage Fault Diagnosis in Three-phase Induction Motors by Park's Vector Approach," *IEEE*, Coimbra, Portugal, 1995.
- [47] H. Nejari and M. E. H. Benbouzid, "Monitoring and Diagnosis of Induction Motors Electrical Faults Using a Current Park's Vector Pattern Learning Approach," *IEEE TRANSACTIONS ON INDUSTRY APPLICATIONS*, vol. 36, no. 3, pp. 730-735, MAY/JUNE 2000.
- [48] S. M. A. Cruz and A. J. M. Cardoso, "Stator Winding Fault Diagnosis in Three-Phase Synchronous and Asynchronous Motors, by the Extended Park's Vector Approach," *IEEE TRANSACTIONS ON INDUSTRY APPLICATIONS*, pp. 1227-1233, SEPTEMBER/OCTOBER 2001.

- [49] S. M. A. Cruz and A. J. M. Cardoso, "Rotor cage fault diagnosis in three-phase induction motors by Extended Park's Vector Approach," *Electrical and Mechanical Power Systems*, vol. 28, no. 4, pp. 289-299, 2000.
- [50] J. L. H. Silva and A. J. M. Cardoso, "Bearing Failures Diagnosis in Three-Phase Induction Motors by Extended Park's Vector Approach," IEEE, Coimbra, Portugal, 2005.
- [51] J. M. MENDEL, "Tutorial on Higher-Order Statistics (Spectra) in Signal Processing and System Theory: Theoretical Results and Some Applications," *PROCEEDINGS OF THE IEEE*, vol. 19, no. 3, pp. 278-305, MARCH 1991.
- [52] D. Z. Li, W. Wang and F. Ismail, "An Enhanced Bispectrum Technique With Auxiliary Frequency Injection for Induction Motor Health Condition Monitoring," *IEEE TRANSACTIONS ON INSTRUMENTATION AND MEASUREMENT*, vol. 64, no. 10, pp. 2679-22687, OCTOBER 2015.
- [53] J. P. Neil Arthur, "Induction Machine Condition Monitoring with Higher Order Spectra," *IEEE TRANSACTIONS ON INDUSTRIAL ELECTRONICS*, vol. 47, no. 5, pp. 1031-1041, OCTOBER 2000.
- [54] T. W. S. Chow, "CONDITION MONITORING OF ELECTRIC MACHINES USING THIRD-ORDER SPECTRUM ANALYSIS," IEEE, 1996.
- [55] A. H. Boudinar, N. Benouzza, A. Bendiabdellah and M.-E.-A. Khodja, "Induction Motor Bearing Fault Analysis Using a Root-MUSIC Method," *IEEE TRANSACTIONS ON INDUSTRY APPLICATIONS, VOL. 52, NO. 5,* vol. 52, no. 5, pp. 3851-3860, SEPTEMBER/OCTOBER 2016.
- [56] A. Garcia-Perez, R. J. Romero-Troncoso, E. Cabal-Yepez, R. A. Osornio-Rios, J. d. J. Rangel-Magdaleno and H. Miranda, "Startup Current Analysis of Incipient Broken Rotor Bar in Induction Motors using High-Resolution Spectral Analysis," IEEE, 2011.
- [57] D. Morinigo-Sotelo, R. J. Romero-Troncoso, J. A. Antonino-Daviu and K. N. Gyftakis, "Reliable Detection of Broken Rotor Bars in Induction Motors via MUSIC and ZSC Methods," IEEE, 2016.
- [58] M. V. C. T. Mohamed El Hachemi Benbouzid, "Induction Motors' Faults Detection and Localization Using Stator Current Advanced Signal Processing Techniques," *IEEE TRANSACTIONS ON POWER ELECTRONICS*, vol. 14, no. 1, pp. 14-22, JANUARY 1999.
- [59] H. Douglas, P. Pillay and A. K. Ziarani, "A New Algorithm for Transient Motor Current Signature Analysis Using Wavelets," *IEEE TRANSACTIONS ON INDUSTRY APPLICATIONS*, vol. 40, no. 5, pp. 1361-1368, SEPTEMBER/OCTOBER 2004.

- [60] A. W. Galli, G. T. Heydt and F. Ribeiro, "Exploring the Power of Wavelet Analysis," *IEEE Comput. Appl. Power*, vol. 9, p. 37–41, Oct. 1996.
- [61] Z. Ye, B. Wu and A. Sadeghian, "Current Signature Analysis of Induction Motor Mechanical Faults by Wavelet Packet Decomposition," *IEEE TRANSACTIONS ON INDUSTRIAL ELECTRONICS*, vol. 50, no. 6, pp. 1217-1228, DECEMBER 2003.
- [62] A. Bouzida, O. Touhami, R. Ibtouen, A. Belouchrani, M. Fadel and A. Rezzoug, "Fault Diagnosis in Industrial Induction Machines Through Discrete Wavelet Transform," *IEEE TRANSACTIONS ON INDUSTRIAL ELECTRONICS*, vol. 58, no. 9, pp. 4385-4395, SEPTEMBER 2011.
- [63] J. Cusidó, L. Romeral, J. A. Ortega, J. A. Rosero and A. G. Espinosa, "Fault Detection in Induction Machines Using Power Spectral Density in Wavelet Decomposition," *IEEE TRANSACTIONS ON INDUSTRIAL ELECTRONICS*, VOL. 55, NO. 2, *IEEE TRANSACTIONS ON INDUSTRIAL ELECTRONICS*, vol. 55, no. 2, pp. 633-643, FEBRUARY 2008.
- [64] P. S. Barendse, B. Herndler, M. A. Khan and P. Pillay, "The Application of Wavelets for the Detection of Inter-Turn Faults in Induction Machines," IEEE, 2009.
- [65] J. Zarei and S. Yousefizadeh, "Fault Detection in Induction Motors using Park's Vector Approach and Wavelet Analysis," in *2014 International Conference on Mechatronics and Control (ICMC)*, Jinzhou, China, July 3 - 5, 2014.
- [66] L. Eren and M. J. Devaney, "Bearing Damage Detection via Wavelet Packet Decomposition of the Stator Current," *IEEE TRANSACTIONS ON INSTRUMENTATION AND MEASUREMENT*, vol. 53, no. 2, pp. 431-436, APRIL 2004.
- [67] S. F. Legowski, A. H. M. S. Ula and A. M. Trzynadlowsh, "Instantaneous power as a medium for the signature analysis of induction motors," *IEEE Trans. Ind, Applicat.*, vol. 32, pp., vol. 32, p. 904–909, July/Aug. 1996..
- [68] A. M. Trzynadlowski and S. F. Legowski, "Diagnostics of Mechanical Abnormalities in Induction Motors Using Instantaneous Electric Power," *IEEE Transactions on Energy Conversion*, vol. 14, no. 4, p. 1417, December 1999.
- [69] A. O. D. Tommaso, R. Miceli and G. R. Galluzzo, "Monitoring and Diagnosis of Failures in Squirrel-Cage Induction Motors Due to Cracked or Broken Bars," IEEE, 2011.
- [70] M. Drif and A. J. M. Cardoso, "Stator Fault Diagnostics in Squirrel Cage Three-Phase Induction Motor Drives Using the Instantaneous Active and Reactive Power Signature Analyses," *IEEE TRANSACTIONS ON INDUSTRIAL INFORMATICS*, vol. 10, no. 2, pp. 1348-

1360, May 2014.

- [71] V. F. Pires, M. Kadivonga, J. Martins and A. Pires, "Motor square current signature analysis for induction motor rotor diagnosis," *Elsevier - Measurement*, vol. 46, p. 942–948, 2013.
- [72] V. F. Pires, D. Foito, J. F. Martins and A. J. Pires, "Detection of Stator Winding Fault in Induction Motors Using a Motor Square Current Signature Analysis (MSCSA)," in *IEEE Internatinal Conference on Power Engineering, Energy and Electrical Drives*, 2015.
- [73] V. F. Pires, J. F. Martins, A. J. Pires and L. Rodrigues, "Induction Motor Fault Detection Based on MCSA, MSCSA and PCA: A Comparitive Study," *IEEE*, 2016.
- [74] A. S. Fontes, C. A. V. Cardoso and L. P. B. Oliveira, "Comparison of techniques based on current signature analysis to fault detection and diagnosis in induction electrical motors," *IEEE*, 2016.
- [75] A. Gandhi, T. Corrigan and L. Parsa, "Recent Advances in Modeling and Online Detection of Stator Interturn Faults in Electrical Motors," *IEEE TRANSACTIONS ON INDUSTRIAL ELECTRONICS, VOL. 58, NO. 5,* vol. 58, no. 5, pp. 1564-1575, 2011.
- [76] A. K. Jain, J. Mao and K. M. Mohiuddin, "Artificial Neural Networks: A Tutorial," *IEEE*, 1996.
- [77] M. J. Devaney and L. Eren, "Detecting Motor Bearing Faults," *IEEE Instrumentation & Measurement Magazine*, 2004.
- [78] J. F. Martins, V. F. Pires and A. J. Pires, "Unsupervised Neural-Network-Based Algorithm for an On-Line Diagnosis of Three-Phase Induction Motor Stator Fault," *IEEE TRANSACTIONS ON INDUSTRIAL ELECTRONICS*, vol. 54, no. 1, pp. 259-264, FEBRUARY 2007.
- [79] R. R. Schoen, B. K. Lin, T. G. Habaetler, J. H. Schlag and S. Farag, "An Unsupervised, On-line System for Induction Motor Fault Detection Using Stator Current Monitoring," *IEEE TRANSACTIONS ON INDUSTRY APPLICATIONS*, vol. 31, no. 6, pp. 1280-1286, 1995.
- [80] M. S. Ballal, Z. J. Khan, H. M. Suryawanshi and R. L. Sonolikar, "Adaptive Neural Fuzzy Inference System for the Detection of Inter-Turn Insulation and Bearing Wear Faults in Induction Motor," *IEEE TRANSACTIONS ON INDUSTRIAL ELECTRONICS*, vol. 54, no. 1, pp. 250-258, 2007.
- [81] A. Sadeghian, Z. Ye and B. Wu, "Online Detection of Broken Rotor Bars in Induction Motors by Wavelet Packet Decomposition and Artificial Neural Networks," *IEEE TRANSACTIONS ON INSTRUMENTATION AND MEASUREMENT*, vol. 58, no. 7, pp. 2253-

2263, 2009.

- [82] Z. Liu, X. Yin, Z. Zhang, D. Chen and W. Chen, "Online Rotor Mixed Fault Diagnosis Way Based on Spectrum Analysis of Instantaneous Power in Squirrel Cage Induction Motors," *IEEE TRANSACTIONS ON ENERGY CONVERSION*, vol. 19, no. 3, p. 485, SEPTEMBER 2004.
- [83] W. T. Thomn, "ON-LINE MCSA TO DIAGNOSE SHORTED TURNS IN LOW VOLTAGE STATOR WINDINGS OF 3-PHASE INDUCTION MOTORS PRIOR TO FAILURE," IEEE, Aberdeen Scotland, 2001.
- [84] BSI Standards Publication, "BS ISO 20958:2013 - Condition monitoring and diagnostics of machine systems — Electrical signature analysis of three-phase induction motors," BSI/ISO, 2013.
- [85] J. Kim, S. Shin, S. B. Lee, K. N. Gyftakis, M. Drif and A. J. M. Cardoso, "Power Spectrum-Based Detection of Induction Motor Rotor Faults for Immunity to False Alarms," *IEEE TRANSACTIONS ON ENERGY CONVERSION*, vol. 30, no. 3, pp. 1123-1132, SEPTEMBER 2015.
- [86] R. R. Schoen, T. G. Habetler, F. Kamran and R. G. Bartheld, "Motor Bearing Damage Detection Using Stator Current Monitoring," *IEEE TRANSACTIONS ON INDUSTRY APPLICATIONS*, vol. 31, no. 6, pp. 1274 - 1279, NOVEMBER/ DECEMBER 1995.
- [87] G. B. K. Mohamed El Hachemi Benbouzid, "What Stator Current Processing-Based Technique to Use for Induction Motor Rotor Faults Diagnosis?," *IEEE TRANSACTIONS ON ENERGY CONVERSION*, VOL. 18, NO. 2,X, vol. 18, no. 2, pp. 238-244, JUNE 2003.
- [88] "Mathworks," Mathworks, [Online]. Available: <http://www.mathworks.com/help/images/fourier-transform.html>. [Accessed 12 01 2018].
- [89] S. R. Kulkarni.. [Online]. Available: https://www.princeton.edu/~cuff/ele201/kulkarni_text/frequency.pdf. [Accessed 12 January 2018].
- [90] E. O. Brigham and R. E. Morrow, "The fast Fourier transform," *IEEE spectrum*, pp. 63-70, DECEMBER 1967.
- [91] R. d. J. Romero-Troncoso, "Multirate Signal Processing to Improve FFT-Based Analysis for Detecting Faults in Induction Motors," *IEEE TRANSACTIONS ON INDUSTRIAL INFORMATICS*, VOL. 13, NO. 3, JUNE 2017 *IEEE TRANSACTIONS ON INDUSTRIAL INFORMATICS*, vol. 13, no. 3, pp. 1291-1300, JUNE 2017.
- [92] LDS Dactron, "LDS Dactron," [Online]. Available:

users.utcluj.ro/~elupu/Curs/fileloader.php?fileName=upload/...de.../FFT_window....
[Accessed 12 January 2018].

- [93] S. M. KAY and J. STANLEY LAWRENCE MARPLE, "Spectrum Analysis-A Modern Perspective," *PROCEEDINGS OF THE IEEE*, vol. 69, no. 11, pp. 1380-1418, NOVEMBER 1981.

- [94] M. Dlamini, "DEVELOPMENT OF AN INDUCTION MOTOR CONDITION MONITORING TEST RIG AND FAULT DETECTION STRATEGIES," University of Cape Town, Cape Town, 2014.

- [95] National Instruments, "NI 9215 Datasheet," National Instruments.

- [96] SpectraQuest Inc, "User Operating Manual for Machinery Fault Simulator," SpectraQuest Inc.

- [97] Delta Electronics Inc., "ASDA-A2 series User Manual," Delta Electronics Inc..

8 Appendices

Appendix A – Hardware and Software

Hardware

Inverter Drive Parameters

Table 8-1: Critical Parameters for the Lenze SMVector Inverter Drive [94].

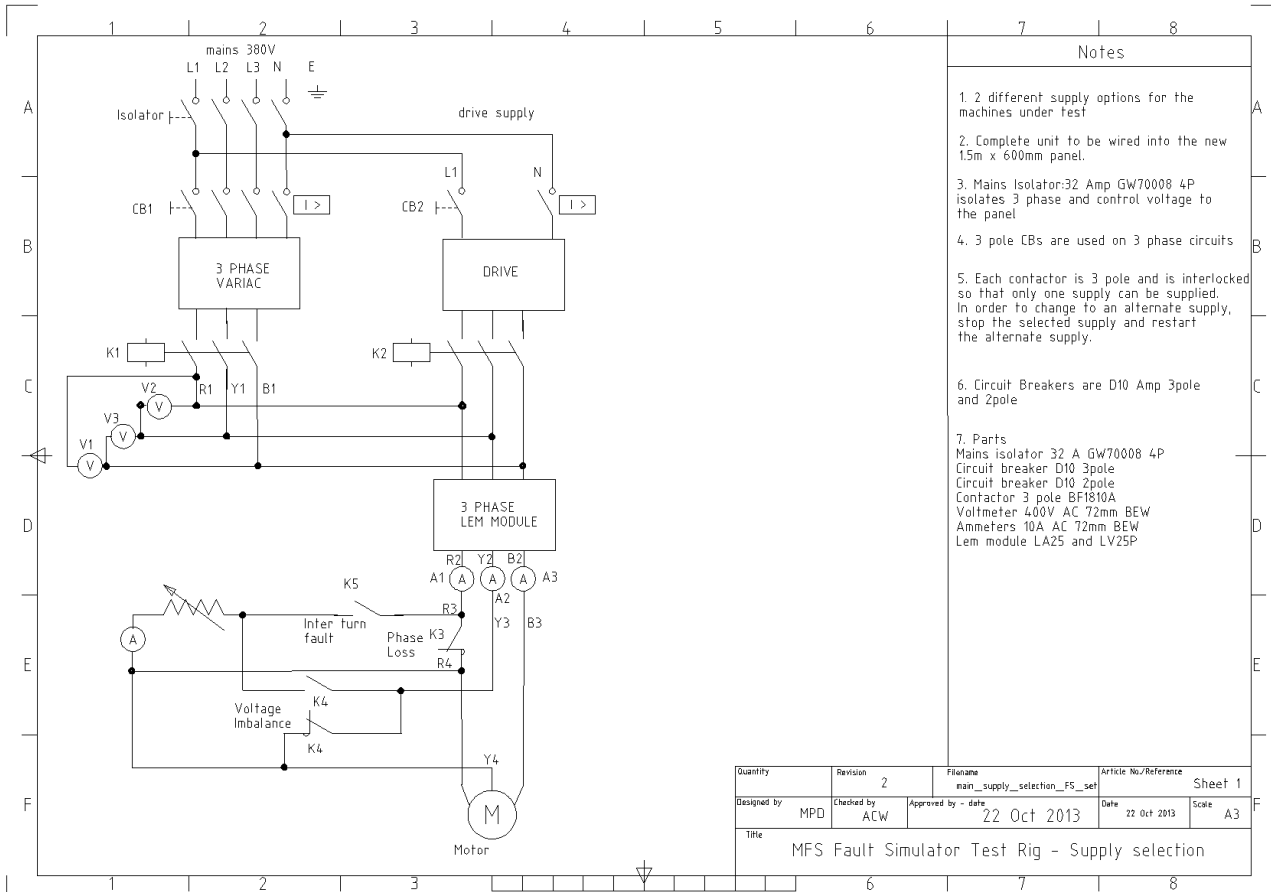
Parameter (P)	Description	Parameter setting
P100	Start source – Local keypad	0.0
P102	Minimum frequency (Hz)	0
P103	Maximum frequency (Hz)	60
P104	Acceleration time 1(s)	10.0
P106	S ramp integration time (s)- Linear ramp	0.0
P107	Line Voltage selection	01
P108	Motor overload (%)	100
P110	Start method – Normal	00
P150	TB-30 Output – Output frequency	1
P166	Carrier frequency- 6kHz	01
P300	Drive mode – Constant V/Hz	00
P302	Motor rated voltage (V)	190
P303	Motor rated current (A)	1.8
P304	Motor rated frequency (Hz)	50
P305	Motor rated speed (rpm)	2850

Servo Drive Parameters

Table 8-2: Critical parameters configured for the Delta ASDA-A2 Servo drive [94].

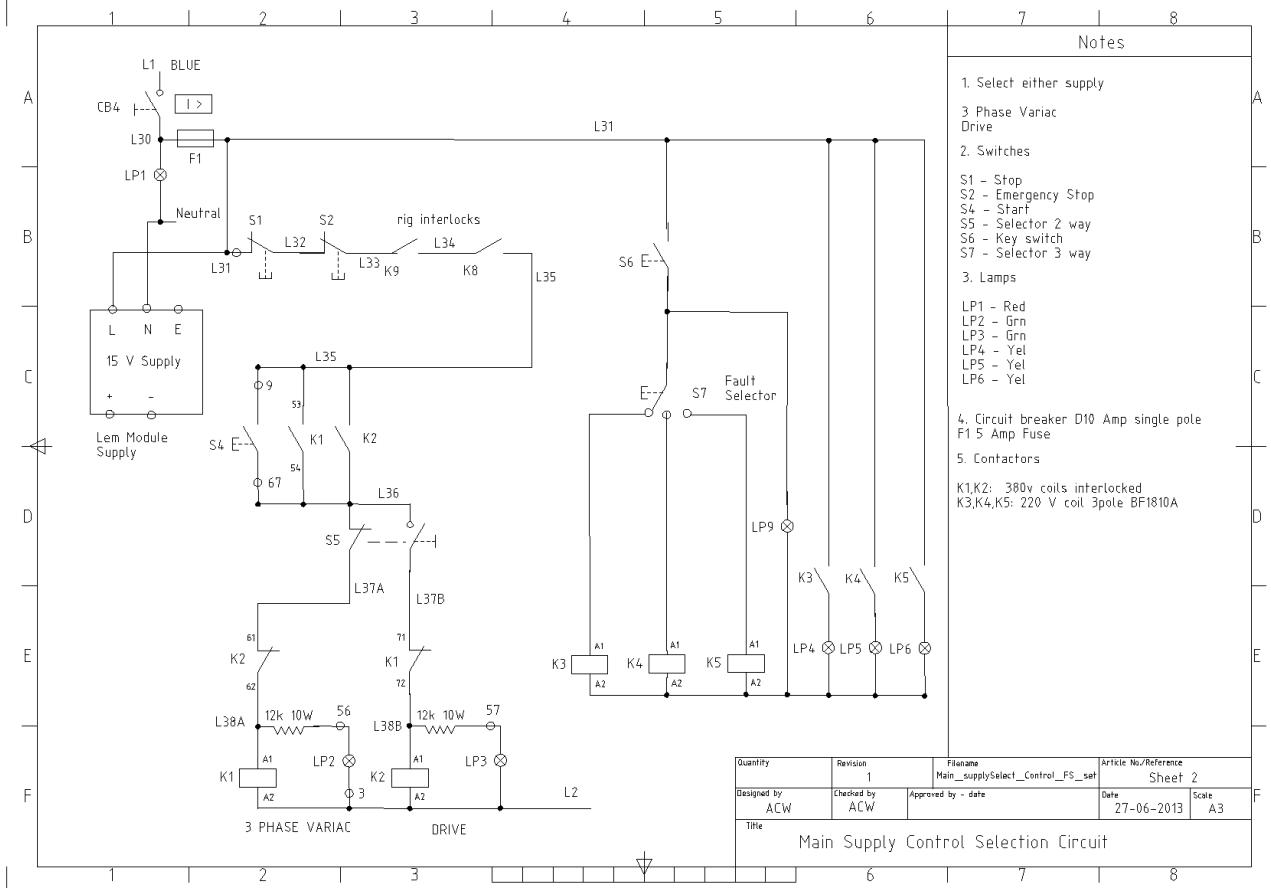
Parameter (P)	Description	Parameter setting
P1-01	Control Mode and output direction	0 x 000A
P1-02	Speed and torque limit setting	0 x 0000
P1 -04	Analogue Monitor output portion 1 (MON1)	100
P1 -05	Analogue Monitor output portion 2 (MON2)	100
P1-52	Regenerative resistor value	20
P1-53	Regenerative resistor capacity	1000
P1-72	Full-closed Loop Resolution (for CN5 terminal)	128000

Control Panel Schematics



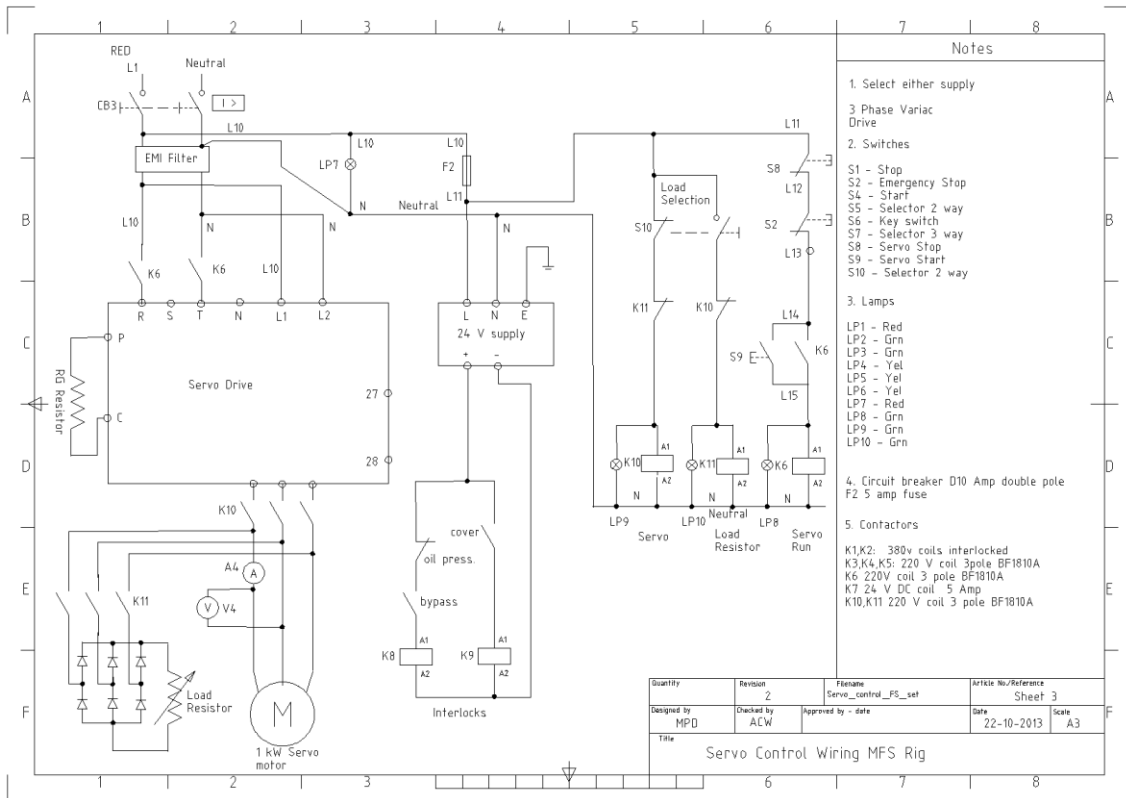
- Notes**
- 2 different supply options for the machines under test
 - Complete unit to be wired into the new 1.5m x 600mm panel.
 - Mains Isolator: 32 Amp GW70008 4P isolates 3 phase and control voltage to the panel
 - 3 pole CBs are used on 3 phase circuits
 - Each contactor is 3 pole and is interlocked so that only one supply can be supplied. In order to change to an alternate supply, stop the selected supply and restart the alternate supply.
 - Circuit Breakers are D10 Amp 3pole and 2pole
 - Parts
Mains isolator 32 A GW70008 4P
Circuit breaker D10 3pole
Circuit breaker D10 2pole
Contactor 3 pole BF1810A
Voltmeter 400V AC 72mm BEW
Ammeters 10A AC 72mm BEW
Lem module LA25 and LV25P

Quantity	Revision 2	Filename main_supply_selection_FS_set	Article No/Reference	Sheet 1
Designed by MPD	Checked by ACW	Approved by - date 22 Oct 2013	Date 22 Oct 2013	Scale A3
Title MFS Fault Simulator Test Rig - Supply selection				



- Notes**
- Select either supply
 - 3 Phase Variac
Drive
 - Switches
S1 - Stop
S2 - Emergency Stop
S4 - Start
S5 - Selector 2 way
S6 - Key switch
S7 - Selector 3 way
 - Lamps
LP1 - Red
LP2 - Grn
LP3 - Grn
LP4 - Yel
LP5 - Yel
LP6 - Yel
 - Circuit breaker D10 Amp single pole F1 5 Amp Fuse
 - Contactors
K1, K2: 380v coils interlocked
K3, K4, K5: 220 V coil 3pole BF1810A

Quantity	Revision 1	Filename Main_supplySelect_Control_FS_set	Article No/Reference	Sheet 2
Designed by ACW	Checked by ACW	Approved by - date	Date 27-06-2013	Scale A3
Title Main Supply Control Selection Circuit				




```

ia_hann_healthy = ia_healthy.*Window_rot; % multiply current vector by rotated window
vector
ia_hann_fault = ia_fault.*Window_rot; % multiply current vector by rotated window vector

NFFT = 2^nextpow2(N); % zero padding
f = (f_sampling/NFFT)*(0:NFFT/2-1); %create a frequency vector

FFT_Ia = fft(ia_hann_healthy,NFFT); % run FFT...
FFT_Ia = FFT_Ia(1:NFFT/2); % creates single sided spectrum

FFT_Ia_2 = fft(ia_hann_fault,NFFT); % run FFT...
FFT_Ia_2 = FFT_Ia_2(1:NFFT/2); % creates single sided spectrum

P_Ia = (1/NFFT) * abs(FFT_Ia).^2; % calculating power for each freq comp
P_Ia_Norm = P_Ia./max(P_Ia); % Normalizing

P_Ia_2 = (1/NFFT) * abs(FFT_Ia_2).^2; % calculating power for each freq comp
P_Ia_2_Norm = P_Ia_2./max(P_Ia_2); % Normalizing

%P_I = FFT_Ia_2.*conj(FFT_Ia_2)/NFFT;% calculates PSD (hamming)
%P_I_n = P_I./max(P_I); %normalise

% figure(1);
% plot(f(7200:9200),10*log10(P_Ia_Norm(7200:9200)),'g'); hold on,
% plot(f(7200:9200),10*log10(P_Ia_2_Norm(7200:9200)));
%
% xlabel('Frequency (Hz)')
% ylabel('Normalized Magnitude of Ia (dB)');
% title('Single Sided PSD of Ia using a Hann Window');
% %legend('Healthy Motor No load (inverter)','Motor with 4 shorted turns, 100% load
(inverter)');
% legend('Healthy Motor, no load','Motor with 4 shorted turns, no load');

figure(2);
%plot(f,10*log10(P_Ia_Norm));hold on
plot(f,10*log10(P_Ia_2_Norm));hold on

xlabel('Frequency (Hz)','FontSize',18,'FontWeight','normal');
ylabel('Normalized Magnitude of Ia (dB)','FontSize',18,'FontWeight','normal');
title('PSD of motor line current','FontSize',22,'FontWeight','bold');
%title('PSD of motor line current');
legend('Healthy Motor, 50% load','Motor with 3 broken rotor bars, 50% load');
% legend({'Healthy motor,inverter driven, 100% load','Motor with 4 shorted turns,
inverter driven, 100% load'},'FontSize',18,'FontWeight','normal');

```

Published with MATLAB® R2015a

```

%%%%%%%%%%%%%%%%%%%%%%%%%%%%%%%%%%%%%%%%%%%%%%%%%%%%%%%%%%%%%%%%%%%%%%%% IPSA and MSCSA Code %%%%%%%%%%%%%%%%%%%%%%%%%%%%%%%%%%%%%%%%%%%%%%%%%%%%%%%%%%%%%%%%%%%%%%%%%555

healthy_data = load('Healthy_motor_grid_100_load_10_20170918.txt');
%healthy_data = load('Healthy_grid_1_load_100_20171031_azile.txt');
% fault_data = load('Brokenrotor_grid_weakfield20_14_servoload_0_20171013.txt');
%fault_data = load('Healthy_motor_grid_stator_4turns_100_load_8_20170922.txt');
fault_data = load('Brokenrotor_grid_1_load_100_20171013.txt');

f_sampling = 25600; % Sampling frequency
T = 1/f_sampling; % Sampling period
N = 768000; % Number of samples
t = (0:N-1)*T; % Time Vector

ia_healthy = healthy_data(:,5); % read phase A current of healthy motor
va_healthy = healthy_data(:,2); % read phase A voltage of healthy motor
% vb_healthy = healthy_data(:,2); % read phase A voltage of healthy motor
% vline_ab_healthy = va_healthy - vb_healthy; %line voltage

ia_fault = fault_data(:,5); % read phase A current of faulted motor
va_fault = fault_data(:,2); % read phase A voltage of faulted motor
% vb_fault = fault_data(:,2); % read phase A voltage of faulted motor
% vline_ab_faulty = va_fault - vb_fault; %line voltage

pa_healthy = ia_healthy.*va_healthy;
pa_faulty = ia_fault.*va_fault;

%w = hann(N); % apply window function
Nh = 1:N; % number of windows for Hann Window
Nhr = rot90(Nh); % rotated window vector
Window(Nhr) = 0.5*(1-cos(2*pi*(Nhr)/N)); % manually perform Hann Window
Window_rot = rot90(Window); % rotate Window vector to perform multiplication
pa_hann_healthy = pa_healthy.*Window_rot; % multiply power vector by rotated window
vector
pa_hann_fault = pa_faulty.*Window_rot; % multiply power vector by rotated window vector

NFFT = 2^nextpow2(N); % zero padding
f = (f_sampling/NFFT)*(0:NFFT/2-1); %create a frequency vector

FFT_Pa = fft(pa_hann_healthy,NFFT); % run FFT...
FFT_Pa = FFT_Pa(1:NFFT/2); % creates single sided spectrum

FFT_Pa_2 = fft(pa_hann_fault,NFFT); % run FFT...
FFT_Pa_2 = FFT_Pa_2(1:NFFT/2); % creates single sided spectrum

P_Pa = (1/NFFT) * abs(FFT_Pa).^2; % calculating power for each freq comp

f_bin = find(P_Pa == max(P_Pa)) %Find the bin with the highest freq
f_max = f(f_bin) %Find the highest freq
v_max = P_Pa(f_bin) % Magnitude of this point

P_Pa_Norm = P_Pa./max(P_Pa); % Normalizing

P_Pa_2 = (1/NFFT) * abs(FFT_Pa_2).^2; % calculating power for each freq comp
P_Pa_2_Norm = P_Pa_2./max(P_Pa_2); % Normalizing

%%%% MOTOR SQUARE CURRENT CODE %%%%%%%%%

```

```

ia2_healthy = ia_healthy.^2;
ia2_fault = ia_fault.^2;

ia2_hann_healthy = ia2_healthy.*Window_rot; % multiply current^2 vector by rotated
window vector
ia2_hann_fault = ia2_fault.*Window_rot; % multiply current^2 vector by rotated window
vector

FFT_Ia2 = fft(ia2_hann_healthy,NFFT); % run FFT...
FFT_Ia2 = FFT_Ia2(1:NFFT/2); % creates single sided spectrum

FFT_Ia2_2 = fft(ia2_hann_fault,NFFT); % run FFT...
FFT_Ia2_2 = FFT_Ia2_2(1:NFFT/2); % creates single sided spectrum

P_Ia2 = (1/NFFT) * abs(FFT_Ia2).^2; % calculating power for each freq comp

f_bin2 = find(P_Ia2 == max(P_Ia2)) %Find the bin with the highest freq
f_max2 = f(f_bin2) %Find the highest freq
v_max2 = P_Ia2(f_bin2) % Magnitude of this point

P_Ia2_Norm = P_Ia2./max(P_Ia2); % Normalizing

P_Ia2_2 = (1/NFFT) * abs(FFT_Ia2_2).^2; % calculating power for each freq comp
P_Ia2_2_Norm = P_Ia2_2./max(P_Ia2_2); % Normalizing

%P_I = FFT_Ia_2.*conj(FFT_Ia_2)/NFFT;% calculates PSD (hamming)
%P_I_n = P_I./max(P_I); %normalise

% figure(1);
% plot(f(7200:9200),10*log10(P_Ia_Norm(7200:9200)), 'g'); hold on,
% plot(f(7200:9200),10*log10(P_Ia_2_Norm(7200:9200)));

% xlabel('Frequency (Hz)')
% ylabel('Normalized Magnitude of Ia (dB)');
% title('Single Sided PSD of Ia using a Hann Window');
% legend('Healthy Motor No load (inverter)', 'Motor with 4 shorted turns, 100% load
(inverter)');
% legend('Healthy Motor, no load', 'Motor with 4 shorted turns, no load');

% figure(1);
% plot(t(7200:9200),pa_healthy(7200:9200), 'g'); hold on,
% plot(t(7200:9200),pa_faulty(7200:9200));hold on,
%
% xlabel('Time (t)')
% ylabel('Instantaneous Power (W)');
% title('Instantaneous Power of Phase A');
% legend('Healthy Motor No load (inverter)', 'Motor with 4 shorted turns, 100% load
(inverter)');
% legend('Healthy Motor, 100% load', 'Motor with Broken Rotor Bars, 100% load');
%
% figure(2);
% plot(t(7200:9200),ia_healthy(7200:9200), 'g'); hold on,
% plot(t(7200:9200),ia_fault(7200:9200));hold on,
% plot(t(7200:9200),va_healthy(7200:9200), 'k'); hold on,
% plot(t(7200:9200),va_fault(7200:9200), 'r');

%
% figure(3);

```

```

% plot(f,10*log10(P_Pa_Norm)); hold on,
% plot(f,10*log10(P_Pa_2_Norm));
%
% xlabel('Frequency (Hz)')
% ylabel('Normalized Magnitude of Instantaneous Power (dB)');
% title('Single Sided PSD of Instantaneous Power using a Hann Window');
% %legend('Healthy Motor, 100% load','Motor with Broken Rotor Bars, 100% load');
% %legend('Healthy Motor, 100% Servo load','Motor with 3 broken rotor bars, 100% Servo
load');
% %legend('Healthy Motor, 100% Servo load','Motor with 3 broken rotor bars and weak
field, 100% Servo load');
%
%
% figure(4);
% plot(f,10*log10(P_Pa),'b'); hold on,
% plot(f,10*log10(P_Pa_2),'r');hold on,
% plot(f,10*log10(P_Ia2),'k'); hold on,
% plot(f,10*log10(P_Ia2_2),'y');
% %plot(f,10*log10(P_Pa),'g'); hold on,
% xlabel('Frequency (Hz)')
% ylabel('Magnitude of Current Squared (dB)');
% title('Single Sided PSD of Current Squared using a Hann Window');
% %legend('Healthy Motor, 100% load','Motor with Broken Rotor Bars, 100% load');

figure(5);
% plot(f,10*log10(P_Pa_Norm),'b'); hold on,
%plot(f,10*log10(P_Pa_2_Norm),'r');hold on,
plot(f,10*log10(P_Pa_2_Norm));hold on,

% plot(f,10*log10(P_Ia2_Norm),'k'); hold on,
% plot(f,10*log10(P_Pa_2_Norm));hold on,
grid on;

xlabel('Frequency [Hz]','FontSize',18,'FontWeight','normal');
ylabel('Normalized Magnitude of Instantaneous Power
[dB]','FontSize',18,'FontWeight','normal');
title('PSD of Motor Instantaneous Power','FontSize',22,'FontWeight','bold');
%title('PSD of Motor Squared Current');
%legend('Healthy Motor, 100% load','Motor with faulty bearing, 100% load');
legend({'Healthy motor, 0% load','Motor with 4 shorted turns, 100%
load'},'FontSize',18,'FontWeight','normal');
%legend({'Healthy motor,inverter driven, 100% load','Motor with 4 shorted turns, inverter
driven, 100% load'},'FontSize',18,'FontWeight','normal');

```

Appendix B - Results

MCSA: Inter-turn fault – 4 shorted turns

Table 8-3: Inter-turn fault components for various combinations of n and k.

Load = 100%	Healthy Motor		Faulty Motor 4 shorted turns		Result
	n = 2928.9 rpm s = 0.0239		n = 2919.6 rpm s = 0.0251		
n; k	Frequency [Hz]	Amplitude [dB]	Frequency [Hz]	Amplitude [dB]	Amplitude difference [dB]
1; 1	98.51	-73.21	98.89	-85.79	-12.58
1; 3	198.21	-75.52	199.03	-89.29	-13.77
1; 5	297.91	-82.22	299.17	-96.99	-14.77
2; 1	147.17	147.70	-74.28	-76.41	2.13
2; 3	246.87	247.84	-77.84	-76.30	-1.54
2; 5	346.57	347.98	-67.51	-69.32	1.81
3; 1	195.83	196.52	-89.98	-78.36	-11.62
3; 3	295.53	296.66	-99.28	-102.10	2.82
3; 5	395.23	396.80	-98.00	-83.10	-14.90
5; 1	293.15	294.15	-91.79	-93.31	1.52

MCSA: Inverter connected motor with inter-turn fault (4 turns)

Table 8-4: Inter-turn fault components for combinations of n and k for the inverter driven case.

	n; k	Healthy Motor		Faulty Motor		Result
		Frequency [Hz]	Amplitude [dB]	Frequency [Hz]	Amplitude [dB]	
Load = 0%		n = 2983.6 rpm s = 0.0054		n = 2983.6 rpm s = 0.0055		
	1; 1	99.73	99.73	-56.67	-61.94	5.27
	1; 3	199.73	199.73	-60.13	-62.06	1.93
	1; 5	299.73	299.73	-68.93	-75.56	6.63
Load = 100%		n = 2920.1 rpm s = 0.0266		n = 2921.9 rpm s = 0.0260		
	1; 3	198.67	-73.95	198.70	-71.16	-2.79
	1; 5	298.67	-74.42	298.70	-74.91	0.49

MCSA: Inverter connected motor with inter-turn fault (2 turns)

Table 8-5: Inter-turn fault components for combinations of n and k for the inverter driven case at reduced fault severity and full load.

Load = 100%	n; k	Healthy Motor		Faulty Motor		Result
		Frequency [Hz]	Amplitude [dB]	Frequency [Hz]	Amplitude [dB]	Amplitude difference [dB]
	1; 3	198.7	-73.95	198.7	-79.34	5.39
	1; 5	298.7	-73.82	298.7	-82.26	8.44

IPSA: Inter-turn fault – 4 shorted turns

Table 8-6: Inter-turn fault components for combinations of n and k at no-load using IPSA.

Load = 0%	Healthy Motor		Faulty Motor		Result
	Frequency [Hz]	Amplitude [dB]	Frequency [Hz]	Amplitude [dB]	Amplitude difference [dB]
	n = 2988.1 rpm s = 0.00496		n = 2986.6 rpm s = 0.00487		
n=1; k=1					
$f_{st1} = 2kf_1$	100.10	20.99	100.04	22.41	-1.42
$f_{st2} = 2f_1 \left[\frac{n}{p}(1-s) + k \right]$	199.80	-38.01	199.60	-30.65	-7.36
n=1; k=3					
$f_{st1} = 2kf_1$	300.40	-11.87	300.20	-4.78	-7.09
$f_{st2} = 2f_1 \left[\frac{n}{p}(1-s) + k \right]$	400.00	-36.27	399.70	-31.71	-4.56
n=1; k=5					
$f_{st1} = 2kf_1$	500.70	-26.08	500.30	-21.58	-4.50
$f_{st2} = 2f_1 \left[\frac{n}{p}(1-s) + k \right]$	600.10	-51.07	599.90	-45.58	-5.49

Table 8-7: Inter-turn fault components for combinations of n and k at 50% load using IPSA.

Load = 50%	Healthy Motor n = 2955.7 rpm s = 0.0134		Faulty Motor n = 2968 rpm s = 0.014		Result
	Frequency [Hz]	Amplitude [dB]	Frequency [Hz]	Amplitude [dB]	Amplitude difference [dB]
n=1; k=1					
$f_{st1} = 2kf_1$	99.85	22.93	100.30	24.54	-1.61
$f_{st2} = 2f_1 \left[\frac{n}{p}(1-s) + k \right]$	198.40	-40.41	199.30	-39.96	-0.45
n=1; k=3					
$f_{st1} = 2kf_1$	299.60	-5.31	301.00	-1.27	-4.05
$f_{st2} = 2f_1 \left[\frac{n}{p}(1-s) + k \right]$	398.10	-43.18	400.00	-43.12	-0.06
n=1; k=5					
$f_{st1} = 2kf_1$	499.30	-19.51	501.70	-14.34	-5.17
$f_{st2} = 2f_1 \left[\frac{n}{p}(1-s) + k \right]$	597.82	-67.60	600.63	-59.84	-7.76

Table 8-8: Inter-turn fault components for combinations of n and k at 100% load using IPSA.

Load = 100%	Healthy Motor n = 2919.6 rpm s = 0.0239		Faulty Motor n = 2928.9 rpm s = 0.0251		Result
	Frequency [Hz]	Amplitude [dB]	Frequency [Hz]	Amplitude [dB]	Amplitude difference [dB]
n=1; k=1					
$f_{st1} = 2kf_1$	99.70	25.36	100.14	25.74	-0.38
$f_{st2} = 2f_1 \left[\frac{n}{p}(1-s) + k \right]$	197.02	-43.74	197.77	-51.74	8.00
n=1; k=3					
$f_{st1} = 2kf_1$	299.10	-4.18	300.42	-0.59	-3.59
$f_{st2} = 2f_1 \left[\frac{n}{p}(1-s) + k \right]$	396.50	-41.34	398.00	-45.68	4.34
n=1; k=5					
$f_{st1} = 2kf_1$	498.60	-19.77	500.70	-17.19	-2.58
$f_{st2} = 2f_1 \left[\frac{n}{p}(1-s) + k \right]$	595.90	-60.20	598.33	-58.13	-2.07

IPSA: Inter-turn fault – 2 shorted turns

Table 8-9: Inter-turn fault components for combinations of n and k at no-load and reduced fault severity using IPSA.

Load = 0%	Healthy Motor n = 2988.1 rpm s = 0.00496		Faulty Motor n = 2987.8 rpm s = 0.0051		Result
	Frequency [Hz]	Amplitude [dB]	Frequency [Hz]	Amplitude [dB]	Amplitude difference [dB]
n=1; k=1					
$f_{st1} = 2kf_1$	100.10	20.99	100.10	22.39	-1.40
$f_{st2} = 2f_1 \left[\frac{n}{p}(1-s) + k \right]$	199.80	-38.01	199.70	-40.12	2.11
n=1; k=3					
$f_{st1} = 2kf_1$	300.20	-11.87	300.30	-5.84	-6.03
$f_{st2} = 2f_1 \left[\frac{n}{p}(1-s) + k \right]$	399.90	-44.06	399.89	-37.86	-6.20
n=1; k=5					
$f_{st1} = 2kf_1$	500.70	-26.08	500.40	-23.89	-2.19
$f_{st2} = 2f_1 \left[\frac{n}{p}(1-s) + k \right]$	600.10	-35.59	600.09	-51.74	16.15

Table 8-10: Inter-turn fault components for combinations of n and k at 50% load and reduced fault severity using IPSA.

Load = 50%	Healthy Motor n = 2955.7 rpm s = 0.0134		Faulty Motor n = 2962 rpm s = 0.0137		Result
	Frequency [Hz]	Amplitude [dB]	Frequency [Hz]	Amplitude [dB]	Amplitude difference [dB]
n=1; k=1					
$f_{st1} = 2kf_1$	99.85	22.93	100.10	23.56	-0.63
$f_{st2} = 2f_1 \left[\frac{n}{p}(1-s) + k \right]$	198.38	-42.52	198.83	-47.47	4.95
n=1; k=3					
$f_{st1} = 2kf_1$	299.60	-5.31	300.30	-6.24	0.92
$f_{st2} = 2f_1 \left[\frac{n}{p}(1-s) + k \right]$	398.10	-43.18	399.03	-46.65	3.47
n=1; k=5					
$f_{st1} = 2kf_1$	499.30	-19.51	500.60	-23.05	3.54
$f_{st2} = 2f_1 \left[\frac{n}{p}(1-s) + k \right]$	597.82	-67.60	599.40	-66.01	-1.59

Table 8-11: Inter-turn fault components for combinations of n and k at 100% load and reduced fault severity using IPSA.

Load = 100%	Healthy Motor n = 2919.6 rpm s = 0.0239		Faulty Motor n = 2930.1 rpm s = 0.0247		Result
	Frequency [Hz]	Amplitude [dB]	Frequency [Hz]	Amplitude [dB]	Amplitude difference [dB]
n=1; k=1					
$f_{st1} = 2kf_1$	99.71	25.36	100.10	25.28	0.08
$f_{st2} = 2f_1 \left[\frac{n}{p}(1-s) + k \right]$	197.02	-43.74	197.81	-45.17	1.43
n=1; k=3					
$f_{st1} = 2kf_1$	299.10	-4.18	300.42	-2.17	-2.01
$f_{st2} = 2f_1 \left[\frac{n}{p}(1-s) + k \right]$	396.42	-41.40	398.09	-43.89	2.49
n=1; k=5					
$f_{st1} = 2kf_1$	498.60	-19.77	500.70	-19.76	-0.01
$f_{st2} = 2f_1 \left[\frac{n}{p}(1-s) + k \right]$	595.90	-60.20	598.40	-61.18	0.98

IPSA: Inter-turn fault - 4 shorted turns (inverter)

Table 8-12: Inter-turn fault components for combinations of n and k for the inverter driven motor at no-load using IPSA.

Load = 0%	Healthy Motor n = 2983.6 rpm s = 0.00547		Faulty Motor n = 2983.7 rpm s = 0.00545		Result
	Frequency [Hz]	Amplitude [dB]	Frequency [Hz]	Amplitude [dB]	Amplitude difference [dB]
n=1; k=1					
$f_{st1} = 2kf_1$	100.00	25.87	100.00	24.32	1.55
$f_{st2} = 2f_1 \left[\frac{n}{p}(1-s) + k \right]$	199.60	-33.72	199.60	-36.70	2.98
n=1; k=3					
$f_{st1} = 2kf_1$	300.00	-4.01	300.00	-5.98	1.97
$f_{st2} = 2f_1 \left[\frac{n}{p}(1-s) + k \right]$	399.45	-34.49	399.46	-40.93	6.44
n=1; k=5					
$f_{st1} = 2kf_1$	500.00	-31.41	500.00	-40.58	9.17
$f_{st2} = 2f_1 \left[\frac{n}{p}(1-s) + k \right]$	599.30	-40.80	599.30	-45.94	5.14

Table 8-13: Inter-turn fault components for combinations of n and k for the inverter driven motor at full load using IPSA.

Load = 100%	Healthy Motor n = 2920.1 rpm s = 0.0266		Faulty Motor n = 2921.9 rpm s = 0.026		Result
	Frequency [Hz]	Amplitude [dB]	Frequency [Hz]	Amplitude [dB]	Amplitude difference [dB]
n=1; k=1					
$f_{st1} = 2kf_1$	100.00	27.09	100.00	26.82	0.27
$f_{st2} = 2f_1 \left[\frac{n}{p}(1-s) + k \right]$	197.20	-48.55	197.30	-48.44	-0.11
n=1; k=3					
$f_{st1} = 2kf_1$	300.00	-4.04	300.00	-4.21	0.17
$f_{st2} = 2f_1 \left[\frac{n}{p}(1-s) + k \right]$	397.40	-39.92	397.40	-39.86	-0.06
n=1; k=5					
$f_{st1} = 2kf_1$	500.00	-37.22	500.00	-26.34	-10.88
$f_{st2} = 2f_1 \left[\frac{n}{p}(1-s) + k \right]$	597.40	-40.99	597.40	-43.42	2.43

IPSA: Inter-turn fault - 2 shorted turns (inverter)

Table 8-14: Inter-turn fault components for combinations of n and k for the inverter driven motor at full load and reduced severity using IPSA.

Load = 100%	Healthy Motor n = 2920.1 rpm s = 0.0266		Faulty Motor n = 2920.2 rpm s = 0.0266		Result
	Frequency [Hz]	Amplitude [dB]	Frequency [Hz]	Amplitude [dB]	Amplitude difference [dB]
n=1; k=1					
$f_{st1} = 2kf_1$	100.00	27.09	100.00	26.54	0.55
$f_{st2} = 2f_1 \left[\frac{n}{p}(1-s) + k \right]$	197.40	-37.29	197.40	-38.85	1.56
n=1; k=3					
$f_{st1} = 2kf_1$	300.00	-4.04	300.00	-4.26	0.23
$f_{st2} = 2f_1 \left[\frac{n}{p}(1-s) + k \right]$	397.40	-36.86	397.40	-39.94	3.08
n=1; k=5					
$f_{st1} = 2kf_1$	500.00	-37.22	500.00	-29.30	-7.92
$f_{st2} = 2f_1 \left[\frac{n}{p}(1-s) + k \right]$	597.30	-44.49	597.30	-48.39	3.90

MSCSA: Inter-turn fault – 4 shorted turns

Table 8-15: Inter-turn fault components for combinations of n and k at no-load using MSCSA.

Load = 0%	Healthy Motor n = 2988.1 rpm s = 0.00496		Faulty Motor n = 2986.6 rpm s = 0.00487		Result
	Frequency [Hz]	Amplitude [dB]	Frequency [Hz]	Amplitude [dB]	Amplitude difference [dB]
n=1; k=1					
$f_{st1} = 2kf_1$	100.10	20.80	100.04	20.84	-0.04
$f_{st2} = 2f_1 \left[\frac{n}{p}(1-s) + k \right]$	199.80	-35.33	199.60	-52.70	17.37
n=1; k=3					
$f_{st1} = 2kf_1$	300.40	-6.94	300.20	-7.31	0.37
$f_{st2} = 2f_1 \left[\frac{n}{p}(1-s) + k \right]$	400.00	-32.95	399.70	-31.71	-1.24
n=1; k=5					
$f_{st1} = 2kf_1$	500.70	-25.61	500.30	-18.29	-7.32
$f_{st2} = 2f_1 \left[\frac{n}{p}(1-s) + k \right]$	600.10	-46.61	599.90	-41.51	-5.10

Table 8-16: Inter-turn fault components for combinations of n and k at 50% load using MSCSA.

Load = 50%	Healthy Motor n = 2955.7 rpm s = 0.0134		Faulty Motor n = 2968 rpm s = 0.014		Result
	Frequency [Hz]	Amplitude [dB]	Frequency [Hz]	Amplitude [dB]	Amplitude difference [dB]
n=1; k=1					
$f_{st1} = 2kf_1$	99.85	22.56	100.30	21.96	0.60
$f_{st2} = 2f_1 \left[\frac{n}{p}(1-s) + k \right]$	198.40	-40.41	199.30	-44.64	4.23
n=1; k=3					
$f_{st1} = 2kf_1$	299.60	-15.26	301.00	-15.98	0.72
$f_{st2} = 2f_1 \left[\frac{n}{p}(1-s) + k \right]$	398.10	-39.31	400.00	-35.18	-4.13
n=1; k=5					
$f_{st1} = 2kf_1$	499.30	-17.68	501.70	-12.25	-5.43
$f_{st2} = 2f_1 \left[\frac{n}{p}(1-s) + k \right]$	597.82	-47.03	600.63	-48.16	1.13

Table 8-17: Inter-turn fault components for combinations of n and k at 100% load using MSCSA.

Load = 100%	Healthy Motor n = 2919.6 rpm s = 0.0239		Faulty Motor n = 2928.9 rpm s = 0.0251		Result
	Frequency [Hz]	Amplitude [dB]	Frequency [Hz]	Amplitude [dB]	Amplitude difference [dB]
n=1; k=1					
$f_{st1} = 2kf_1$	99.71	26.43	100.14	23.68	2.75
$f_{st2} = 2f_1 \left[\frac{n}{p}(1-s) + k \right]$	197.02	-43.00	197.77	-39.26	-3.74
n=1; k=3					
$f_{st1} = 2kf_1$	299.10	-13.65	300.42	-3.87	-9.78
$f_{st2} = 2f_1 \left[\frac{n}{p}(1-s) + k \right]$	396.50	-36.48	398.00	-38.93	2.45
n=1; k=5					
$f_{st1} = 2kf_1$	498.60	-17.88	500.70	-13.69	-4.19
$f_{st2} = 2f_1 \left[\frac{n}{p}(1-s) + k \right]$	595.90	-49.31	598.33	-54.26	4.95

MSCSA: Inter-turn fault – 2 shorted turns

Table 8-18: Inter-turn fault components for combinations of n and k at no-load and reduced severity using MSCSA.

Load = 0%	Healthy Motor n = 2988.1 rpm s = 0.00496		Faulty Motor n = 2987.8 rpm s = 0.0051		Result
	Frequency [Hz]	Amplitude [dB]	Frequency [Hz]	Amplitude [dB]	Amplitude difference [dB]
n=1; k=1					
$f_{st1} = 2kf_1$	100.10	20.80	100.10	21.39	-0.59
$f_{st2} = 2f_1 \left[\frac{n}{p}(1-s) + k \right]$	199.80	-35.55	199.60	-35.94	0.39
n=1; k=3					
$f_{st1} = 2kf_1$	300.40	-6.94	300.20	-5.91	-1.04
$f_{st2} = 2f_1 \left[\frac{n}{p}(1-s) + k \right]$	399.90	-37.64	399.89	-31.15	-6.49
n=1; k=5					
$f_{st1} = 2kf_1$	500.70	-25.61	500.40	-21.66	-3.95
$f_{st2} = 2f_1 \left[\frac{n}{p}(1-s) + k \right]$	600.10	-29.31	600.09	-50.05	6.28

Table 8-19: Inter-turn fault components for combinations of n and k at 50% load and reduced severity using MSCSA.

Load = 50%	Healthy Motor n = 2955.7 rpm s = 0.0134		Faulty Motor n = 2962 rpm s = 0.0137		Result
	Frequency [Hz]	Amplitude [dB]	Frequency [Hz]	Amplitude [dB]	Amplitude difference [dB]
n=1; k=1					
$f_{st1} = 2kf_1$	99.85	22.56	100.10	21.60	0.96
$f_{st2} = 2f_1 \left[\frac{n}{p}(1-s) + k \right]$	198.38	-40.41	198.83	-48.33	7.92
n=1; k=3					
$f_{st1} = 2kf_1$	299.60	-15.26	300.30	-18.70	3.44
$f_{st2} = 2f_1 \left[\frac{n}{p}(1-s) + k \right]$	398.10	-39.31	399.03	-43.02	3.71
n=1; k=5					
$f_{st1} = 2kf_1$	499.30	-17.78	500.60	-21.54	3.76
$f_{st2} = 2f_1 \left[\frac{n}{p}(1-s) + k \right]$	597.82	-47.03	599.30	-52.09	5.06

Table 8-20: Inter-turn fault components for combinations of n and k at 100% load and reduced severity using MSCSA.

Load = 100%	Healthy Motor n = 2919.6 rpm s = 0.0239		Faulty Motor n = 2930.1 rpm s = 0.0247		Result
	Frequency [Hz]	Amplitude [dB]	Frequency [Hz]	Amplitude [dB]	Amplitude difference [dB]
n=1; k=1					
$f_{st1} = 2kf_1$	99.71	26.43	100.10	22.88	3.55
$f_{st2} = 2f_1 \left[\frac{n}{p}(1-s) + k \right]$	197.02	-43.00	197.81	-45.29	2.29
n=1; k=3					
$f_{st1} = 2kf_1$	299.10	-13.65	300.42	-9.08	-4.57
$f_{st2} = 2f_1 \left[\frac{n}{p}(1-s) + k \right]$	396.42	-36.67	398.09	-40.87	4.20
n=1; k=5					
$f_{st1} = 2kf_1$	498.60	-17.88	500.70	-19.76	1.88
$f_{st2} = 2f_1 \left[\frac{n}{p}(1-s) + k \right]$	595.90	-49.31	598.40	-53.44	4.13

MSCSA: Inter-turn fault – 4 shorted turns (inverter)

Table 8-21: Inter-turn fault components for combinations of n and k at 0% load for an inverter driven motor using MSCSA.

Load = 0%	Healthy Motor n = 2983.6rpm s = 0.0545		Faulty Motor n = 2983.6 rpm s = 0.00545		Result
	Frequency [Hz]	Amplitude [dB]	Frequency [Hz]	Amplitude [dB]	Amplitude difference [dB]
n=1; k=1					
$f_{st1} = 2kf_1$	100.00	33.04	100.00	26.47	6.57
$f_{st2} = 2f_1 \left[\frac{n}{p}(1-s) + k \right]$	199.60	-14.91	199.60	-24.68	9.77
n=1; k=3					
$f_{st1} = 2kf_1$	300.00	8.81	300.00	-0.10	8.91
$f_{st2} = 2f_1 \left[\frac{n}{p}(1-s) + k \right]$	399.45	-20.70	399.46	-25.23	4.53
n=1; k=5					
$f_{st1} = 2kf_1$	500.00	-17.86	500.00	-22.35	4.49
$f_{st2} = 2f_1 \left[\frac{n}{p}(1-s) + k \right]$	599.30	-20.34	599.30	-30.98	10.64

Table 8-22: Inter-turn fault components for combinations of n and k at 100% load for an inverter driven motor using MSCSA.

Load = 100%	Healthy Motor n = 2920.1 rpm s = 0.0266		Faulty Motor n = 2921.9 rpm s = 0.026		Result
	Frequency [Hz]	Amplitude [dB]	Frequency [Hz]	Amplitude [dB]	Amplitude difference [dB]
n=1; k=1					
$f_{st1} = 2kf_1$	100.00	32.05	100.00	27.95	4.10
$f_{st2} = 2f_1 \left[\frac{n}{p}(1-s) + k \right]$	197.34	-23.38	197.40	-38.16	14.78
n=1; k=3					
$f_{st1} = 2kf_1$	300.00	-0.48	300.00	-7.04	6.56
$f_{st2} = 2f_1 \left[\frac{n}{p}(1-s) + k \right]$	397.40	-22.48	397.40	-29.16	6.68
n=1; k=5					
$f_{st1} = 2kf_1$	500.00	-10.97	500.00	-37.22	26.25
$f_{st2} = 2f_1 \left[\frac{n}{p}(1-s) + k \right]$	597.30	-23.64	597.30	-28.03	4.39

MSCSA: Inter-turn fault – 2 shorted turns (inverter)

Table 8-23: Inter-turn fault components for combinations of n and k at 100% load and reduced severity for an inverter driven motor using MSCSA.

Load = 100%	Healthy Motor n = 2920.1 rpm s = 0.0266		Faulty Motor n = 2920.2 rpm s = 0.0266		Result
	Frequency [Hz]	Amplitude [dB]	Frequency [Hz]	Amplitude [dB]	Amplitude difference [dB]
n=1; k=1					
$f_{st1} = 2kf_1$	100.00	32.05	100.00	27.83	4.22
$f_{st2} = 2f_1 \left[\frac{n}{p}(1-s) + k \right]$	197.40	-32.61	197.40	-34.54	1.93
n=1; k=3					
$f_{st1} = 2kf_1$	300.00	-0.48	300.00	-5.53	5.04
$f_{st2} = 2f_1 \left[\frac{n}{p}(1-s) + k \right]$	397.40	-22.48	397.40	-32.65	10.17
n=1; k=5					
$f_{st1} = 2kf_1$	500.00	-10.97	500.00	-16.50	5.53
$f_{st2} = 2f_1 \left[\frac{n}{p}(1-s) + k \right]$	597.30	-23.64	597.30	-34.96	11.32

MCSA: Broken Rotor Bar Fault, Grid supplied

Table 8-24: Broken rotor bar fault components and its multiples for a motor at no-load.

Load = 0% Grid Connected MCSA	Healthy Motor n = 2988.1 rpm s = 0.00496		Faulty Motor with 3 broken bars n = 2982.3 rpm s = 0.00551		Result
	Frequency [Hz]	Amplitude [dB]	Frequency [Hz]	Amplitude [dB]	Amplitude diff. [dB]
k = 1					
$f_{bu} = f_1(1 + 2ks)$	50.55	-46.27	50.53	-38.48	-7.79
$f_{bl} = f_1(1 - 2ks)$	49.55	-45.34	49.43	-38.26	-7.08
k = 2					
$f_{bu} = f_1(1 + 2ks)$	51.04	-73.71	51.08	-57.47	-16.24
$f_{bl} = f_1(1 - 2ks)$	49.06	-77.13	48.88	-56.30	-20.83
k = 3					
$f_{bu} = f_1(1 + 2ks)$	51.54	-78.33	51.63	-66.92	-11.41
$f_{bl} = f_1(1 - 2ks)$	48.56	-72.35	48.33	-65.49	-6.86

Table 8-25: Broken rotor bar fault components and its multiples for a motor at 50% load.

Load = 50% Grid Connected MCSA	Healthy Motor n = 2955.7 rpm s = 0.0134		Faulty Motor with 3 broken bars n = 2952.6 rpm s = 0.0148		Result
	Frequency [Hz]	Amplitude [dB]	Frequency [Hz]	Amplitude [dB]	Amplitude diff. [dB]
k = 1					
$f_{bu} = f_1(1 + 2ks)$	51.27	-46.54	51.43	-38.67	-7.87
$f_{bl} = f_1(1 - 2ks)$	48.59	-46.56	48.47	-38.69	-7.87
k = 2					
$f_{bu} = f_1(1 + 2ks)$	52.61	-66.02	52.91	-53.35	-12.67
$f_{bl} = f_1(1 - 2ks)$	47.25	-66.97	46.99	-55.44	-11.53
k = 3					
$f_{bu} = f_1(1 + 2ks)$	53.94	-67.32	54.39	-55.33	-11.99
$f_{bl} = f_1(1 - 2ks)$	45.92	-67.44	45.51	-57.42	-10.02

Table 8-26: Broken rotor bar fault components and its multiples for a motor at 100% load.

Load = 100% Grid Connected MCSA	Healthy Motor n = 2919.6 rpm s = 0.0239		Faulty Motor with 3 broken bars n = 2913.4 rpm s = 0.0265		Result
	Frequency [Hz]	Amplitude [dB]	Frequency [Hz]	Amplitude [dB]	Amplitude diff. [dB]
k = 1					
$f_{bu} = f_1(1 + 2ks)$	52.23	-50.85	52.53	-40.55	-10.30
$f_{bl} = f_1(1 - 2ks)$	47.47	-49.39	47.23	-41.71	-7.68
k = 2					
$f_{bu} = f_1(1 + 2ks)$	54.61	-64.76	55.17	-55.18	-9.58
$f_{bl} = f_1(1 - 2ks)$	45.09	-65.60	44.59	-51.33	-14.27
k = 3					
$f_{bu} = f_1(1 + 2ks)$	56.99	-68.47	57.82	-53.04	-15.43
$f_{bl} = f_1(1 - 2ks)$	42.71	-65.93	41.94	-53.85	-12.08

MCSA: Broken Rotor Bar Fault, Inverter supplied

Table 8-27: Broken rotor bar fault components and its multiples for an inverter driven motor at no-load.

Load = 0% Inverter MCSA	Healthy Motor n = 2983.6 rpm s = 0.0055		Faulty Motor with 3 broken bars n = 2982.9 rpm s = 0.0057		Result
	Frequency [Hz]	Amplitude [dB]	Frequency [Hz]	Amplitude [dB]	Amplitude diff. [dB]
k = 1					
$f_{bu} = f_1(1 + 2ks)$	50.55	-45.59	50.57	-38.93	-6.66
$f_{bl} = f_1(1 - 2ks)$	49.45	-46.19	49.43	-38.85	-7.34
k = 2					
$f_{bu} = f_1(1 + 2ks)$	51.09	-71.25	51.14	-60.03	-11.22
$f_{bl} = f_1(1 - 2ks)$	48.91	-69.62	48.86	-58.96	-10.66
k = 3					
$f_{bu} = f_1(1 + 2ks)$	51.64	-72.09	51.71	-66.76	-5.33
$f_{bl} = f_1(1 - 2ks)$	48.36	-71.39	48.29	-63.08	-8.31

Table 8-28: Broken rotor bar fault components and its multiples for an inverter driven motor at full load.

Load = 100% Inverter MCSA	Healthy Motor n = 2920.1 rpm s = 0.0266		Faulty Motor with 3 broken bars n = 2915.6 rpm s = 0.0281		Result
	Frequency [Hz]	Amplitude [dB]	Frequency [Hz]	Amplitude [dB]	Amplitude diff. [dB]
k = 1					
$f_{bu} = f_1(1 + 2ks)$	52.66	-53.26	52.81	-41.14	-12.12
$f_{bl} = f_1(1 - 2ks)$	47.34	-50.77	47.19	-42.11	-8.66
k = 2					
$f_{bu} = f_1(1 + 2ks)$	55.33	-64.31	55.63	-52.77	-11.54
$f_{bl} = f_1(1 - 2ks)$	44.67	-66.53	44.37	-49.00	-17.53
k = 3					
$f_{bu} = f_1(1 + 2ks)$	57.99	-64.79	58.44	-53.46	-11.33
$f_{bl} = f_1(1 - 2ks)$	42.01	-64.11	41.56	-52.03	-12.08

IPSA: Broken Rotor Bar Fault, Grid supplied

Table 8-29: Broken rotor bar fault components and its multiples for a motor at 0% load using IPSA.

Load = 0% Grid Connected IPSA	Healthy Motor n = 2988.1 rpm s = 0.00496		Faulty Motor with 3 broken bars n = 2982.3 rpm s = 0.00551		Result
	Frequency [Hz]	Amplitude [dB]	Frequency [Hz]	Amplitude [dB]	Amplitude diff. [dB]
k = 1					
$f_{br1} = 2ksf_1$	0.4883	-45.16	0.5615	-40.51	-4.65
$f_{br2U} = 2f_1(1 + ks)$	100.6	-45.69	100.5	-40.01	-5.68
$f_{br2L} = 2f_1(1 - ks)$	99.63	-48.18	99.39	-39.93	-8.25
k = 2					
$f_{br1} = 2ksf_1$	1.05	-73.69	1.123	-58.91	-14.78
$f_{br2U} = 2f_1(1 + ks)$	101.1	-68.09	101.1	-59.62	-8.47
$f_{br2L} = 2f_1(1 - ks)$	99.1	-66.94	98.83	-60.71	-6.23
k = 3					
$f_{br1} = 2ksf_1$	1.465	-68.45	1.685	-64.94	-3.51
$f_{br2U} = 2f_1(1 + ks)$	101.6	-75.83	101.6	-66.81	-9.02
$f_{br2L} = 2f_1(1 - ks)$	98.66	-79.59	98.29	-69.4	-10.19

Table 8-30: Broken rotor bar fault components and its multiples for a motor at 50% load using IPSA.

Load = 50% Grid Connected IPSA	Healthy Motor n = 2955.7 rpm s = 0.0134		Faulty Motor with 3 broken bars n = 2952.6 rpm s = 0.0148		Result
	Frequency [Hz]	Amplitude [dB]	Frequency [Hz]	Amplitude [dB]	Amplitude diff. [dB]
k = 1					
$f_{br1} = 2ksf_1$	1.343	-47.12	1.489	-39.81	7.31
$f_{br2U} = 2f_1(1 + ks)$	101.2	-48.44	101.4	-39.93	-8.51
$f_{br2L} = 2f_1(1 - ks)$	98.54	-48.14	98.41	-40.09	-8.05
k = 2					
$f_{br1} = 2ksf_1$	2.686	-68.07	3.003	-51.62	-16.45
$f_{br2U} = 2f_1(1 + ks)$	102.5	-65.82	102.9	-54.72	-11.1
$f_{br2L} = 2f_1(1 - ks)$	97.19	-65.41	96.92	-58.19	-7.22
k = 3					
$f_{br1} = 2ksf_1$	4.004	-66.52	4.492	-54.75	-11.77
$f_{br2U} = 2f_1(1 + ks)$	103.9	-69.63	104.4	-57.69	-11.94
$f_{br2L} = 2f_1(1 - ks)$	95.85	-66.05	95.41	-58	-8.05

Table 8-31: Broken rotor bar fault components and its multiples for a motor at 100% load using IPSA.

Load = 100% Grid Connected IPSA	Healthy Motor n = 2919.6 rpm s = 0.0239		Faulty Motor with 3 broken bars n = 2913.4 rpm s = 0.0265		Result
	Frequency [Hz]	Amplitude [dB]	Frequency [Hz]	Amplitude [dB]	Amplitude diff. [dB]
k = 1					
$f_{br1} = 2ksf_1$	2.368	-49.85	2.661	-40.86	-8.99
$f_{br2U} = 2f_1(1 + ks)$	102.1	-52.66	102.4	-42.62	-10.04
$f_{br2L} = 2f_1(1 - ks)$	97.34	-51.67	97.09	-44.03	-7.64
k = 2					
$f_{br1} = 2ksf_1$	4.761	-66.3	5.298	-46.45	-19.85
$f_{br2U} = 2f_1(1 + ks)$	104.5	-65.31	105.1	-53	-12.31
$f_{br2L} = 2f_1(1 - ks)$	94.95	-67.75	94.46	-51.61	-16.14

k = 3					
$f_{br1} = 2ksf_1$	7.129	-65.47	7.959	-49.3	-16.17
$f_{br2U} = 2f_1(1 + ks)$	106.8	-70.91	107.7	-54.64	-16.27
$f_{br2L} = 2f_1(1 - ks)$	92.58	-65.44	91.8	-54.33	-11.11

IPSA: Broken Rotor Bar Fault, Inverter supplied

Table 8-32: Broken rotor bar fault components and its multiples for an inverter driven motor at 0% load using IPSA.

Load = 0% Inverter Supplied IPSA	Healthy Motor n = 2983.6 rpm s = 0.0055		Faulty Motor with 3 broken bars n = 2982.9 rpm s = 0.0057		Result
	Frequency [Hz]	Amplitude [dB]	Frequency [Hz]	Amplitude [dB]	Amplitude diff. [dB]
k = 1					
$f_{br1} = 2ksf_1$	0.5127	-47.67	-41	0.5859	-6.67
$f_{br2U} = 2f_1(1 + ks)$	100.5	-46.96	-38.2	100.6	-8.76
$f_{br2L} = 2f_1(1 - ks)$	99.49	-47.07	-39.35	99.41	-7.72
k = 2					
$f_{br1} = 2ksf_1$	1.05	-70.7	-60.08	1.147	-10.62
$f_{br2U} = 2f_1(1 + ks)$	101	-75.31	-58.02	101.2	-17.29
$f_{br2U} = 2f_1(1 - ks)$	98.95	-73.4	-59	98.85	-14.4
k = 3					
$f_{br1} = 2ksf_1$	1.538	-69.05	-63.18	1.733	-5.87
$f_{br2U} = 2f_1(1 + ks)$	101.6	-67.48	-63.23	101.7	-4.25
$f_{br2L} = 2f_1(1 - ks)$	98.44	-73.56	-63.3	98.27	-10.26

Table 8-33: Broken rotor bar fault components and its multiples for an inverter driven motor at 0% load using IPSA.

Load = 0% Inverter Supplied IPSA	Healthy Motor n = 2920.1 rpm s = 0.0266		Faulty Motor with 3 broken bars n = 2915.6 rpm s = 0.0281		Result
	Frequency [Hz]	Amplitude [dB]	Frequency [Hz]	Amplitude [dB]	Amplitude diff. [dB]
k = 1					
$f_{br1} = 2ksf_1$	2.661	-50.68	2.832	-41.46	-9.22
$f_{br2U} = 2f_1(1 + ks)$	102.7	-52.06	102.8	-41.6	-10.46
$f_{br2L} = 2f_1(1 - ks)$	97.36	-52.32	97.17	-44.82	-7.5
k = 2					
$f_{br1} = 2ksf_1$	5.298	-69.08	5.64	-46.02	-23.06
$f_{br2U} = 2f_1(1 + ks)$	105.3	-65.22	105.7	-52.57	-12.65
$f_{br2L} = 2f_1(1 - ks)$	94.7	-65.09	94.36	-48.57	-16.52
k = 3					
$f_{br1} = 2ksf_1$	7.935	-65	8.472	-48.42	-16.58
$f_{br2U} = 2f_1(1 + ks)$	107.9	-69.49	108.5	-55.04	-14.45
$f_{br2L} = 2f_1(1 - ks)$	92.07	-65.83	91.53	-51.41	-14.42

MSCSA: Broken Rotor Bar Fault, Grid supplied

Table 8-34: Broken rotor bar fault components and its multiples for a motor at 0% load using MSCSA.

Load = 0% Grid Connected MSCSA	Healthy Motor n = 2988.1 rpm s = 0.00496		Faulty Motor with 3 broken bars n = 2982.3 rpm s = 0.00551		Result
	Frequency [Hz]	Amplitude [dB]	Frequency [Hz]	Amplitude [dB]	Amplitude diff. [dB]
k = 1					
$f_{br1} = 2ksf_1$	0.4883	-40.44	0.5615	-33.74	-6.7
$f_{br2U} = 2f_1(1 + ks)$	100.6	-48.81	100.5	-39.89	-8.92
$f_{br2L} = 2f_1(1 - ks)$	99.63	-49.69	99.39	-40.6	-9.09
k = 2					
$f_{br1} = 2ksf_1$	0.9766	-65.76	1.123	-53.71	-12.05
$f_{br2U} = 2f_1(1 + ks)$	101.1	-75.05	101.1	-58.59	-16.46
$f_{br2L} = 2f_1(1 - ks)$	99.1	-70.79	98.83	-59.82	-10.97

k = 3					
$f_{br1} = 2ksf_1$	1.465	-68.81	1.685	-59.64	-9.17
$f_{br2U} = 2f_1(1 + ks)$	101.5	-72.81	101.6	-63.54	-9.27
$f_{br2L} = 2f_1(1 - ks)$	98.63	-73.51	98.29	-62.39	-11.12

Table 8-35: Broken rotor bar fault components and its multiples for a motor at 50% load using MSCSA.

Load = 50% Grid Connected MSCSA	Healthy Motor n = 2955.7 rpm s = 0.0134		Faulty Motor with 3 broken bars n = 2952.6 rpm s = 0.0148		Result
	Frequency [Hz]	Amplitude [dB]	Frequency [Hz]	Amplitude [dB]	Amplitude diff. [dB]
k = 1					
$f_{br1} = 2ksf_1$	1.343	-43.23	1.489	-35.86	-7.37
$f_{br2U} = 2f_1(1 + ks)$	101.2	-49.03	101.4	-40.12	-8.91
$f_{br2L} = 2f_1(1 - ks)$	98.54	-48.41	98.41	-40.82	-7.59
k = 2					
$f_{br1} = 2ksf_1$	2.686	-60.7	3.003	-52.1	-8.6
$f_{br2U} = 2f_1(1 + ks)$	102.5	-67.08	102.9	-53.6	-13.48
$f_{br2L} = 2f_1(1 - ks)$	97.19	-66.53	96.92	-56.8	-9.73
k = 3					
$f_{br1} = 2ksf_1$	4.004	-63.4	4.4492	-53	-10.4
$f_{br2U} = 2f_1(1 + ks)$	103.9	-67.47	104.4	-56.72	-10.75
$f_{br2L} = 2f_1(1 - ks)$	95.85	-65.95	95.41	-58.4	-7.55

Table 8-36: Broken rotor bar fault components and its multiples for a motor at 100% load using MSCSA.

Load = 100% Grid Connected MSCSA	Healthy Motor n = 2919.6 rpm s = 0.0239		Faulty Motor with 3 broken bars n = 2913.4 rpm s = 0.0265		Result
	Frequency [Hz]	Amplitude [dB]	Frequency [Hz]	Amplitude [dB]	Amplitude diff. [dB]
k = 1					
$f_{br1} = 2ksf_1$	2.368	-48.63	2.661	-40.13	-8.5
$f_{br2U} = 2f_1(1 + ks)$	102.1	-52.96	102.4	-42.14	-10.82
$f_{br2L} = 2f_1(1 - ks)$	97.34	-50.45	97.09	-44.08	-6.37
k = 2					
$f_{br1} = 2ksf_1$	4.761	-61.34	5.298	-57.39	-3.95
$f_{br2U} = 2f_1(1 + ks)$	104.5	-64.86	105.1	-52.88	-11.98
$f_{br2L} = 2f_1(1 - ks)$	94.95	-67.56	94.46	-52.32	-15.24
k = 3					
$f_{br1} = 2ksf_1$	7.129	-63.57	7.959	-56.65	-6.92
$f_{br2U} = 2f_1(1 + ks)$	106.8	-69.27	107.7	-54.66	-14.61
$f_{br2L} = 2f_1(1 - ks)$	92.58	-65.43	91.8	-54.45	-10.98

MSCSA: Broken Rotor Bar Fault, Inverter supplied

Table 8-37: Broken rotor bar fault components and its multiples for an inverter driven motor at 0% load using MSCSA.

Load = 0% Inverter Supplied MSCSA	Healthy Motor n = 2983.6 rpm s = 0.0055		Faulty Motor with 3 broken bars n = 2982.9 rpm s = 0.0057		Result
	Frequency [Hz]	Amplitude [dB]	Frequency [Hz]	Amplitude [dB]	Amplitude diff. [dB]
k = 1					
$f_{br1} = 2ksf_1$	0.5859	-41.08	0.5127	-33.26	-7.82
$f_{br2U} = 2f_1(1 + ks)$	100.5	-47.87	100.6	-39.14	-8.73
$f_{br2L} = 2f_1(1 - ks)$	99.49	-46.29	99.41	-39.97	-6.32
k = 2					

$f_{br1} = 2ksf_1$	1.025	-65.06	1.147	-53.03	-12.03
$f_{br2U} = 2f_1(1 + ks)$	101	-73.16	101.2	-58.05	-15.11
$f_{br2L} = 2f_1(1 - ks)$	98.97	-72.62	98.85	-58.77	-13.85
k = 3					
$f_{br1} = 2ksf_1$	1.685	-78.33	1.733	-57.54	-20.79
$f_{br2U} = 2f_1(1 + ks)$	101.6	-69.62	101.7	-63.38	-6.24
$f_{br2L} = 2f_1(1 - ks)$	98.44	-68.3	98.27	-61.04	-7.26

Table 8-38: Broken rotor bar fault components and its multiples for an inverter driven motor at 100% load using MSCSA.

Load = 100% Inverter Supplied MSCSA	Healthy Motor n = 2920.1 rpm s = 0.0266		Faulty Motor with 3 broken bars n = 2915.6 rpm s = 0.0281		Result
	Frequency [Hz]	Amplitude [dB]	Frequency [Hz]	Amplitude [dB]	Amplitude diff. [dB]
k = 1					
$f_{br1} = 2ksf_1$	2.661	-50.74	2.832	-40.73	-10.01
$f_{br2U} = 2f_1(1 + ks)$	102.7	-52.84	102.8	-41.14	-11.7
$f_{br2L} = 2f_1(1 - ks)$	97.36	-50.79	97.17	-44.07	-6.72
k = 2					
$f_{br1} = 2ksf_1$	5.298	-62.34	5.64	-55.5	-6.84
$f_{br2U} = 2f_1(1 + ks)$	105.3	-67.42	105.7	-52.91	-14.51
$f_{br2L} = 2f_1(1 - ks)$	94.7	-66.59	94.36	-50.11	-16.48
k = 3					
$f_{br1} = 2ksf_1$	7.959	-66.24	8.472	-58.05	-8.19
$f_{br2U} = 2f_1(1 + ks)$	107.9	-69.26	108.5	-54.62	-14.64
$f_{br2L} = 2f_1(1 - ks)$	92.07	-66.39	91.53	-52.11	-14.28

MSCSA: The Effect of Field Weakening on Broken Rotor Bar Fault Detection

Table 8-39: Summary of sideband distance from the fundamental frequency at 90% rated voltage using MSCSA.

MSCSA Load = 0%	Healthy motor 90% V	Faulty motor 90% V	Faulty motor 100% V	Frequency shift between fault components
	n = 2977.9 rpm s = 0.0084	n = 2967.9 rpm s = 0.0077	n = 2982.3 rpm s = 0.0055	
	Frequency [Hz]	Frequency [Hz]	Frequency [Hz]	[Hz]
2 X Fundamental Frequency	50.05	49.85	49.98	
Distance from DC component f_{br1}	0.84	0.77	0.55	0.22
Distance from 2 X fundamental f_{br2U}	0.84	0.77	0.55	0.22
Distance from 2 X fundamental f_{br2L}	-0.84	-0.77	-0.55	-0.22

Table 8-40: Summary of sideband distance from the fundamental frequency at 80% rated voltage using MSCSA.

MSCSA Load = 0%	Healthy motor 80% V	Faulty motor 80% V	Faulty motor 100% V	Frequency shift between fault components
	n = 2972 rpm s = 0.00997	n = 2971.3 rpm s = 0.00974	n = 2982.3 rpm s = 0.0055	
	Frequency [Hz]	Frequency [Hz]	Frequency [Hz]	[Hz]
2 X Fundamental Frequency	50.02	50.02	49.98	
Distance from DC component f_{br1}	0.97	1.00	0.55	0.45
Distance from 2 X fundamental f_{br2U}	0.97	1.00	0.55	0.45
Distance from 2 X fundamental f_{br2L}	-0.97	-1.00	-0.55	-0.45

MCSA: Bearing faults

Table 8-41: Bearing fault components for inner and outer race faults at various motor loads.

GRID m = 1	Healthy Motor		Faulty Motor		Result
	Frequency [Hz]	Amplitude [dB]	Frequency [Hz]	Amplitude [dB]	Amplitude difference [dB]
Load = 0%	n = 2988.1 rpm s = 0.00496		n = 2995.4 rpm s = 0.00451		
<i>BFO+</i>	203.7	-103.5	203.7	-93.16	-10.34
<i>BFO-</i>	109.3	none	109.6	none	no result
<i>BFI+</i>	289	-103	289.1	-95.63	-7.37
<i>BFI-</i>	189.6	-103.6	189.6	-95.28	-8.32
Load = 50%	n = 2955.7 rpm s = 0.0134		n = 2957.6 rpm s = 0.0132		
<i>BFO+</i>	203.1	-95.2	203.3	-75.32	-19.88
<i>BFO-</i>	109.5	-98.66	109.5	-87.42	-11.24
<i>BFI+</i>	284.7	-108.2	284.6	-96.14	-12.06
<i>BFI-</i>	186.2	-104.4	186.2	-94.24	-10.16
Load = 100%	n = 2933.5 rpm s = 0.0241		n = 2935.6 rpm s = 0.0238		
<i>BFO+</i>	201.6	-98.57	201.7	-85.69	-12.88
<i>BFO-</i>	106.1	-95.14	106.2	-86.45	-8.69
<i>BFI+</i>	284	-103.1	283.9	-89.06	-14.04
<i>BFI-</i>	184.6	none	184.7	none	no result

Table 8-42: Bearing fault components for inner and outer race faults at various motor loads (inverter driven).

INVERTER m = 1	Healthy Motor		Faulty Motor		Result
	Frequency [Hz]	Amplitude [dB]	Frequency [Hz]	Amplitude [dB]	Amplitude difference [dB]
Load = 0%	n = 2983.6 rpm s = 0.00482		n = 2985.6 rpm s = 0.00547		
<i>BFO+</i>	203.6	-66.87	203.7	-57.06	-9.81
<i>BFO-</i>	107.8	-68.17	107.9	-50.25	-17.92
<i>BFI+</i>	288.1	-73.32	288.1	-55.41	-17.91
<i>BFI-</i>	188.1	-69.84	188.1	-47.83	-22.01
Load = 100%	n = 2920.1 rpm s = 0.02663		n = 2925.1 rpm s = 0.02495		
<i>BFO+</i>	200.8	-67.03	200.7	-58.77	-8.26
<i>BFO-</i>	105.7	none	106	none	none
<i>BFI+</i>	285.5	-76.1	285.5	-61.96	-14.14
<i>BFI-</i>	184.8	-73.27	184.8	-58.25	-15.02

Appendix C – Derivations

Equation (3.8) associated with an inter-turn fault and the square of the current is now derived.

Assume that the Phase A instantaneous current consists of the fundamental, upper and lower sideband components:

$$i_a(t) = I_{ml} \sin(\omega_1 t) + I_u \sin(\omega_u t - \beta_u) + I_l \sin(\omega_l t - \beta_l) \quad (8.1)$$

Where I_{ml} is the maximum line current, ω_1 is the supply frequency, ω_u is the frequency of the upper sideband harmonic, ω_l is the frequency of the lower sideband harmonic, β_u is the phase angle of the upper sideband harmonic current and β_l is the phase angle of the lower sideband harmonic current. Hence, the square of the current will be given by:

$$i_a^2(t) = \{I_{ml} \sin(\omega_1 t) + I_u \sin(\omega_u t - \beta_u) + I_l \sin(\omega_l t - \beta_l)\}^2 \quad (8.2)$$

$$i_a^2(t) = I_{ml}^2 \sin^2(\omega_1 t) + I_u^2 \sin^2(\omega_u t - \beta_u) + I_l^2 \sin^2(\omega_l t - \beta_l) + 2I_{ml}I_u \sin(\omega_1 t) \sin(\omega_u t - \beta_u) + 2I_{ml}I_l \sin(\omega_1 t) \sin(\omega_l t - \beta_l) + 2I_uI_l \sin(\omega_u t - \beta_u) \sin(\omega_l t - \beta_l) \quad (8.3)$$

Since $\sin^2\theta = (1 - \cos 2\theta)/2$

Hence, for the first term (fundamental) of (8.3):

$$\begin{aligned} & I_{ml}^2 \sin^2(\omega_1 t) \\ &= \frac{I_{ml}^2}{2} (1 - \cos(2\omega_1 t)) \\ &= \frac{I_{ml}^2}{2} - \frac{I_{ml}^2}{2} \cos(2\omega_1 t) \end{aligned}$$

Hence the fundamental component produces a dc term and term at twice the fundamental frequency f_1 .

When considering the second term for the upper sideband components of (8.3):

$$\begin{aligned} & I_u^2 \sin^2(\omega_u t - \beta_u) \\ &= \frac{I_u^2}{2} (1 - \cos(2\omega_u t - 2\beta_u)) \end{aligned}$$

Since $\omega_u = 2\pi f_u$ where $f_u = f_1 \left[\frac{n}{p}(1-s) + k \right]$

$$= \frac{I_u^2}{2} - \frac{I_u^2}{2} \cos \left(2 \times 2\pi f_1 \left[\frac{n}{p}(1-s) + k \right] t - 2\beta_u \right)$$

Hence, the fault frequency associated with the upper sideband component is given by:

$$f_{fault\ upper} = 2f_1 \left[\frac{n}{p}(1-s) + k \right]$$

Similarly, when considering the third term for the lower sideband component of (8.3):

$$\begin{aligned} & I_l^2 \sin^2(\omega_l t - \beta_l) \\ &= \frac{I_l^2}{2} (1 - \cos(2\omega_l t - \beta_l)) \\ &= \frac{I_l^2}{2} - \frac{I_l^2}{2} \cos \left(2 \times 2\pi f_1 \left[\frac{n}{p}(1-s) - k \right] t - \beta_l \right) \end{aligned}$$

Hence, the fault frequency associated with the lower sideband component is given by:

$$f_{fault\ lower} = 2f_1 \left[\frac{n}{p}(1-s) - k \right]$$

Thus the stator fault component frequency using the square of the current is given by:

$$f_{st2} = 2f_1 \left[\frac{n}{p}(1-s) \pm k \right]$$

9 EBE Faculty: Assessment of Ethics in Research Projects

Application for Approval of Ethics in Research (EiR) Projects
Faculty of Engineering and the Built Environment, University of Cape Town

APPLICATION FORM


Please Note:



Any person planning to undertake research in the Faculty of Engineering and the Built Environment (EBE) at the University of Cape Town is required to complete this form **before** collecting or analysing data. The objective of submitting this application *prior* to embarking on research is to ensure that the highest ethical standards in research, conducted under the auspices of the EBE Faculty, are met. Please ensure that you have read, and understood the **EBE Ethics in Research Handbook**(available from the UCT EBE, Research Ethics website) prior to completing this application form: <http://www.ebe.uct.ac.za/usr/ebe/research/ethics.pdf>

APPLICANT'S DETAILS	
Name of principal researcher, student or external applicant	
Naasef Rylands	
Department	
Electrical Engineering	
Preferred email address of applicant:	
nrylands@gmail.com	
If a Student	Your Degree: e.g., MSc, PhD, etc.,
	MEng Nuclear Power
	Name of Supervisor (if supervised):
	Assoc Prof Paul Barendse
If this is a research contract, indicate the source of funding/sponsorship	
Click here to enter text.	
Project Title	
Condition Monitoring of Induction Machines in a Nuclear Power Station context	

I hereby undertake to carry out my research in such a way that:

- there is no apparent legal objection to the nature or the method of research; and
- the research will not compromise staff or students or the other responsibilities of the University;
- the stated objective will be achieved, and the findings will have a high degree of validity;
- limitations and alternative interpretations will be considered;
- the findings could be subject to peer review and publicly available; and
- I will comply with the conventions of copyright and avoid any practice that would constitute plagiarism.

SIGNED BY	Full name	Signature	Date
Principal Researcher/ Student/External applicant	Naasef Rylands		05 Mar 2017

APPLICATION APPROVED BY	Full name	Signature	Date
Supervisor (where applicable)	Assoc Prof Paul Barendse		25/4/17 Click here to enter a date.
HOD (or delegated nominee) Final authority for all applicants who have answered NO to all questions in Section 1; and for all Undergraduate research (Including Honours).	A/PROF SUNETRA CHOWDHURY Click here to enter text.		19/5/17 Click here to enter a date.
Chair : Faculty EIR Committee For applicants other than undergraduate students who have answered YES to any of the above questions.	Click here to enter text.		Click here to enter a date.